Volume 93, Number 5, September–October 1988
Journal of Research of the National Bureau of Standards

In This Issue:

Departments

News Briefs

Conferences/Events

Articles

Volume 93, Number 5, September–October 1988
Journal of Research of the National Bureau of Standards

News Briefs

Developments

LASER DOPPLER COOLING LIMIT FOR ATOMS BROKEN

Careful measurements of the temperature of "gases" of cooled atoms reveal that the *lowest temperatures achieved may be more than 10 times lower than the limit predicted* by the generally accepted model. These results were reported by a group of physicists from NBS, the University of Connecticut, and the State University of New York (SUNY) at Stony Brook in the July 11 issue of *Physical Review Letters*. Extremely low-temperature gases of free atoms or ions are produced in laboratories by "laser cooling." The generally accepted model of this process predicts a lower limit to the temperature that can be achieved by these techniques. The limit is different for each type of atom. Using four different methods, the NBS group measured the temperature of sodium atoms, laser-cooled in optical molasses, to be about 45 microkelvins, with an uncertainty of about 20 microkelvins—substantially below the presumed limit for sodium of about 240 microkelvins. Laser cooling experiments seek to create samples of free, isolated atoms or ions, moving very slowly in a confined region, where they can be probed by various techniques. Such experiments can make very accurate measurements of intrinsic properties of the atoms—measurements which in the past have led to important advances in the theories of quantum mechanics and relativity, among others.

PROGRAM SEEKS RESEARCHERS IN POLYMER COMPOSITES

A bureau research program to target the most critical barriers in high-performance polymer composite processing that producers must overcome to meet increasing international competition *invites participation from researchers in industry, universities, and government.*

The U.S. market for high-technology plastic products, valued at approximately $1.6 billion in 1987, is expected to grow to $10 billion before the year 2000. The U.S. now has the technological lead in the use of high-performance polymer composites in defense and aerospace applications. In high-volume mass markets, however, U.S. industries face intense competition. Polymer composites are reinforced plastics carefully engineered to meet specific performance requirements. By combining polymer resins with reinforcements such as graphite fibers, very versatile, lightweight, and high-strength materials can be made. Examples include jet aircraft parts and sporting goods like tennis rackets and fishing rods.

For information on the program, contact Donald L. Hunston, A209 Polymers Bldg., National Bureau of Standards, Gaithersburg, MD 20899, telephone: 301/975-6837.

ENERGY MANAGEMENT AND CONTROL SYSTEMS COMPARED

In a comparison of two energy management and control systems (EMCS), researchers in the NBS Center for Building Technology found the *microprocessor-based EMCS performed as well as, and in many cases better than and consumed less energy than, the pneumatic control system*. The microprocessor-based system was developed by NBS and constructed of "off-the-shelf" components. The communication and control software also was written in-house. The system was installed in the NBS 11-story administration building along with the in-place pneumatic system. Both were monitored for a year. One advantage of the microprocessor system is ease of resetting and maintaining operating schedules. A problem with the pneumatic system is that the tuning of the system "drifted" with time and was sensitive to changes made during routine maintenance. Another advantage of EMCS is more information about the performance of the system allowing problems to be discovered earlier and providing information for diagnosing a problem. *Comparison of Direct Digital Control and Pneumatic Control Systems in a Large Office Building* (NBSIR 88-3739) is available for $14.95 prepaid from National Technical Information Service, Springfield, VA 22161. Order by PB #88-215470/AS.

ADVANCED SHIPYARD MANUFACTURING SYSTEM DEDICATED

Officials of NBS and the U.S. Navy's Naval Sea Systems Command (NAVSEA) on July 19 dedicated a *state-of-the-art robotic manufacturing system designed and assembled by NBS for the Navy's Mare Island (Calif.) Naval Shipyard*. The Mare Island workstation, scheduled for delivery to the shipyard this fall, will be one of a handful of facilities in the United States capable of operating, largely untended, 24 hours a day, five days a week. Consisting of an automated lathe, industrial robot, automated storage and retrieval system, and various control computers, and incorporating several advanced automation techniques, the workstation is designed to produce any of 40 different pipe connector parts used to suppress noise in nuclear submarines. Such parts are not stockpiled and are produced on demand when the submarine is serviced. Current manual production methods require about 17 hours to make one of these parts. The Mare Island workstation can machine the same part in under 30 minutes and is already turning out parts for the Navy on a trial basis. The advanced manufacturing techniques used in the workstation are applicable to any manufacturing operation.

TRACING INDUSTRIAL EMISSIONS TO THEIR SOURCES

In an effort to track emissions from coal-fired industrial plants to their sources, researchers at NBS and the University of Maryland have developed a technique that shows promise as a *simple and definitive way of tracing smoke particles*. It may be the first method suitable for tracing fine particles over long distances. Other techniques that use tracer gases detect only gaseous components of stack emissions, not particles. The NBS/Maryland work, sponsored by the Electric Power Research Institute, uses artificially enriched stable isotopes of rare earth elements as "tags" to permit positive identification by mass spectrometry of emission particles near the source or miles away. These isotopes are nontoxic and inexpensive. Besides allowing samples to be traced to their sources, an analysis also can measure *how much of the tagged material is present*, in essence gauging the source's environmental impact. The NBS/Maryland scientists also hope to combine their study results with those of researchers examining gaseous emissions from coal-fired plants to produce a more complete picture of total emissions.

SQL TEST PACKAGE AVAILABLE FROM NBS

A package of tests to help users and vendors *determine compliance with a new Federal Information Processing Standard Publication (FIPS PUB) 127 for the Database Language SQL* is available for purchase from NBS. SQL is a voluntary industry standard language used to develop database management system applications. FIPS PUB 127 requires federal agencies to implement SQL in relational database management system applications acquired or developed after Aug. 3, 1988. The test suite will help both users and vendors meet the standard. Database management systems can save time and money by making data, application programs, and trained users "portable" from one system to another. The NBS test package includes six types of tests in three programming languages—C, FORTRAN, and COBOL. For further information, call Joan Sullivan (301/975-3258) or Joseph Collica (301/975-3267) or write to A266 Technology Bldg., National Bureau of Standards, Gaithersburg, MD 20899. FIPS PUB 127 is available from the National Technical Information Service, Springfield, VA 22161, 703/487-4650.

U.S., ITALY AGREE ON LUMINOUS INTENSITY STANDARD

NBS and the Istituto Elettrotecnico Nazionale "Galileo Ferraris" (IEN), Italy, signed an agreement on Apr. 15, 1988 recognizing the equivalency of their national standards for luminous intensity measurements as defined by the International System of Units (SI). The agreement, based on extensive interlaboratory comparisons, marks the seventh equivalency recognition between NBS and Italian national standards laboratories. The bureau and IEN recognize the equivalency of their national standards for voltage, electrical resistance and capacitance, and time. NBS also has an agreement with the Istituto di Metrologia "G. Colonnetti" of the Consiglio Nazionale delle Ricerche for length and temperature. Both the U.S. and Italy are signatories of the Convention of the Meter and determine their basic units of measurements in accordance with the definitions for SI units adopted by the General Conference of Weights and Measures, an intergovernmental body that is the world authority on physical quantities and the ways they are measured. *These agreements facilitate the sale of products between the two countries* when traceability to national standards is required by contract or law.

U.S., ISRAEL RECOGNIZE EQUIVALENCE OF TIME STANDARDS

NBS and its Israeli equivalent, the National Physical Laboratory (INPL) in Jerusalem, signed an agreement on June 7 recognizing the equivalence of the unit of time measurement, the second, as kept by each country to at least one part in 10,000,000,000,000.

Both the U.S. and Israel measure seconds in accord with the definitions of the International System of Units (SI), which is maintained by the General Conference of Weights and Measures (CGPM).

The agreement between NBS and INPL essentially *means that precision timing instruments calibrated against the standards of either country may be considered equally*, as for example in meeting procurement specifications that require a calibration "traceable" to NBS or INPL. Such agreements require careful intercomparison of national standards to determine the level of accuracy at which "equivalence" can be said to exist. NBS has entered into several such agreements with foreign standards organizations to facilitate international trade.

Standard Reference Materials

STANDARD TO MEASURE CARBON IN NATURAL MATERIALS

To meet the needs of environmentalists and other researchers in science and industry, NBS has developed a new set of materials for *calibrating automated instruments to measure the carbon content* in biological tissues and botanical specimens. These devices, widely used in the metals industry for the rapid analysis of carbon in steel, produce highly sensitive and precise data when they are calibrated with accurate standards. Standard Reference Material (SRM) 1216, Carbon Modified Silica, is a set of three silica matrices certified for concentration levels of carbon at 0.70, 9.06, and 17.04 percent. Each of the three materials has been measured both by prompt gamma neutron activation and combustion techniques using known, highly characterized material as controls for their certification.

SRM 1216 is available for $192 for the set of three materials from the Office of Standard Reference Materials, B311 Chemistry Bldg., National Bureau of Standards, Gaithersburg, MD 20899, telephone: 301/975-6776.

LOW ALLOY STEEL CALIBRATION STANDARDS ANNOUNCED

NBS has developed a new graded series of seven low alloy steel standards for calibrating optical emission and X-ray fluorescence spectrometers. Great care has been used in preparing these materials to obtain a high level of homogeneity to meet the demands of new, highly precise instruments *used in the quality control of alloy materials*. Standard Reference Materials (SRMs) 1761-1767, prepared in consultation with ASTM and industry, are intended as a replacement for the currently available 1260 series of low alloy steels. SRMs 1761-64 contain major and minor elements at normal concentration levels and SRMs 1765-1767 contain a graded series of elements at the trace levels. The new standards are available for $135 each in the form of disks approximately 34 mm (1 3/8 in) in diameter and 19 mm (3/4 in) thick. To obtain information on the certified values of each disk, or to order the new graded series of calibration standards, contact the Office of Standard Reference Materials, B311 Chemistry Bldg., National Bureau of Standards, Gaithersburg, MD 20899, telephone: 301/975-6776.

Standard Reference Data

PUBLICATION OF SUPPLEMENT TO THE JOURNAL OF PHYSICAL AND CHEMICAL REFERENCE DATA ANNOUNCED

The Office of Standard Reference Data announced the publication of "Gas-Phase Ion and Neutral Thermochemistry" by S. G. Lias, J. E. Bartmess, J. F. Liebman, J. L. Holmes, R. D. Levin, and W. G. Mallard. This volume, the update of the 1977 publication "Energetics of Gaseous Ions," provides evaluated ionization energies for 5,000 molecules, atoms, and radicals, and proton affinities of 1,000 compounds, as well as electron affinities and gas phase acidities of approximately 3,000 species. The heats of formation of all relevant ions and the related neutral species are also included.

For information on the publication "Gas-Phase Ion and Neutral Thermochemistry," contact S. G. Lias, A317 Physics Bldg., National Bureau of Standards, Gaithersburg, MD 20899, telephone: 301/975-2506.

OFFICE OF STANDARD REFERENCE DATA SUPPORT FOR DATA COMPILATION PROJECTS ANNOUNCED

The Office of Standard Reference Data announced the awarding of new grants under its 1988 Program for Critical Compilations of Physical, Chemical, and Materials Data in July. The program, which is supported by funds from the National Science Foundation, offers support for projects involving the compilation and critical evaluation of data on well-defined chemical, physical, or materials properties. Each project must lead to a publishable compilation, critical review, or computer database containing recommended values for the properties in question along with an assessment of the reliability of these recommended values. The program is in its eighth year.

The new critical data evaluation projects which were approved for the coming year were:

- High temperature kinetic data for combustion- and propulsion-related chemistry (Dr. Norman Cohen, The Aerospace Corporation)
- Thermodynamic and phase diagram data for the binary systems of iron (Dr. H. Okamoto, ASM International)
- High temperature aqueous electrolyte data (Prof. Robert H. Wood, University of Delaware)
- Vaporization equilibria in one component systems (Dr. Vladimir Majer, University of Delaware)
- Thermodynamic data on lipid mesomorphic phase transitions and miscibility (Prof. Martin Caffrey, The Ohio State University)
- Absolute coverage of adsorbed molecules on transition metal surfaces (Prof. Torgny Gustafsson, The State University of Rutgers)
- Application of expert systems to critical evaluation of thermophysical property data (Drs. J. C. Holste and K. R. Hall, Texas A&M)
- Thermodynamic and Vaporization Data for Metal Sulfides (Prof. Paul W. Gilles, University of Kansas)

The program has been highly successful in drawing upon the expertise of scientists in universities and industry to add to the body of standard reference data available to the U. S. technical community.

NBS FILE OF JANAF THERMOCHEMICAL TABLES NOW AVAILABLE ONLINE WORLDWIDE

The third edition of the (Joint-Army-Navy-Air Force) *JANAF Thermochemical Tables*, published by the National Bureau of Standards (NBS), has been computerized to provide scientists and engineers with rapid access to important information on the performance of materials at high temperatures.

The new JANAF file is available to subscribers of STN International (Scientific and Technical Network), an online private sector retrieval service offered worldwide. The computerized database eliminates the need to manually search through approximately 1,800 pages of thermochemical tables in two volumes.

The numerical data in the new JANAF file can be used by researchers and designers to make quick performance calculations for chemical reactors such as rocket engines, air pollution control equipment, automotive internal combustion engines, coal gasifiers and furnaces, fuel cells, liquefaction reactors and their catalyst structures, and magnetohydrodynamic generators. The information also can be used by engineers in the design of chemical plants.

The JANAF tables project was established in late 1959 at the Thermal Research Laboratory of the Dow Chemical Company, Midland, MI, as a way to compile and publish consistent tables of thermodynamic data required for rocket propellent performance calculations by industry and the Department of Defense agencies. Today the database is located in the NBS Chemical Thermodynamics Data Center, one of 23 data centers that make up the National Standard Reference Data System (NSRDS).

For information on the availability of the new JANAF file through STN, or the third edition of the *JANAF Thermochemical Tables* (1985), and the computer-readable database for lease on magnetic tape, contact the Office of Standard Reference Data, A323 Physics Bldg., National Bureau of Standards, Gaithersburg, MD 20899, telephone: 301/975-2208.

Volume 93, Number 5, September-October 1988
Journal of Research of the National Bureau of Standards

Diffraction Imaging (Topography) with Monochromatic Synchrotron Radiation

Volume 93 Number 5 September-October 1988

Bruce Steiner, Masao Kuriyama, Ronald C. Dobbyn, and Uri Laor

National Bureau of Standards
Gaithersburg, MD 20899

Structural information of special interest to crystal growers and device physicists is now available from high resolution monochromatic synchrotron diffraction imaging (topography). In this review, the importance of superior resolution in momentum transfer and in space is described, and illustrations are taken from a variety of crystals: gallium arsenide, cadmium telluride, mercuric iodide, bismuth silicon oxide, and lithium niobate. The identification and detailed understanding of local variations in crystal growth processes are shown. Finally, new experimental opportunities now available for exploitation are indicated.

Key words: crystal growth; electrooptic materials; monochromatic diffraction imaging; synchrotron topography.

Accepted: May 19, 1988

1. Sources of Current Interest

New types of materials with enormous scientific and practical interest are now being created by atomic or "ultramolecular engineering" [1] of structures not found in nature. Successful fabrication of such materials, whether novel in structure or simply far freer of imperfections than found in nature, depends on detailed structural information. The degree of perfection that has been achieved, the effects of remaining defects, and sources of deviation from the intended structure all constitute the type of information required. More fundamental guidance that will underlie future advances in materials design concepts will come from knowledge and understanding of modification in properties engendered by specific variations in structure.

2. Types of Information Now Available through Diffraction Imaging

In contrast to electron microscopy, which provides information on the *location* of features in *small* regions of materials, diffraction imaging can portray minute *deviations* from crystal perfection over *larger* areas. Diffraction imaging by monochromatic synchrotron x-radiation [2] pinpoints and permits analysis of irregularities that can affect physical properties of materials. For example, lattice strains lead to strong contrast in such images, as in figure 1; and analysis of the patterns in these strains can lead to a detailed understanding of how they arise [3]. Similarly, crystallographic dislocations stand out in the images of high quality crystals, as seen in figure 2.

Analysis of such images can provide not only evidence of the presence and distribution of structural inhomogeneities but also an understanding of their structure and origins. As a result, steps can be taken to enhance or reduce their presence, as desired. Diffraction imaging thus provides useful information on variation in high quality crystals that can be correlated with specific aspects of their performance. Such a correlation can lead to improvement in device performance through guidance on

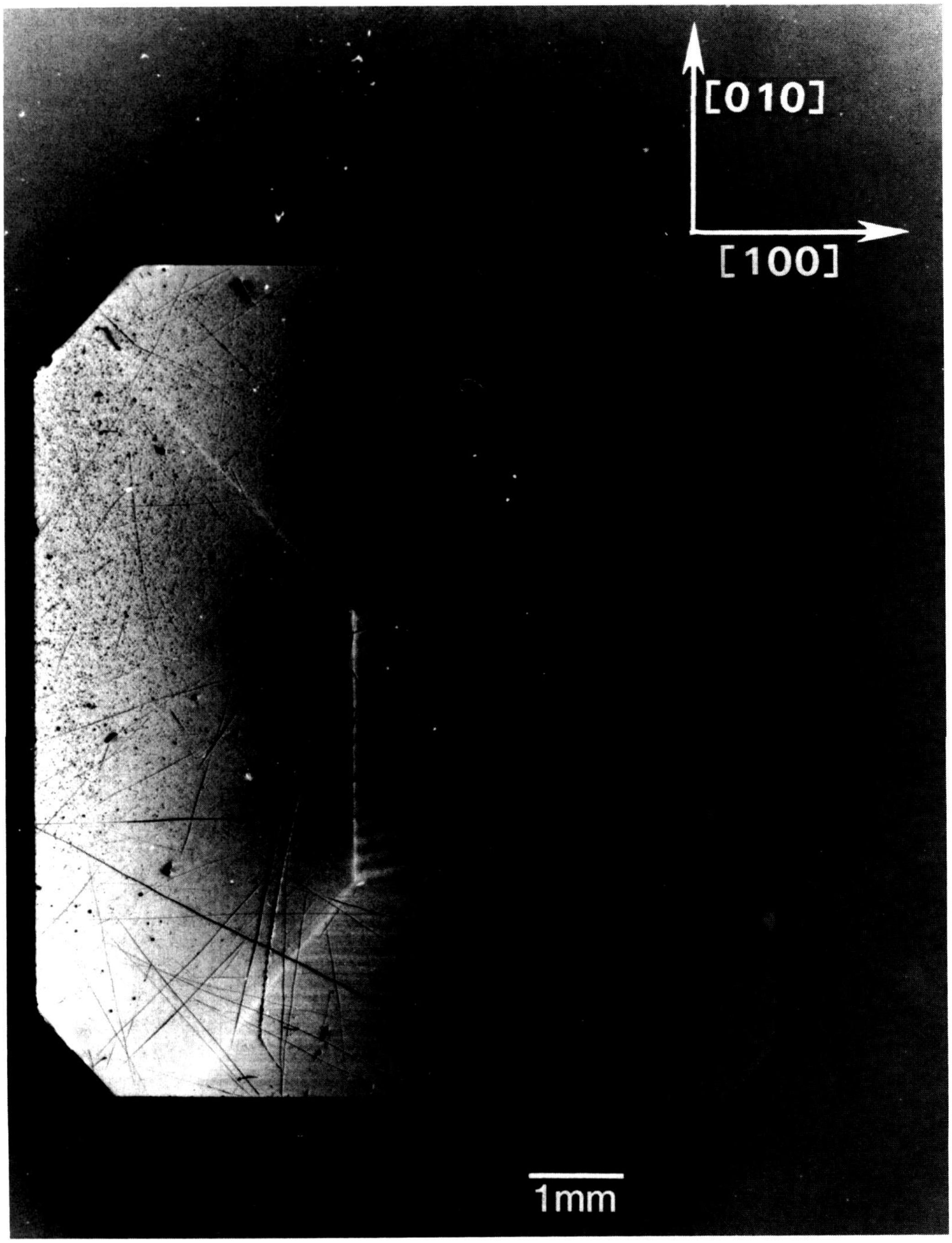

Figure 1. Strain patterns in the 8 keV (309) diffraction from a (001)-cut crystal (slice K) of bismuth silicon oxide.

desirable modification in crystal growth and subsequent processing parameters.

3. Current Experimental Opportunities

Synchrotron storage rings now permit far more comprehensive and useful realization of these opportunities than can be achieved with laboratory sources because of three optical characteristics of such rings: their effective small source size, their high brightness, and the presence of a continuous energy spectrum. The small optical source size permits formation of highly parallel x-ray beams, which are required for maximum resolution. The smallest source size achieved to date, 140 micro-

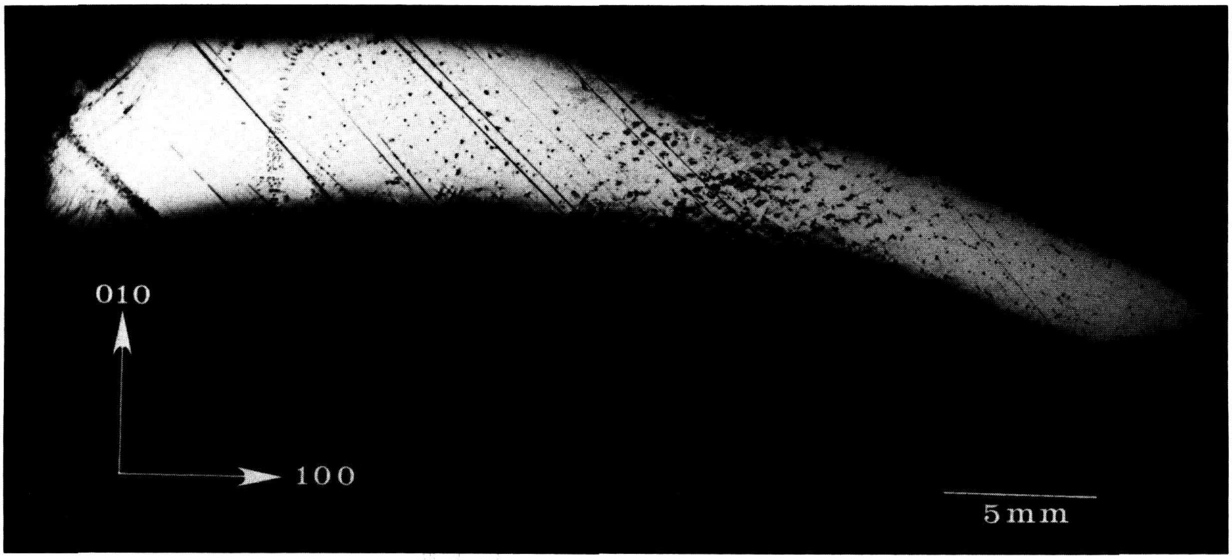

Figure 2. Dislocation patterns in the 10 keV (040) diffraction from an indium doped (001)-cut wafer of gallium arsenide.

meters, has been realized in the large storage ring at the National Synchrotron Light Source at Brookhaven National Laboratory. Optics at the end of one of its 20 meter beamlines can achieve at least 1.5 arc-second angular resolution, or less than a micrometer on the surface of a detector in a typical configuration. This resolution can be further increased through suitable optics. With the optics described here [4–6], individual dislocations are clearly seen as in figure 3.

The high brightness achieved in storage rings is central to several aspects of crystal characterization. First, high brightness enables one to insert additional optics for the improvement of angular and spatial resolution while maintaining a useful flux of photons, as described later. Second, high brightness permits observation of diffraction features in transmission. The distinctive signatures of the dislocations observed in figure 3 are visible only in diffraction in Laue geometry (transmission), with its integration of information from the interior of a crystal. Moreover, when strains are observed in transmission, as in figure 4, differences in their orientation in various parts of the image can be emphasized. In figure 4, for example, strains in the <100> direction are clearly visible in some parts of the crystal while absent in others that appear equivalent in diffraction in Bragg geometry. Analysis of such differences provides information on the processes leading to their formation [3]. Third, the high brightness of a storage ring permits video camera observation of diffraction images in real time. This in turn facilitates surveys of subgrain boundary structure and of large scale crystal strain that are difficult to observe and prohibitive in time by any other means. Also important is the capability for *in situ* experiments under environmental variation of conditions such as temperature, pressure, or electric and magnetic fields.

The availability of a choice in wavelength permits work in transmission that would otherwise not be possible because of absorption. The utilization of a monochromator with the continuum from a synchrotron storage ring can provide important further advantages. The restriction of diffracting radiation to a narrow spectral band substantially increases the contrast in an image over that obtainable with a white beam as in figure 5. The interpretation of such monochromatic images is far simpler and more certain than the interpretation of images formed with white radiation.

When asymmetric diffraction is employed in the monochromator, two additional benefits can be obtained [8]. First, the beam can be expanded several fold to a height of several centimeters. With such a beam, large crystals can be examined without serious interferences from spurious contrast generated by scanning. Second, the parallelism of the analyzed beam is increased by the same factor, bringing the resolution well under one arc-second. This can be reduced to much less than a tenth of an arc-second with appropriate monochromator optics where necessary.

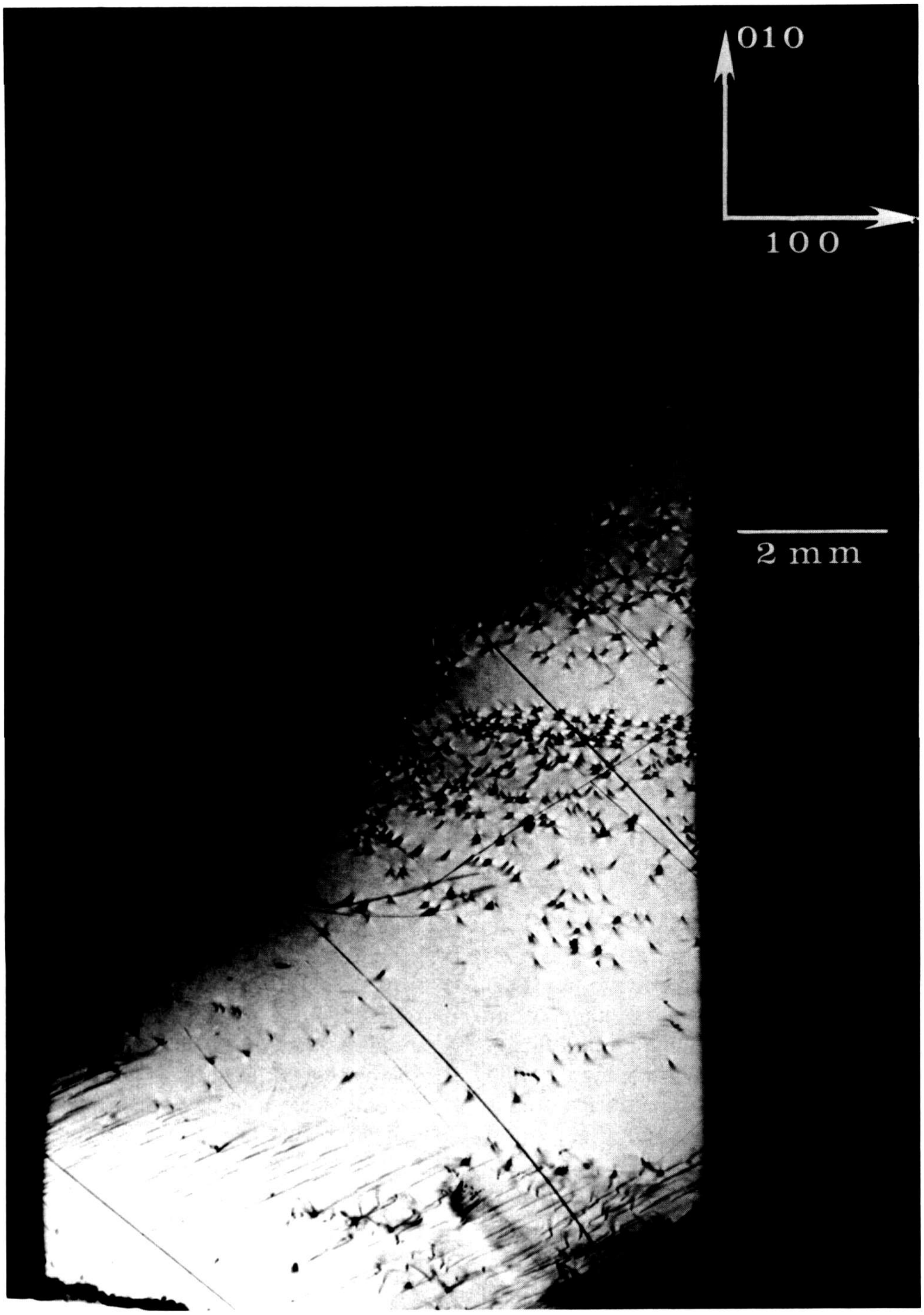

Figure 3. Individual dislocations resolved in 8 keV (400) diffraction from the indium doped (001)-cut wafer of gallium arsenide shown in the previous figure, after fracture.

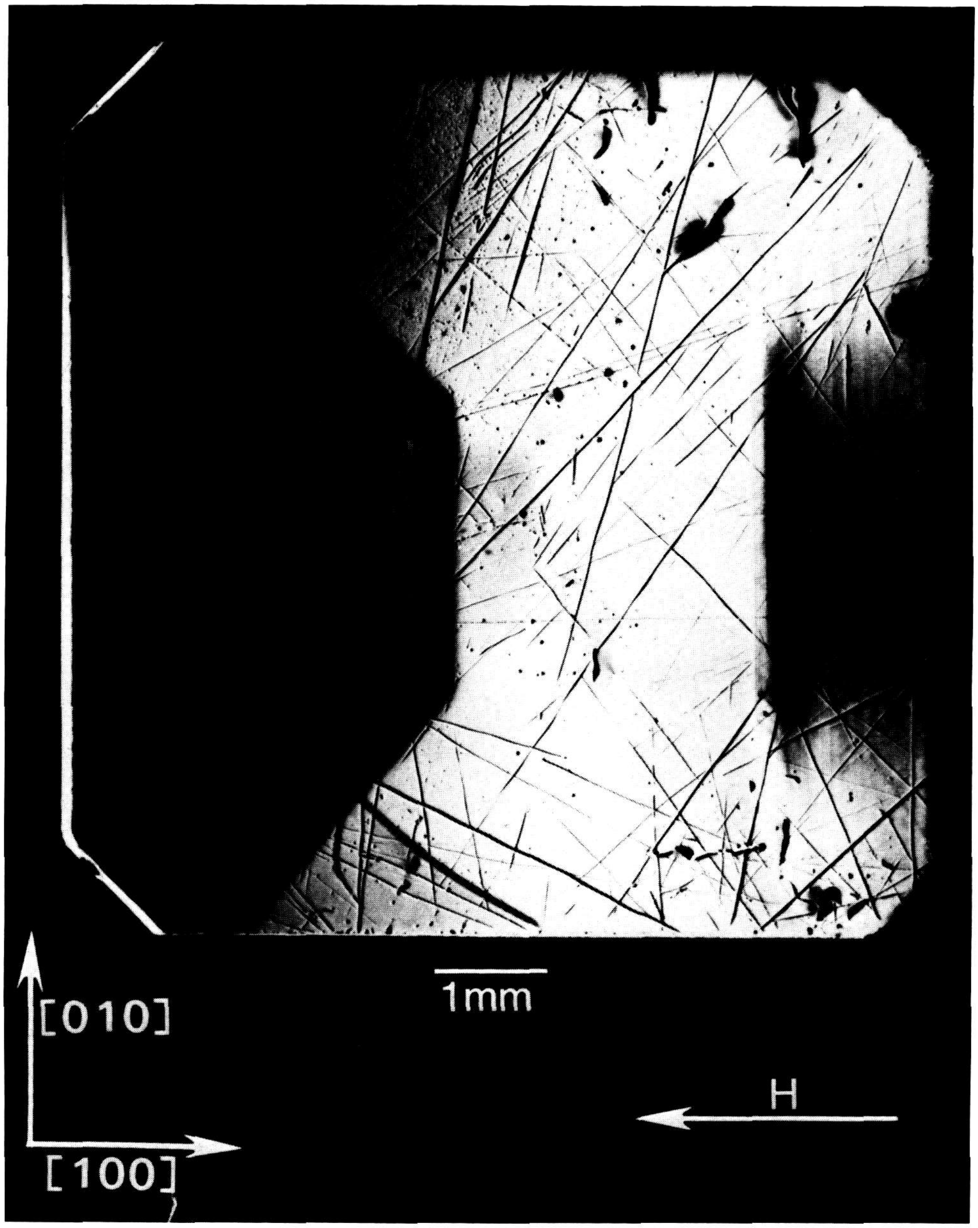

Figure 4. Image of 13.4 keV diffraction in Laue geometry (transmission) from ($\bar{6}$00) planes of the (001)-cut bismuth silicon oxide crystal shown in figure 1 in diffraction in Bragg geometry.

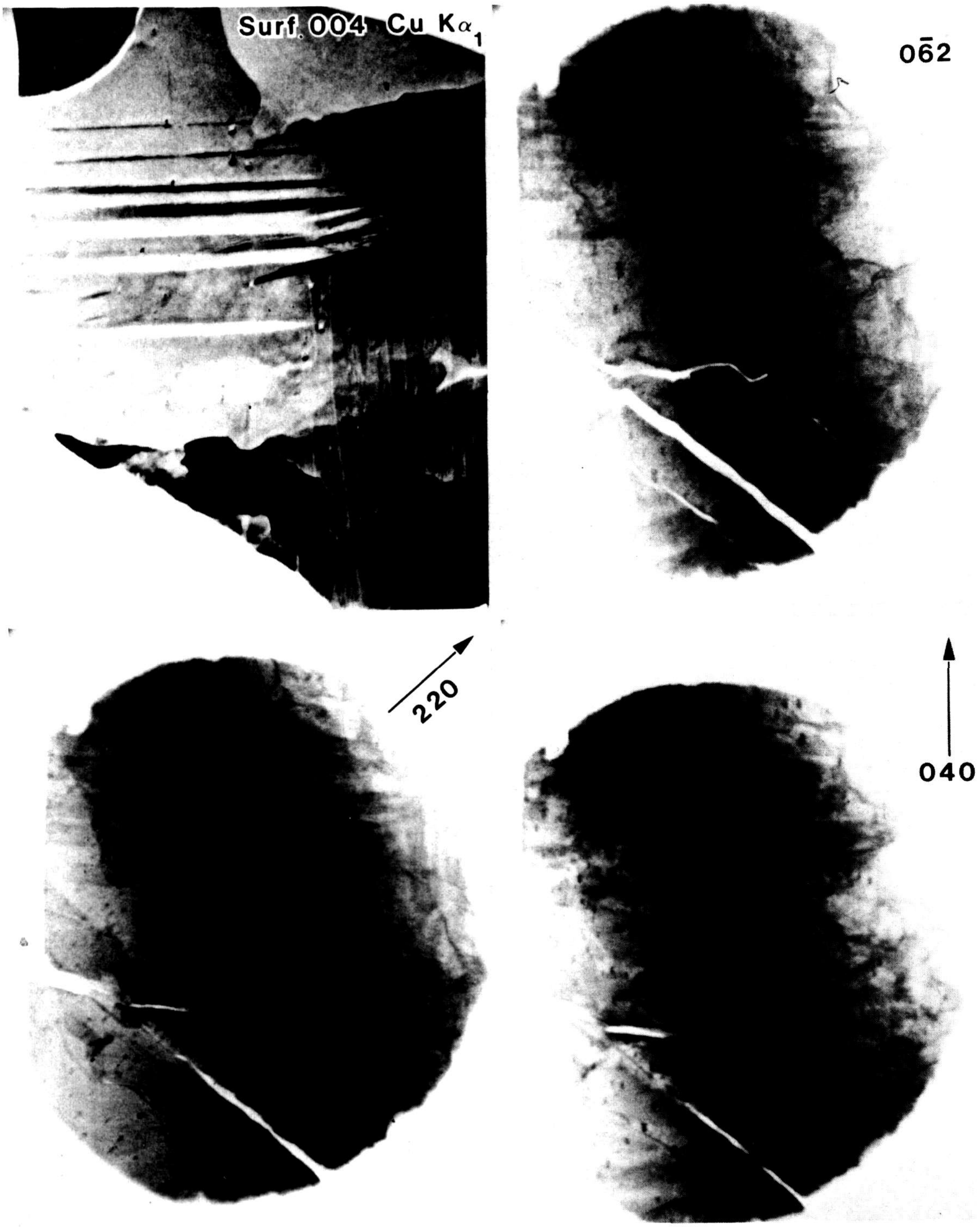

Figure 5. Comparison of a monochromatic laboratory (004) diffraction image of iron-aluminum crystal with three white beam synchrotron topographs: (06̄2), (220), and (040) of the same crystal.

These advantages are being realized on the National Bureau of Standards (NBS) Materials Beamline X23A-3 at the National Synchrotron Light Source (NSLS) at the Brookhaven National Laboratory [5]. Figure 6 shows the x-ray optical configuration for diffraction imaging at this beamline [6,7]. Two flat crystals (L1 and L2) in sequence control beam divergence and beam size and are arranged to keep the beam position with respect to the sample location fixed in space, independent of the energy selected for study. The first monochromator crystal (L1) intercepts the white radiation beam from the storage ring. This crystal and the second (L2) move and rotate in tandem to the appropriate positions to give a highly parallel, monochromatic beam of specified energy with a desired dimension.

It is important to have available monochromatic beams with variable dimensions and flux density. The monochromator crystals, L1 and L2, can be configured in three different ways: (a) symmetrical diffraction, resulting in magnification of one; (b) asymmetric diffraction in the magnification mode, (providing a large size, more highly parallel beam); and (c) asymmetric diffraction in the demagnification mode, [providing a concentrated, less parallel beam, useful for work with an x-ray magnifier [9] (fig. 7), as described later, and for "out state" analysis (fig. 8)].

Diffracted image magnifier crystals L3 and L4 in figure 6 can be placed orthogonally in the beam to produce two dimensional magnification by successive stages of asymmetric Bragg diffraction. Such an x-ray image magnifier produces an undistorted image, magnified up to 150-fold before detection either with film or with an image detector [9,10]. The submicron range of resolution in real time for crystals can thus be reached by commercially available two dimensional image detectors with a practical resolution of about 30 micrometers. Figure 7 illustrates the formation of a two dimensionally magnified image of a 0-diffracted (forward diffraction) beam in transmission. Such an x-ray magnifier can be used also as a zoom lens [6], since a given pair of two asymmetrically cut crystals provides continuously changing magnification as different energies of the incident beam are selected by the control system.

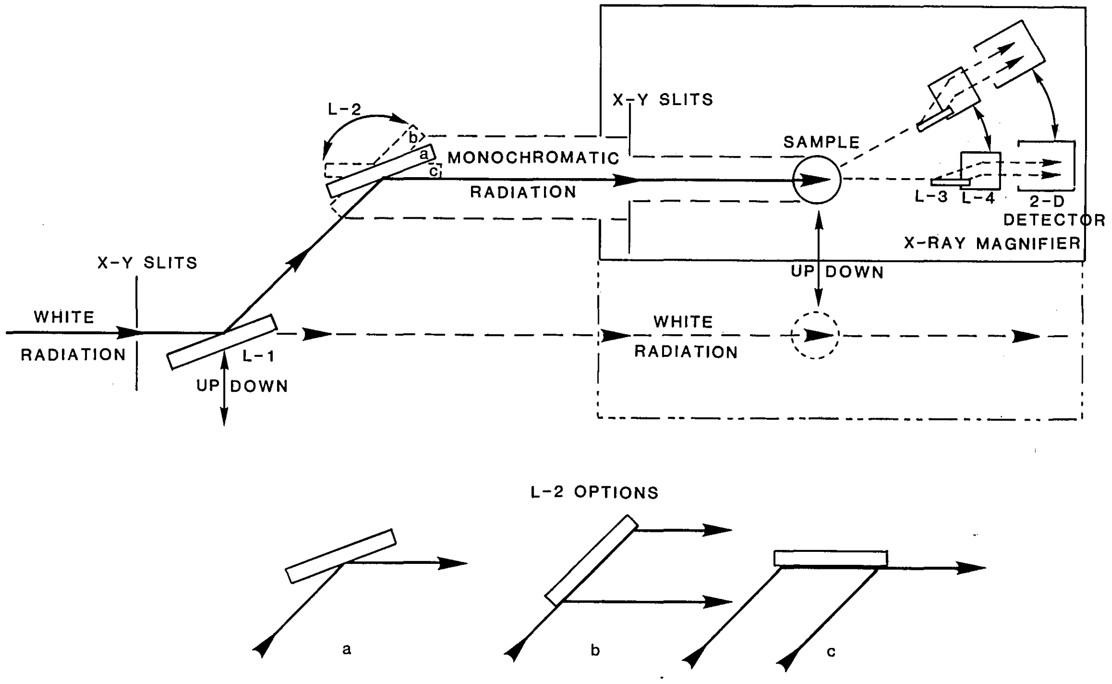

Figure 6. NBS materials science beamline optics: arrangement of flat crystal diffraction elements used for imaging. L1: first monochromator crystal, L2: second monochromator crystal, L3: first crystal of x-ray magnifier, and L4: second crystal of x-ray magnifier.

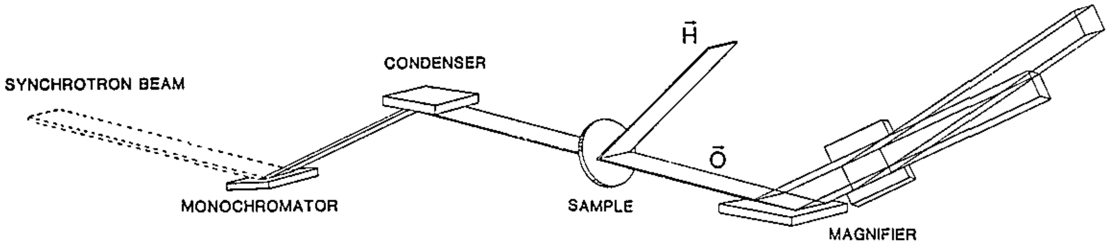

Figure 7. Image magnification: schematic beam path for two dimensional magnification. This example shows the image formation for the 0 (forward)-diffracted beam in transmission under the Bragg condition.

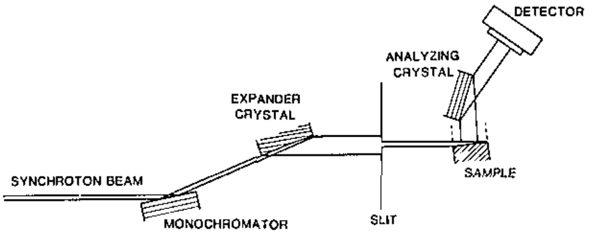

Figure 8. Schematic of experimental arrangement for "out state analysis." A fourth crystal, in addition to two monochromator crystals and the sample being studied, passes the diffracted beam only over a narrow angular range, permitting observation either of defect images or of perfect (matrix) crystal images without interference from the other type of image.

The use of flat crystal diffraction in an analyzer stage provides additional important opportunities for further analysis. Crystal L3 alone when set for asymmetric diffraction can act as an ideal angular analyser with an aperture less than one arc-second. This defines precisely the momentum transfer of x-ray photons detected after diffraction and scattering. In conjunction with an incident beam prepared to be extremely parallel by the monochromator system described above, such an analyzer crystal is capable of providing for equi-d mapping (lattice parameter), angle-resolved imperfection imaging, and small angle x-ray scattering (SAXS) imaging [11–15]. These analytic features strengthen diffraction imaging with a new quantitative capability in which the spatial imperfection information in diffraction images is preserved or enhanced. With these optical systems, microstructural effects that have been observed and measured *in situ* on a real time basis under simulated environmental conditions in white beam imaging now come within reach for monochromatic imaging.

4. Illustrative Examples

A crystal containing distinct grains (which by definition differ in crystallographic orientation) yields broad or structured rocking curves in conventional x-ray diffraction. Diffraction images of such crystals typically display sharp contrast among the various grains. However, even where the difference in orientation is in excess of several arc-minutes, simultaneous diffraction from more than one grain can be observed and analyzed quantitatively if the crystal is suitably oriented with respect to the beam, as has been done in figure 9, where five grains can be distinguished. In such instances, the tilt of the individual grains and their orientation with respect to one another can be accurately determined from the clear displacement of the images of the various grains with respect to each other [16].

Broad rocking curves can arise also from a different source of imperfection, which, in the absence of images, is sometimes confused with the assumed presence of multiple grains or subgrains. One such case is shown in figure 10. The rocking curve for this crystal of cadmium telluride would approach in breadth the curve for the mercuric iodide crystal shown in figure 9. However, in contrast to the diffraction image of mercuric iodide, the image of cadmium telluride shows no major sharp boundaries separating crystal grains or subgrains. The breadth of the rocking curve in this instance is traceable to relatively gradual, irregular variation either in the lattice constant or in the lattice orientation. Improvement of such crystals will clearly depend on the particular types of crystal imperfection that are dominant. Steps taken to reduce the nucleation or propagation of additional grains will be ineffective in improving the quality of crystals whose perfection is limited principally by more subtle inhomogeneity within individual grains, perhaps due to impurities or deviation from stoichiometry.

Clearly delineated sharp subgrain boundaries are observed also in high quality crystals. Such boundaries can separate regions of high contrast even when the orientation of the subgrains differs only by a few arc-seconds in the direction of the

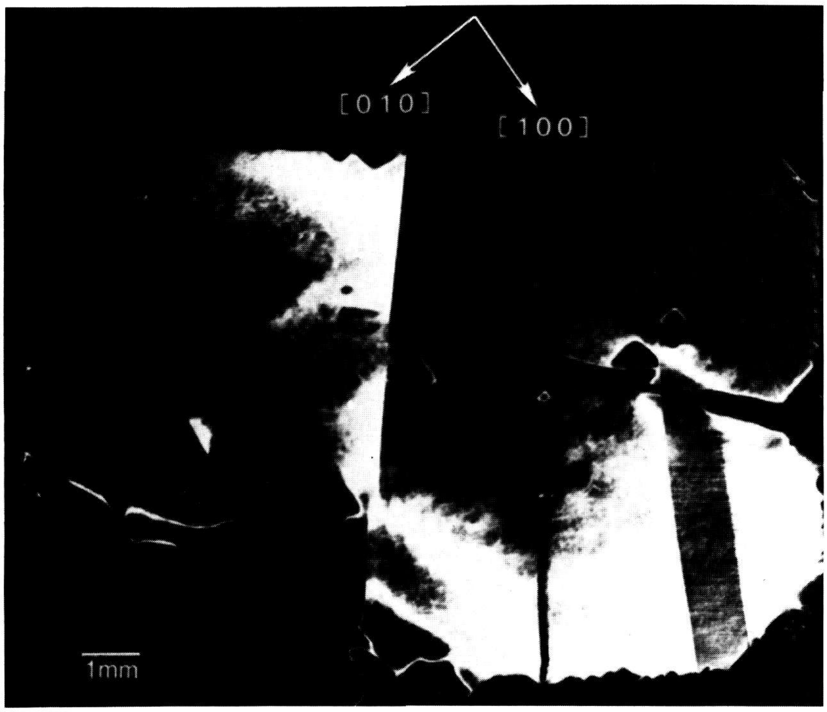

Figure 9. Image of 8 keV diffraction from (1 1 10) planes of a mosaic (001) cut mercuric iodide crystal.

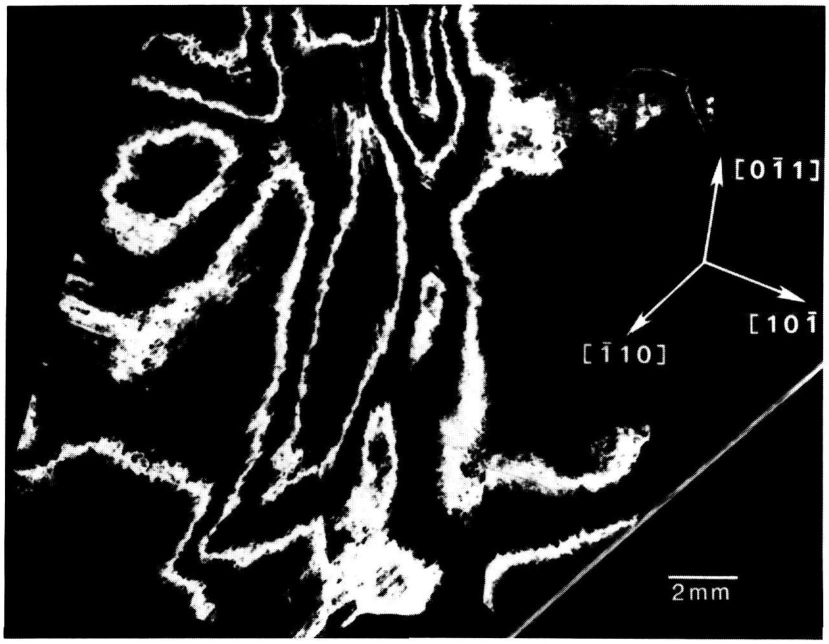

Figure 10. "Contour map" of strains in (111)-cut slice of cadmium telluride, recorded by superimposing diffraction from (333) planes of cadmium telluride recorded at three diffraction angles differing by 144 arc-seconds.

beam, as in the case in figure 11. More complex boundaries can be resolved even under unfavorable conditions in which imperfections are more complex, as is characteristic of undoped gallium arsenide, shown in figure 12. The orientation of each feature is indicated by changes in the visibility with change in diffraction. Highly oriented features in some parts of this image result from boundary scattering in the interior of the crystal, while other features display sharp contrast characteristic of features located close to the surface.

Other types of structure, clearly related to specific aspects of the growth of a crystal, are visible in indium doped gallium arsenide, as in figure 13. Geometrical features in a circular region of the center of a boule appear to imply faceted growth in this region. This is surrounded by striations associated with periodic fluctuation in one or more growth parameters. An image of the central region of this boule is shown magnified in figure 14. The rectangular features characteristic of this region are oriented along <110> directions. These different features in local regions indicate that the interface between the melt and solid is curved and changes in time during crystal growth [17].

5. Comprehensive Understanding

A variety of strains and other crystallographic irregularities can thus be portrayed by diffraction imaging. Through such observations, the role that these defects play can be correlated with specific aspects of materials properties [18]. However, also inherent in this analysis is the insight that it can provide into the origin of complex anomalies and the corresponding potential for their control where suitable samples are available for study.

An example of this aspect of monochromatic synchrotron diffraction imaging is a recent study carried out on three slices taken from a single high quality boule of bismuth silicon oxide grown in the [001] direction as shown in figure 15 [3]. The three slices were cut and polished perpendicular to the growth direction, the perimeter retaining the shape that it acquired during growth. Slice K is shown in Bragg (reflection) geometry in figure 1 and in Laue (transmission) geometry in one orientation in figure 4. Slices E and I are shown in Bragg geometry in figures 16 and 17, respectively. Slice I is shown in Laue geometry in figure 18. Slice K is shown in a second orientation in Laue geometry in figure 19.

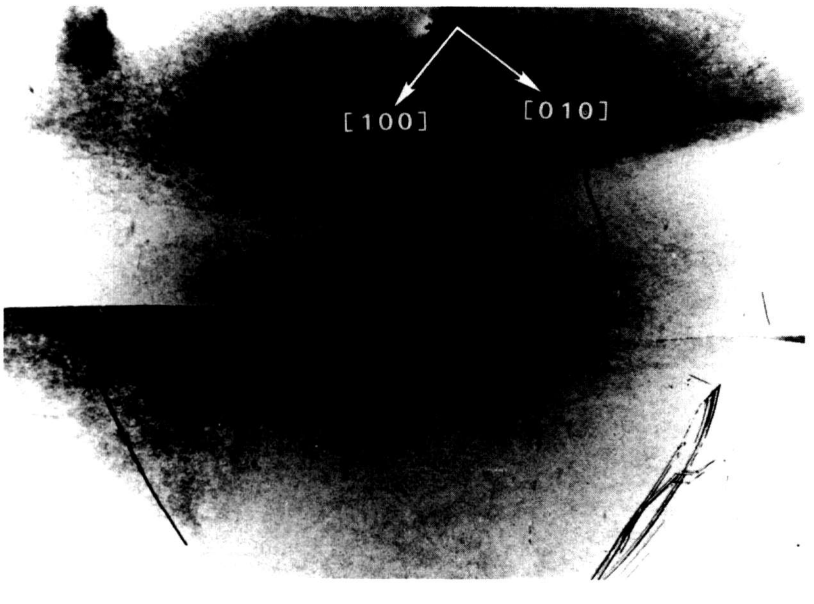

Figure 11. Sharp boundaries separating subgrains differing in orientation by about 2 arcseconds, shown in 8 keV diffraction from $(\hat{2}\hat{2}4)$ planes of a (001)-cut undoped gallium arsenide wafer. Also visible are curved regions of strain that produces curved, continuously varying contrast.

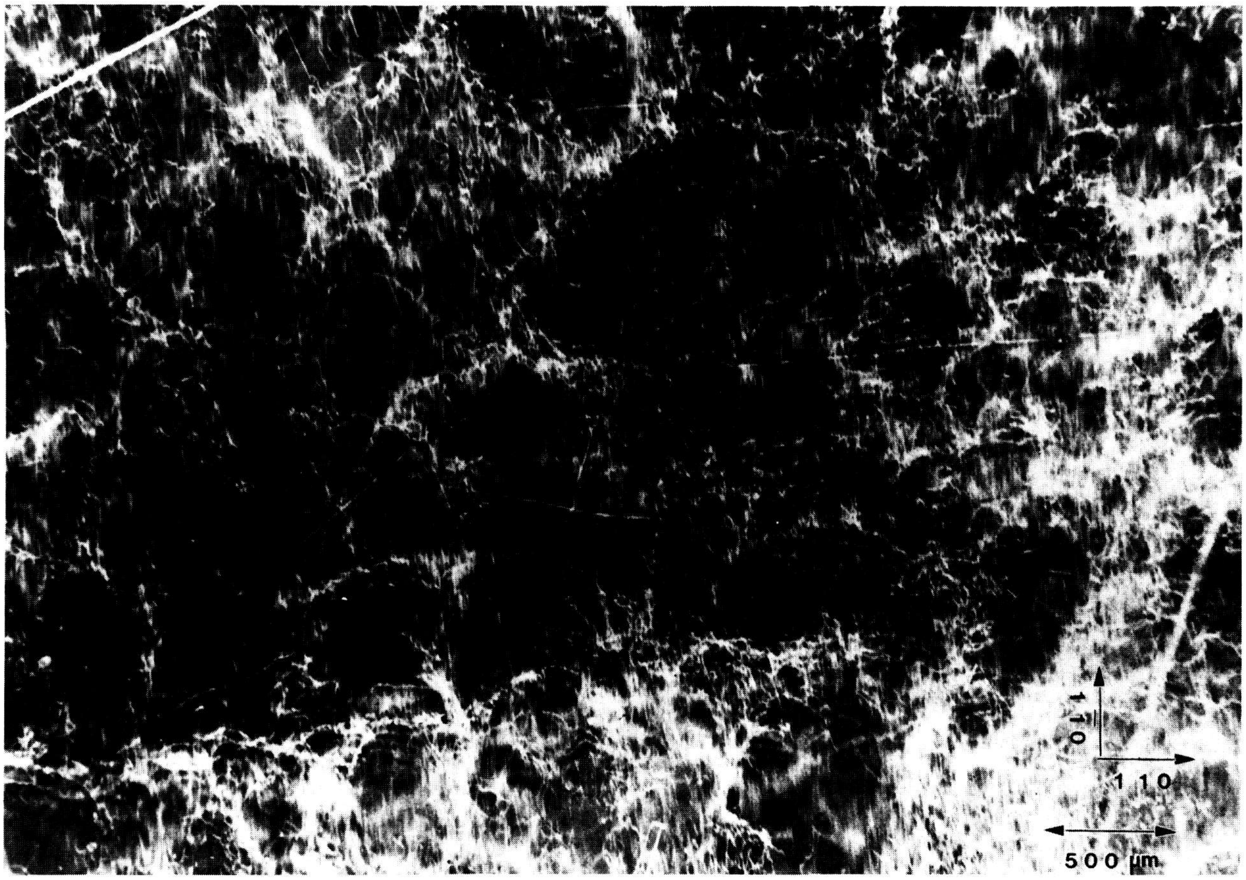

Figure 12. Boundary defects (possibly antiphase interfaces) observed in 10 keV diffraction in Laue geometry (transmission) from (220) planes of (001)-cut undoped gallium arsenide crystal.

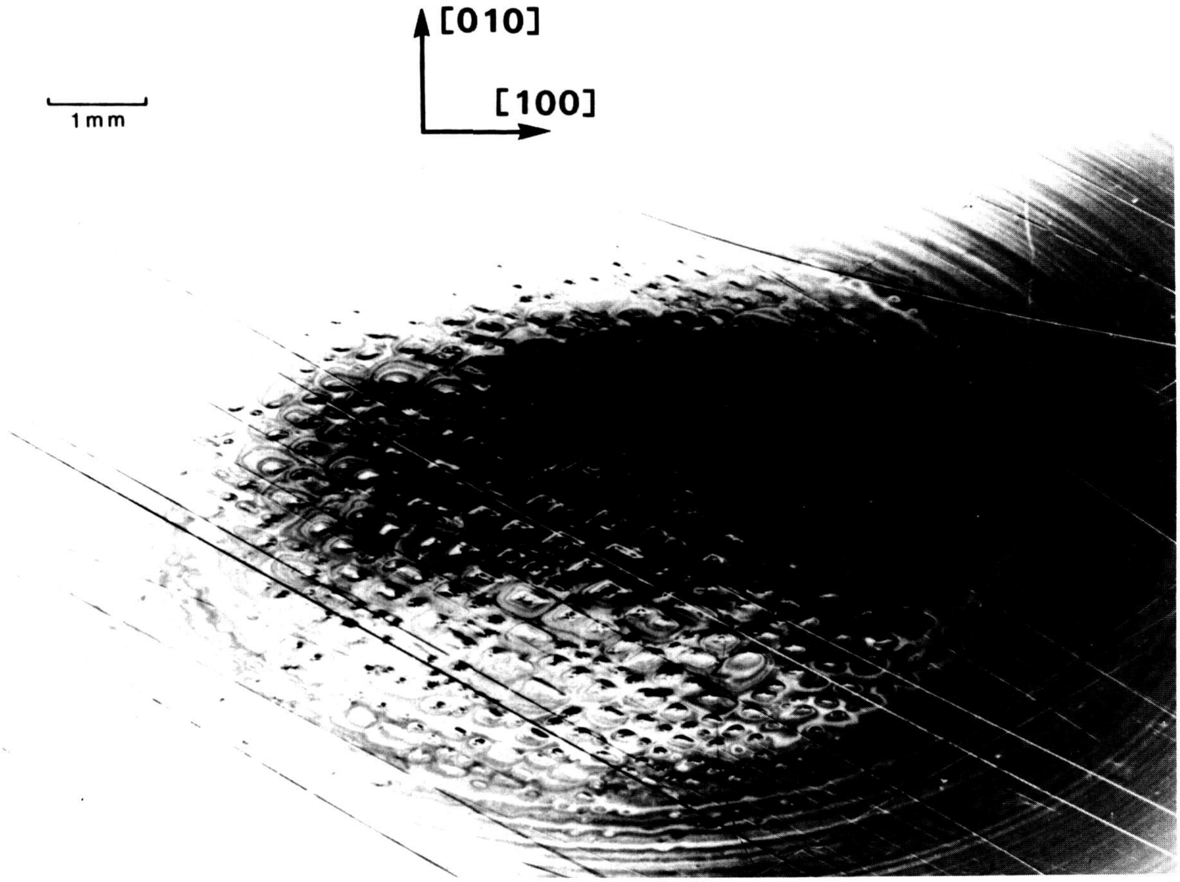

Figure 13. Image obtained in Bragg geometry diffraction at 8 keV from (004) crystal planes of the (001)-cut indium doped gallium arsenide wafer shown in figure 2 and 3 in Laue geometry.

Figure 14. Magnified portion of image of diffraction in Laue geometry at 10 keV from (400) planes of the (001)-cut indium doped gallium arsenide crystal shown in figures 2, 3, and 13.

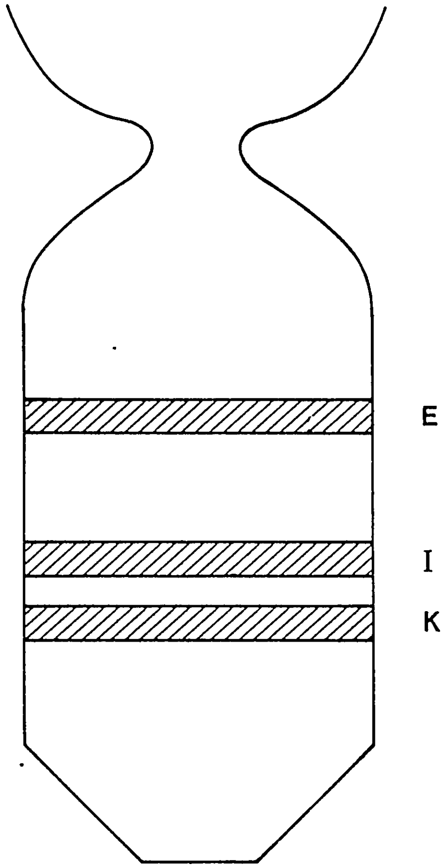

Figure 15. Relative positions of slices taken from a single high quality 8 mm boule of bismuth silicon oxide.

Analysis of these diffraction images permits us to unfold the following sequence of steps in the faceted growth of the boule. Shortly after necking, a small near-(001) growth plane had been established in the center of the growing face. Four peripheral {101} facets had also been formed. These are depicted in figure 20. By the time that the boule had grown to the location of slice E, the $(0\bar{1}1)$ facet was growing more rapidly than the others, causing it to decrease in area as illustrated in figure 21. Meanwhile, the central, near-(001) facet was growing nonuniformly. Its growth rate was greater in proximity to the rapidly growing $(0\bar{1}1)$ facet, causing the central near-(001) facet to deviate from a precise (001) orientation and resulting in strains observed as fringes in the central part of figure 16.

Between the growth of slice E and that of slice I, the rate of growth of the $(0\bar{1}1)$ facet slowed, while the growth of the (101) facet increased, causing a corresponding change in the shape of the related facets as abstracted in figure 22. The change in the orientation of the central figures indicates that the slope of the central near-(001) face underwent a corresponding change. By the time that the center of the boule had grown to position K, however, growth of the (101) facet had ceased completely, causing distinctive correlated high strain regions in both slices I and K, and associated further change in the orientation of the central strain fringes, figures 22 and 23, respectively.

Specific aspects of this nonconstant faceted growth model are verified in magnified portions of the diffraction images, figures 24 and 25. Figure 24 illustrates continuity between fringes observed in the central region and the peripheral striations, supporting the faceted growth model where growth of the central facet is at a slight angle to the (001) plane. Cessation in the growth of the (101) facet while the (011) facet continued to grow is illustrated in figure 25.

The principal elements of a mathematical model that successfully predicts flow during stable Czochralski growth for a flat interface [19] are illustrated schematically in figure 26. An outer flow cell is established by convective heating of the crucible, while an opposing inner flow cell is established by rotation of the growing boule. The general features of this mathematical model have been verified experimentally [19]. However, the asymmetrical faceted growth found in the diffraction images requires a modification in this model. The development of facets influences, and in turn is influenced by, changes in the position of the boundary between the two flow cells, indicated in figure 27. The changes in flow are associated with corresponding changes in the temperature of particular growing regions of the boule and hence control the growth morphology.

6. Devices

Modification in materials that can be observed after an additional stage of processing in the manufacture of a device is illustrated in figure 28. This image shows strains in a piece of lithium niobate indiffused with titanium. Such regions of the crystal will guide light to be switched or modulated by electrodes that have yet to be installed. Observations can be made first on a virgin material and at various stages in the finishing of the crystal and subsequent processing of a device in order to identify the stages at which critical defects are introduced. Another example is the observation of EL2

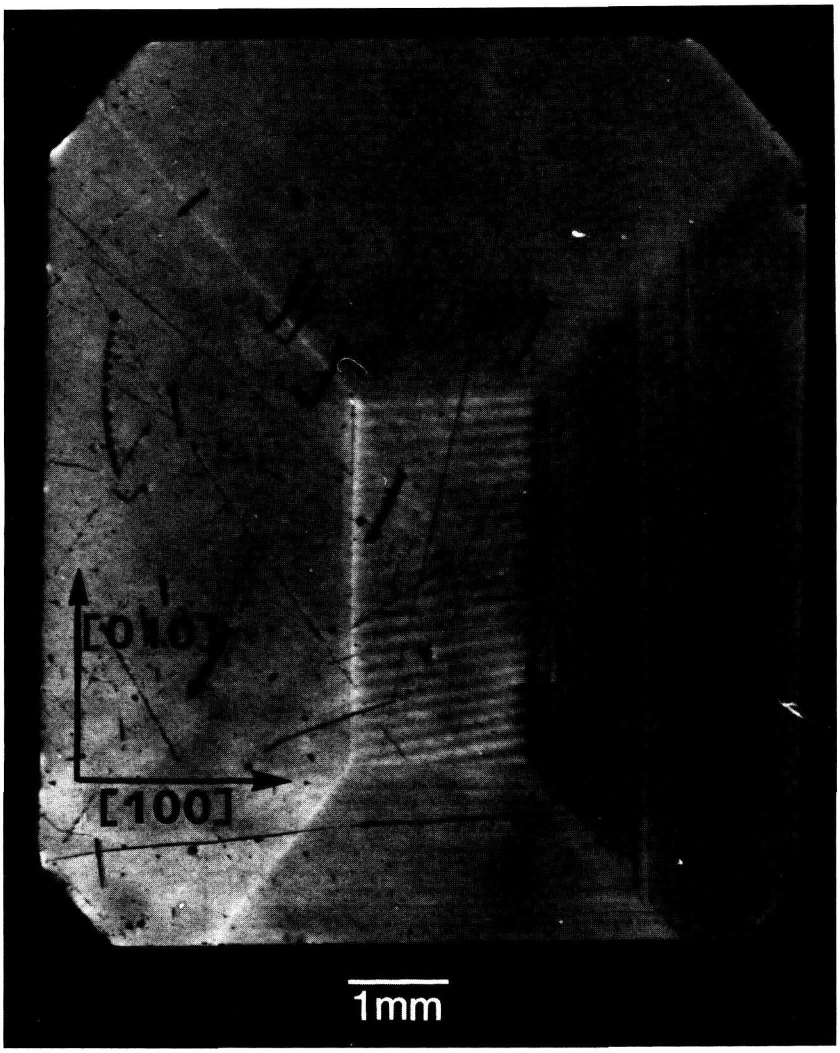

Figure 16. Diffraction image in Bragg geometry of (001)-cut slice E of bismuth silicon oxide from (006) planes at 8 keV.

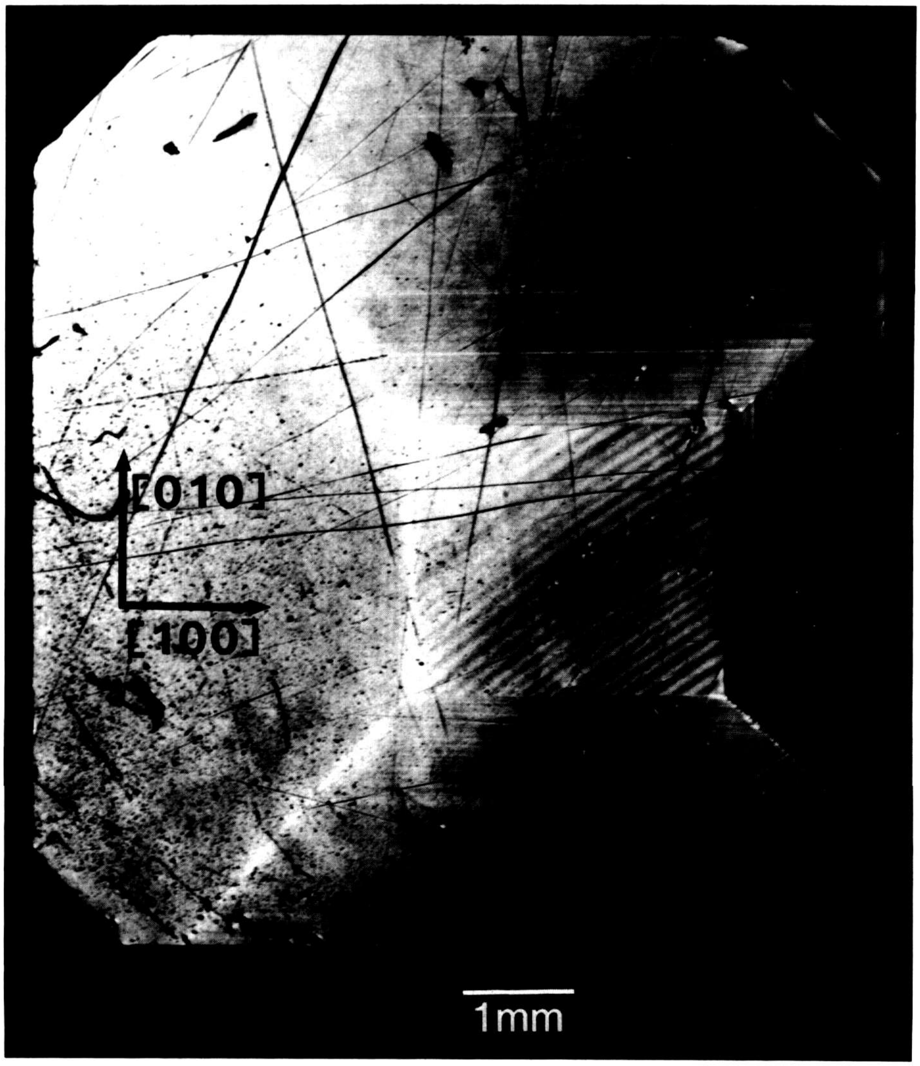

Figure 17. Diffraction image in Bragg geometry of (001)-cut slice I of bismuth silicon oxide from (0 0 10) planes at 8 keV.

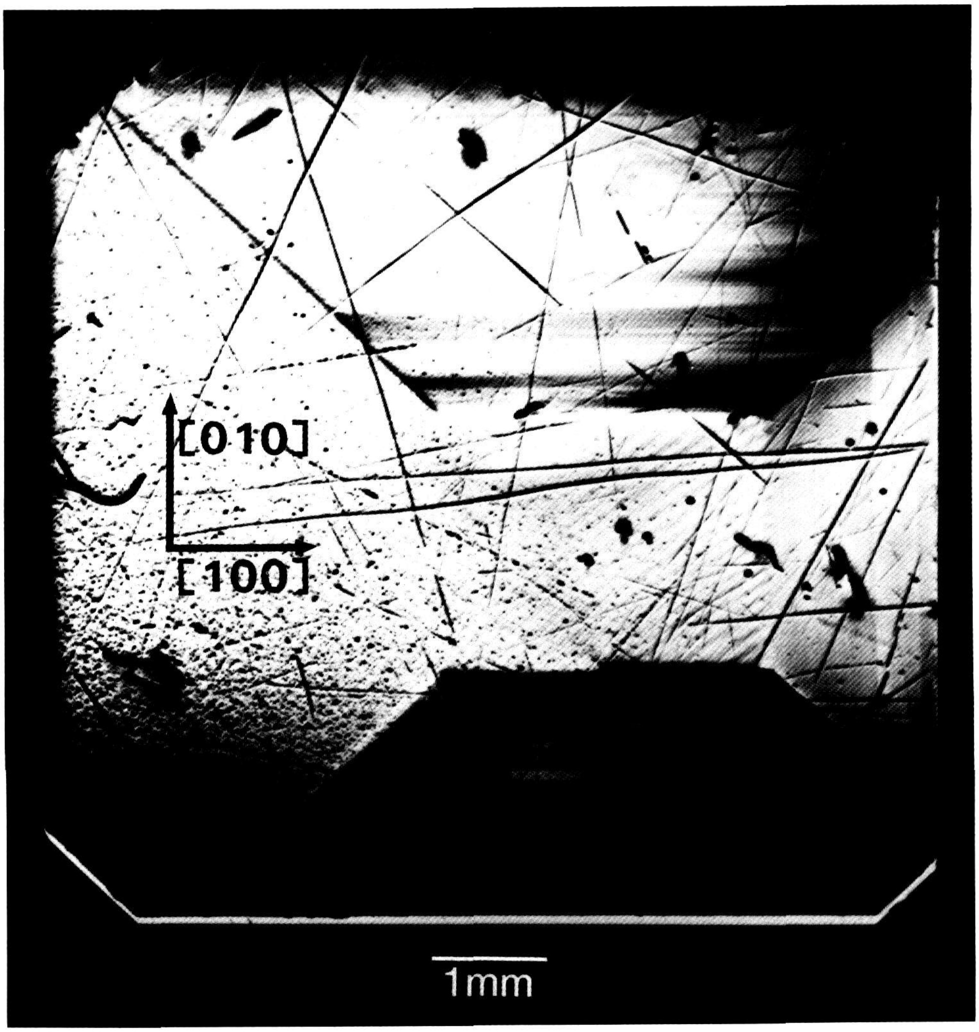

Figure 18. Diffraction image at 13.4 keV in Laue geometry from $(0\bar{6}0)$ planes of bismuth silicon oxide slice I, shown in Bragg geometry in figure 14.

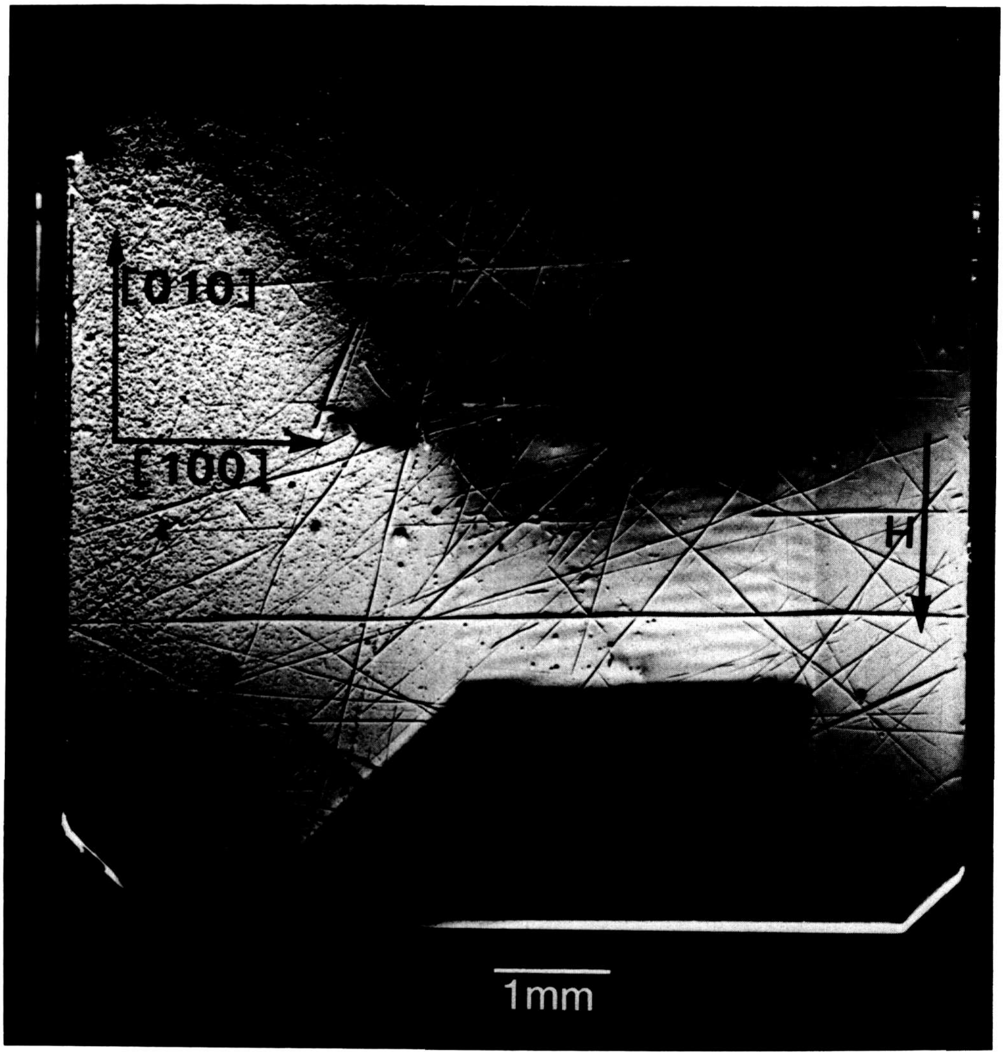

Figure 19. Diffraction image in Laue geometry of bismuth silicon oxide slice K from $(0\bar{6}0)$ planes at 13.4 keV. This crystal is shown in Bragg geometry in figure 1 and in another orientation in Laue geometry in figure 4.

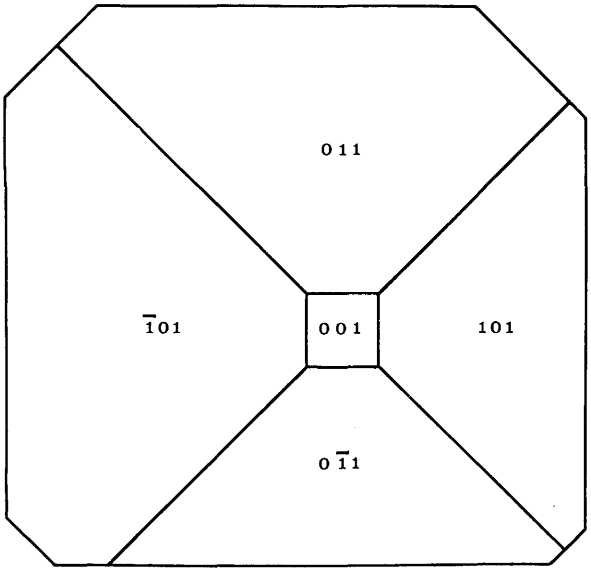

Figure 20. Abstraction of face of growing bismuth silicon oxide boule shortly after initial necking.

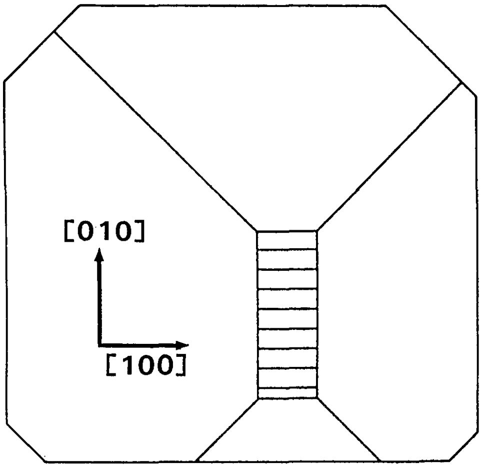

Figure 21. Abstraction of faceted growth of bismuth silicon oxide boule while slice E was being formed.

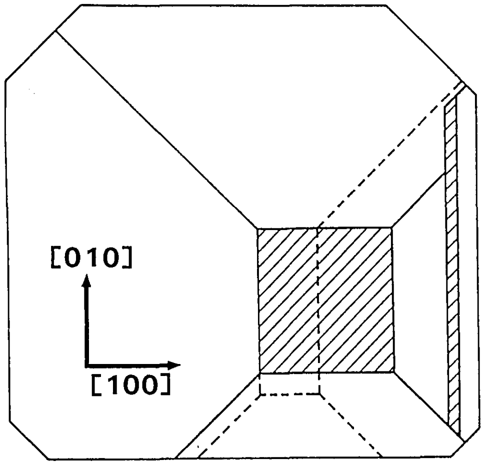

Figure 22. Abstraction of faceted growth of bismuth silicon oxide boule while slice I was being formed.

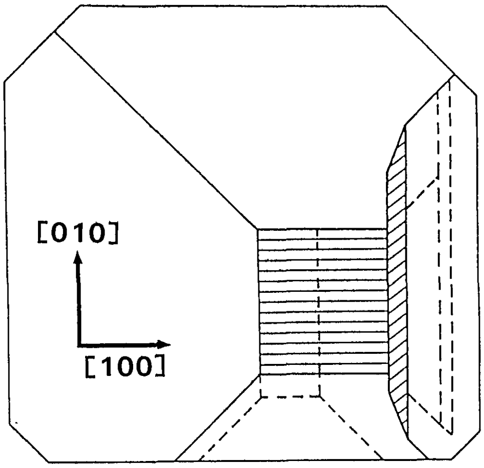

Figure 23. Abstraction of faceted growth of bismuth silicon oxide boule while slice K was being formed.

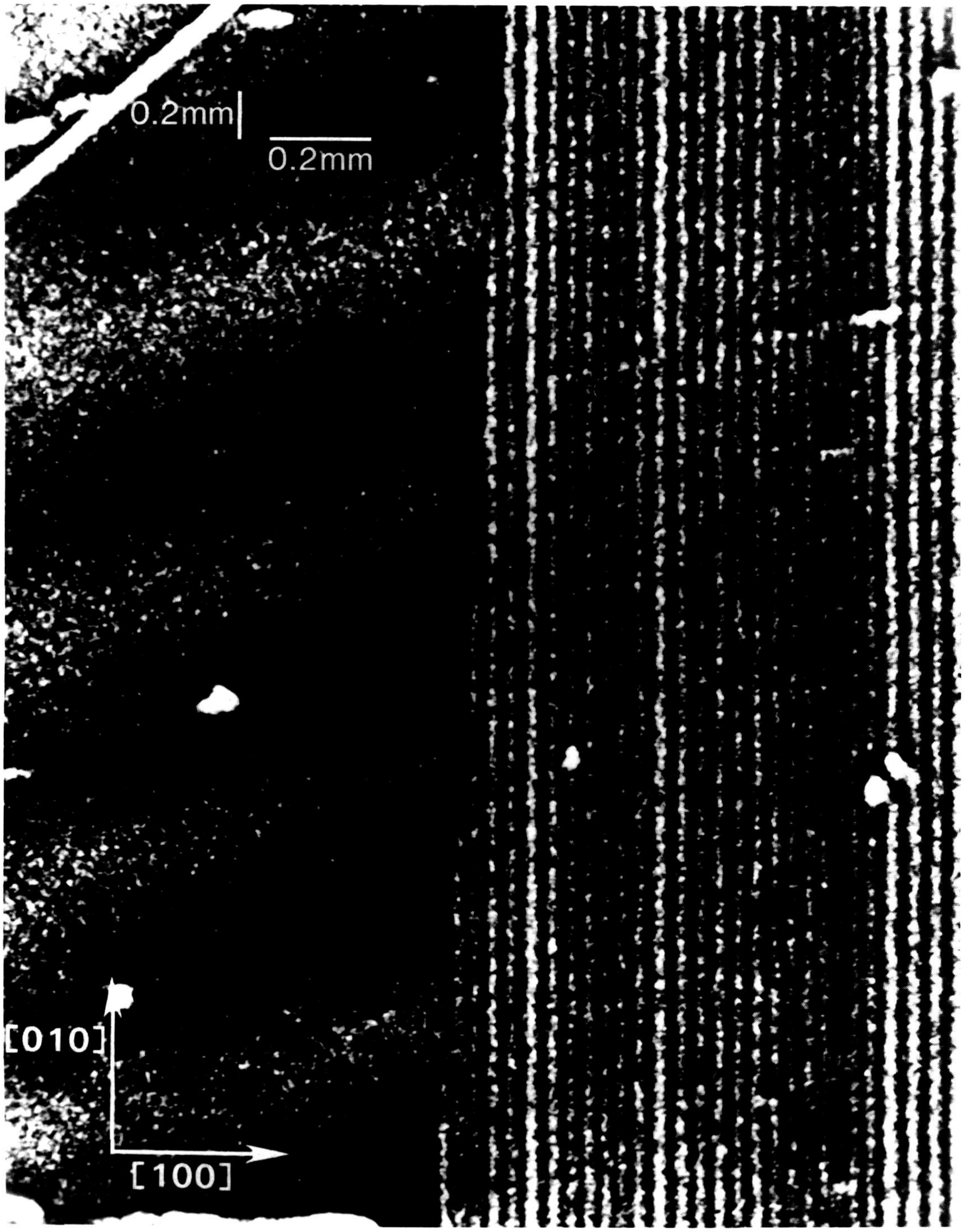

Figure 24. Magnification of region adjacent to the center, in the [100] direction, of a (006) diffraction of slice I in Bragg geometry at 8 keV. This section shows the boundary between the central rectangular near (001) facet growth region containing fringes and the peripheral (101) facet growth.

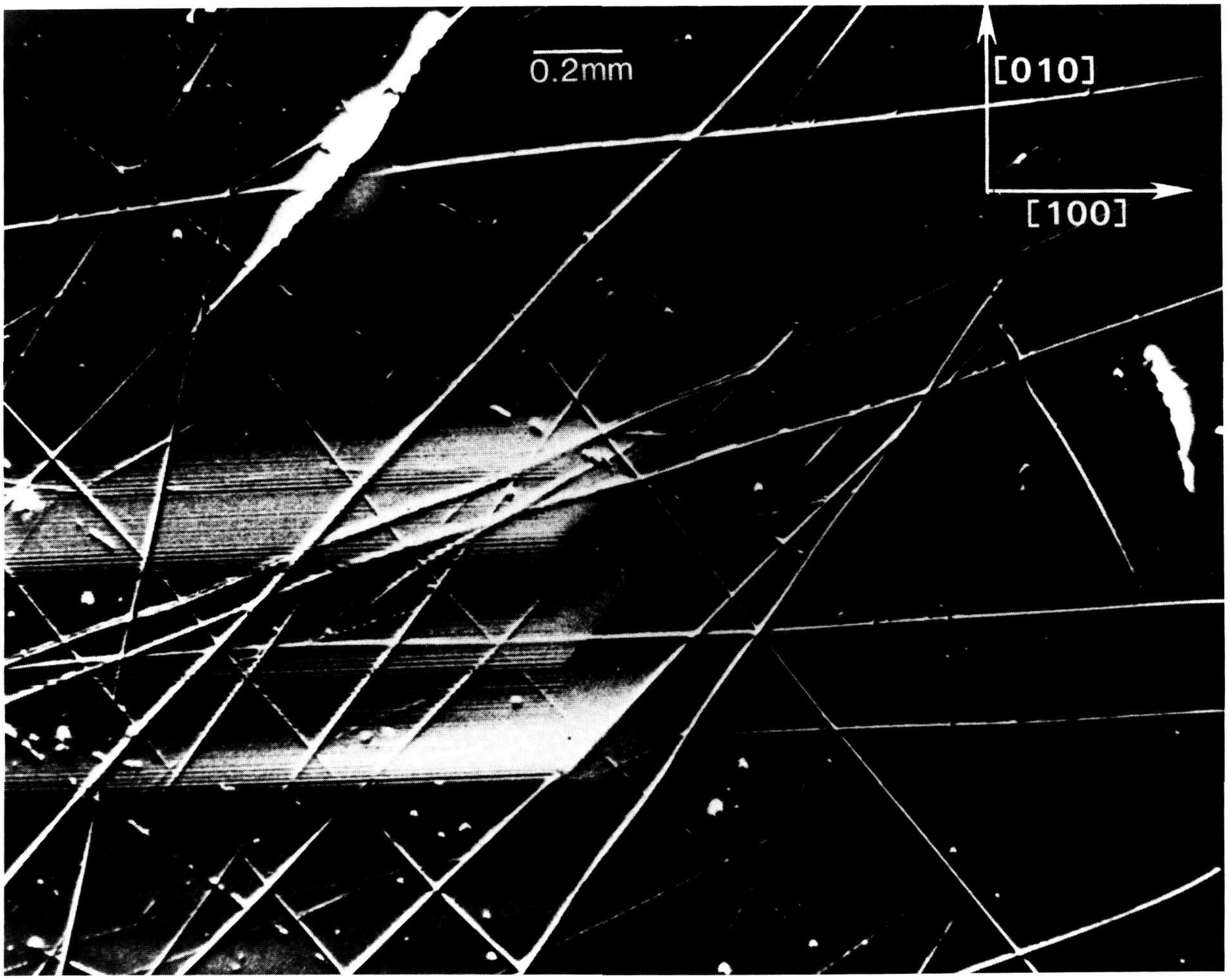

Figure 25. Magnification of the [110] corner region of a (0$\bar{6}$0) diffraction image of slice K in Laue geometry at 13.4 keV. This image shows strains in the [010] direction, and thereby the cessation in the growth of one of the facets while an adjacent facet continued to grow.

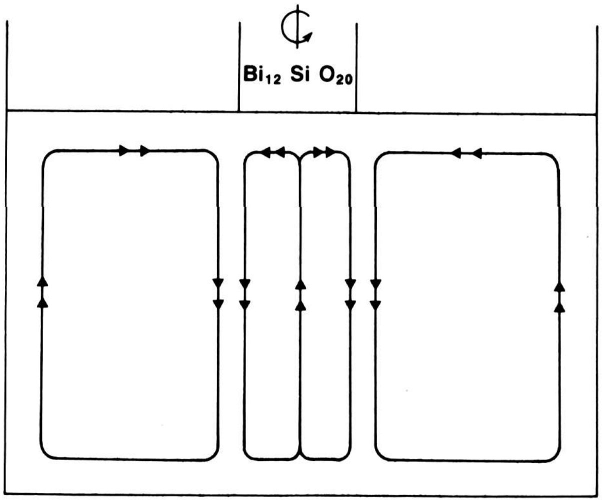

Figure 26. Schematic illustration of basic elements in a model for the flow in the bismuth silicon oxide melt as modified for stable flat interface Czochralski growth.

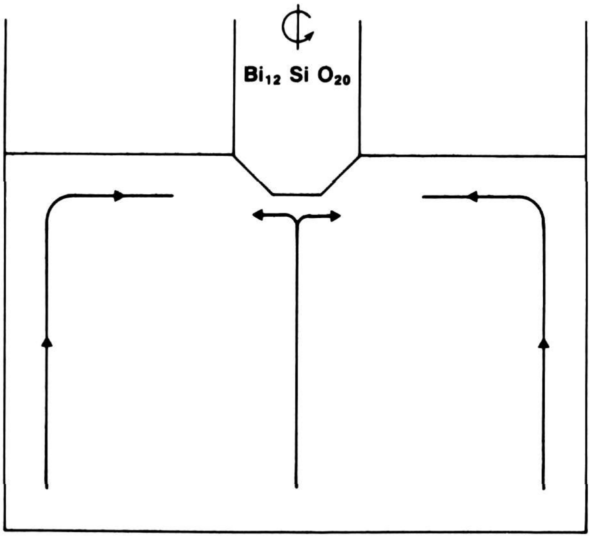

Figure 27. Schematic illustration of basic elements in the model for the flow in the bismuth silicon oxide melt as modified for faceted interface Czochralski growth. Competition between the two melt currents causes changes in the relative rates of growth of the various facets.

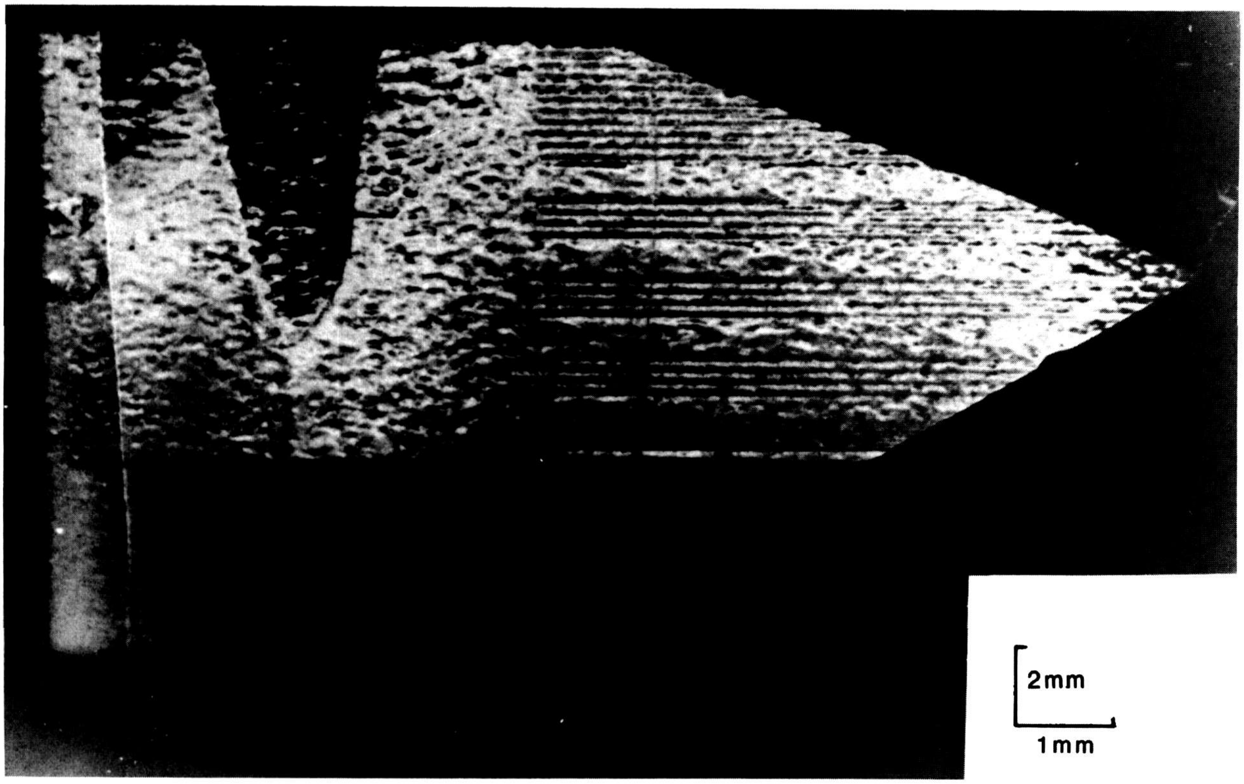

Figure 28. Diffraction image of titanium indiffused lithium niobate showing strains caused by this stage in the manufacture of a guided wave device.

defects, which control the electrical compensation of semi-insulating materials such as gallium arsenide, and their correlation by laboratory topography with dislocation density [18].

7. Future Directions

While imaging with monochromatic radiation removes ambiguity associated with diffraction of white radiation having a range of wavelengths, some ambiguity in the interpretation nevertheless remains. Contrast in a monochromatic image can be caused either by lattice parameter variations or by variation in orientation of the crystal lattice. Moreover, because of differing diffraction (scattering) angles, radiation from a defect appears in an image displaced from the image of the immediately surrounding undisturbed region. Diffraction from a surface defect surrounded by a perfect crystal is illustrated schematically in figure 29, in which spatial confusion in the diffracted image is shown and is clearly traceable to dissimilar diffraction (scattering) angles. Separation of the diffracted radiation from the two sources, defect and surrounding region, and removal of the ambiguity in the source can be accomplished by "out state analysis" through placing an additional analyzing crystal so as to intercept the diffracted image, as illustrated in figure 8, where an analyzing crystal is depicted in "symmetrical diffraction." Examples of the results of such "out state analysis" are shown in figures 30 and 31, which picture images of the central region of the indium doped gallium arsenide crystal previously shown in conventional diffraction images in figures 2, 3, and 13.

When the analyzer crystal is set to pass "perfect crystal" diffraction, the contrast between diffracting and non diffracting regions is relatively high. This high contrast is caused by the interaction between the beam in perfect crystal diffraction and the beams scattered from defects. When the analyzer crystal is set to discriminate against this "perfect crystal" diffraction from the matrix, the image is then restricted to the scattering from the defects. Analysis of such simplified images should prove to be more direct and thus less subject to models of defect location than is the analysis of conventional diffraction images.

Another opportunity with monochromatic synchrotron radiation not yet fully exploited is the ability to carry out experiments in real time while observations are made with a video camera. One example whose feasibility has been proved is the observation of changes in the strain in electrooptic crystals as various electromagnetic fields are applied. Strains have been observed in real time in lithium niobate as electrostatic fields are applied [20]. These strains are highly nonuniform, relax with time, and display hysteresis.

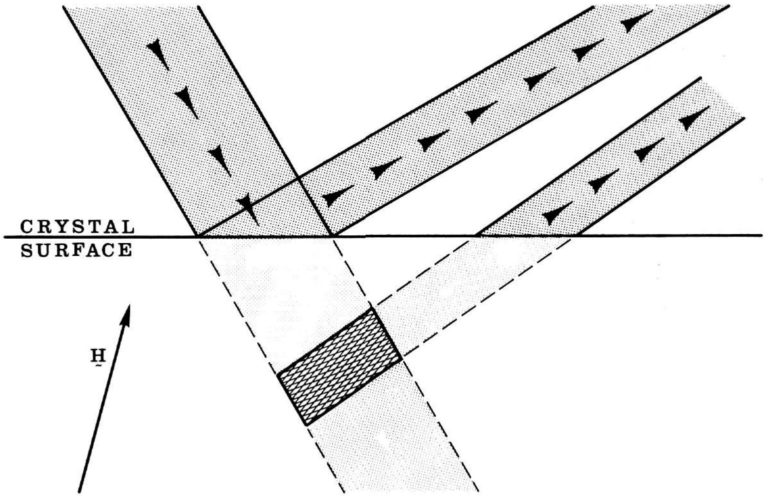

Figure 29. Schematic diagram of sources of image confusion caused by the unfortunate combination of defect strain and lattice orientation.

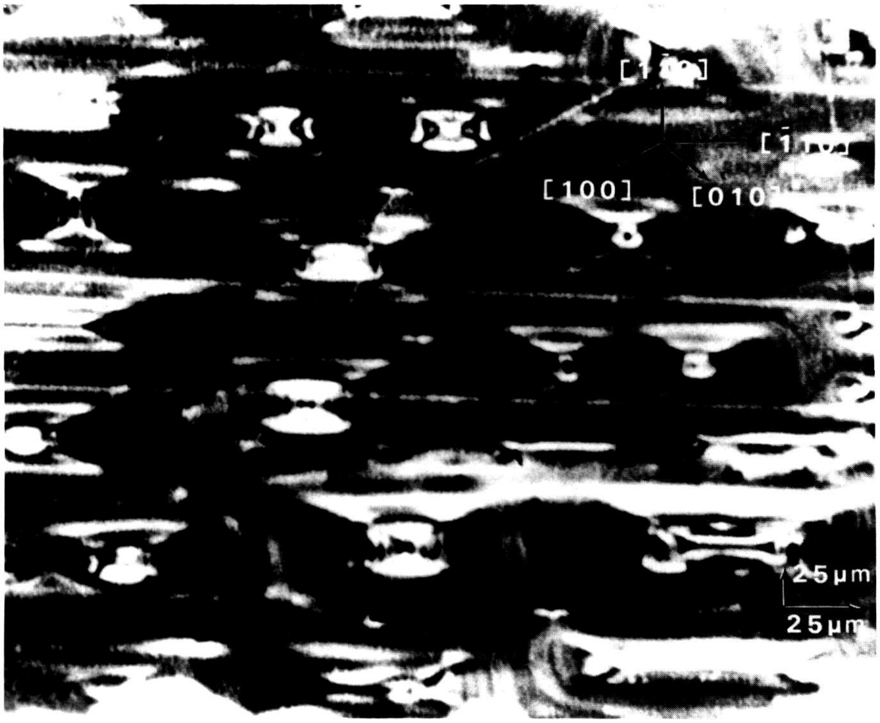

Figure 30. Magnified portion of (004) diffraction image of central portion of (001)-cut indium doped gallium arsenide wafer as diffracted by a silicon crystal oriented to pass the "perfect crystal" diffraction and to discriminate against defects.

Figure 31. Magnified portion of (004) diffraction image of central portion of (001)-cut indium doped gallium arsenide wafer as diffracted by a silicon crystal oriented to pass diffraction from defects and to discriminate against "perfect crystal" diffraction.

In summary, diffraction imaging can provide a great deal of insight into the physics and formation of electrooptic, photorefractive, and gamma ray sensitive crystals. Through exploitation of these opportunities, we expect to expand our understanding of the role of defects, which may either reduce or enhance the physical properties of these materials. Through collaboration with crystal growers, we can thus optimize these parameters through increase in the incidence and character of those defects that can be utilized and reduction of those that interfere.

8. Acknowledgments

The authors acknowledge the support of the U.S. Department of Commerce and of the National Aeronautics and Space Administration, through the Center for the Developement of Crystal Growth in Space. The NBS Materials Science synchrotron radiation beamline is located at the National Synchrotron Light Source at Brookhaven National Laboratory, which is supported by the U.S. Department of Energy, Division of Materials Sciences (DOE contract number DE-AC02-76 CH00016).

About the authors: Masao Kuriyama is leader of the Synchrotron Radiation Group of the Institute for Materials Science and Engineering at NBS. Bruce Steiner and Ronald C. Dobbyn are scientists in that group. They all divide their time between Gaithersburg and the National Synchrotron Light Source at Brookhaven National Laboratory, where they have specially instrumented a beam line to perform materials science work such as described in the article. Uri Laor, a scientist at the Nuclear Research Center in Beer Sheva, was a visiting scientist in that group.

9. References

[1] Turnbull, D., Ann. Rev. Mater. Sci. **13**, 1 (1983).
[2] Kuriyama, M., Boettinger, W. J., and Cohen, G. G., Ann. Rev. Mater. Sci. **12**, 23 (1982).
[3] Steiner, B., Laor, U., Kuriyama, M., Long, G. G., and Dobbyn, R. C., J. Cryst. Growth **87**, 79 (1988).
[4] Kuriyama, M., Boettinger, W. J., and Burdette, H. E., Real Time Radiologic Imaging: Medical and Industrial Applications, ed. by D. A. Garrett and D. A. Bracher, ASTM Special Tech. Publ. 716, ASTM, Philadelphia, PA (1980) p. 113.
[5] Spal, R., Dobbyn, R. C., Burdette, H. E., Long, G. G., Boettinger, W. J., and Kuriyama, M., Nuclear Inst. Methods **222**, 189 (1984).
[6] Kuriyama, M., Dobbyn, R. C., Takagi, S., and Chow, L. C., Med. Phys. **14**, 968 (1987).
[7] Kuriyama, M., in Advanced Techniques for Microstructure Characterization, ed. T. R. Anatharaman and R. Krishnan, Aedermannsdorf, Switzerland (1988).
[8] Boettinger, W. J., Burdette, H. E., and Kuriyama, M., Applications of X-Ray Topographic Methods to Materials Science, ed. S. Weissmann et al., Plenum Press, NY. (1984) p. 283.
[9] Boettinger, W. J., Burdette, H. E., and Kuriyama, M., Rev. Sci. Instr. **40**, 26 (1979).
[10] Boettinger, W. J., Dobbyn, R. C., Burdette, H. E., and Kuriyama, M., Nucl. Instr. Meth. **195**, 355 (1982).
[11] Kuriyama, M., J. Phys. Soc. Jpn. **23**, 1369 (1967).
[12] Kuriyama, M., J. Phys. Soc. Jpn. **25**, 846 (1968).
[13] Kuriyama, M., and Long, G. G., Applications of X-Ray Topographic Methods to Materials Science, ed. by S. Weissmann et al., Plenum Press, NY (1984) p. 97.
[14] Dobbyn, R. C., and Yoo, K. C., ibid. p. 241.
[15] Ishikawa, T., Kitano, T., and Matsui, J., J. Appl. Cryst. **20**, 344 (1987).
[16] Armstrong, R. W., Boettinger, W. J., and Kuriyama, M., J. Appl. Cryst. **13**, 417 (1980).
[17] Derby, J. J., Brown, R. A., Geyling, F. T., Jordan, A. S., and Nikolakopoulou, J. Electrochem. Soc. Solid-State Sci. Tech. **132**, 470 (1985).
[18] Kuwamoto, M. and Holmes, D. E., Defect Recognition and Image Processing in III-V compounds II, ed. E. R. Weber, Elsevier Science Publishers B. V., Amsterdam (1987) pp. 15–23.
[19] Whiffin, P. A. C., Bruton, T. M., and Brice, J. C., J. Crystal Growth **32**, 205 (1976).
[20] Laor, Uri, et al., unpublished work.

Volume 93, Number 5, September–October 1988
Journal of Research of the National Bureau of Standards

Convective Velocity Effects on a Thermistor in Water

Volume 93 Number 5 September–October 1988

Steve R. Domen

National Bureau of Standards
Gaithersburg, MD 20899

Electrical powers from 5 to 150 μW were dissipated in a thermistor, causing it to rise to equilibrium temperatures above the stagnant surrounding water. Natural convection was then simulated by forced convection of water flowing up or down at known rates from 1.3 to 17 mm/min. The disturbances of the equilibrium temperatures were measured, and are presented as effects of equivalent absorbed dose and absorbed dose rates, positive and "negative."

Key words: absorbed dose; calorimeter; convection; convective velocity; plume; point source heater; thermistor; water.

Accepted: April 14, 1988

1. Introduction

Because water has absorption properties for ionizing radiation similar to biological tissue, it has been chosen as the standard reference material for radiation therapy [1]. Therefore, the absorbed dose[1] water calorimeter was devised [2] and developed [3] for investigative studies concerning its use as a reliable standard for the calibration of instruments. One reason for the seemingly great delay in initiating such a calorimeter appears to have been concerns about the complexities of convection and its effect on the accuracy of measuring absorbed dose. Although convection at the point of measurement can be reduced or eliminated by the application of barriers [3] or by operating the calorimeter at 4 °C [4], it is of fundamental interest not only to better understand the water calorimeter, but also to understand convection in a system where there is essentially a free flow of water. The few observations reported (in an absorbed dose water calorimeter) are by the authors of reference [4] (who also operated their calorimeter at 30 °C) and by Barnett [5]. For a water calorimeter operated at ambient temperature or higher, it is valuable to know the best operational procedures to employ in order to reduce undesirable effects as much as possible. With the help of this knowledge and the use of convective barriers in the vicinity of the sensing thermistor, convective effects can be minimized to the point where they are likely to be insignificant.

A vast amount of theoretical and experimental work on convection has been reported in the field of fluid mechanics. The most successfully used instrument for measuring small velocities is the hot-wire anemometer (1–3 mm long and 5–10 μm in diameter). However, the calibration of this instrument is difficult and special apparatus is required. The lowest velocity at which it has been calibrated was about 8 mm/min [6]. A later work is also described [7], and several difficulties of its use in water are pointed out [8]. Depending on irradiation conditions and position of measurement in a barrier-free water calorimeter, the convective velocity

---

[1] Absorbed dose is the energy per unit mass imparted to matter by ionizing radiation. The SI unit of absorbed dose is the gray (symbol Gy). 1 Gy=1 J/kg.

could vary from zero to about 10 mm/min. Even if a small velocity could be measured accurately, there would still remain the important problem of determining the effects of convection on the accuracy of measurement of absorbed dose with a temperature-calibrated thermistor. The equilibrium temperature rise could be significantly disrupted by the motion of the water.

To circumvent the above difficulties, a thermistor was used both as a temperature-measuring device and as a velocity-measuring device. Its velocity sensitivity is significantly greater than that of the hot-wire anemometer.

In the present investigation, natural convection was simulated by forced convection of water flowing around a thermistor over a wide range of known water velocities and thermistor powers. The changes in thermistor temperature were measured and are presented as the effect of an equivalent absorbed dose or absorbed dose rate, quantities of direct interest to those in the field of radiation dosimetry. A conversion factor can be used to rescale the results in terms of temperature.

2. Sources of Convective Effects

Dissipation of electrical power in the thermistor will cause it to rise to an equilibrium temperature above that of the surrounding stagnant water, which might be either uniform or nonuniform in temperature. Irradiation of the water will produce temperature gradients which are the driving force of convection, and which may set it into motion.

Measurement errors due to convection as a result of irradiation may then arise in two ways: (1) if the background temperature of the water is uniform, the motion of the water may disturb the equilibrium temperature rise of the thermistor, and (2) if the background temperature of the water is nonuniform, an additional disturbance may result from a temperature difference between the water entering and leaving the region of the thermistor. The study of effect (1) is the main purpose of this investigation. Applications will be described elsewhere [9].

Nonuniform temperature distribution in the water may have two causes: (a) a significant variation of absorbed dose rate in the vicinity of the thermistor from previous runs, and (b) conduction of heat between the calorimeter and surroundings. Cause (b) can be reduced by placing an enclosure around the calorimeter to circulate the air and regulate it within 0.1 °C. Such a simple enclosure was used and has been previously recommended [3]. Any remaining temperature gradients, caused by either (a) or (b), can be rapidly and effectively erased by simply agitating and circulating the water between runs. A significant observed drift is a good indication that this needs to be done.

3. Setup

Figure 1 shows a sketch of the experimental setup. A calibrated thermistor (which formed one arm of a Wheatstone bridge) was positioned on the vertical axis of a two-piece plastic tube, 3 cm inside diameter. The tube was supported in a calorimeter container C filled with once-distilled water. Plastic tubes connected C to an elevated water reservoir R and a column of water where micrometer measurements were made to its surface.

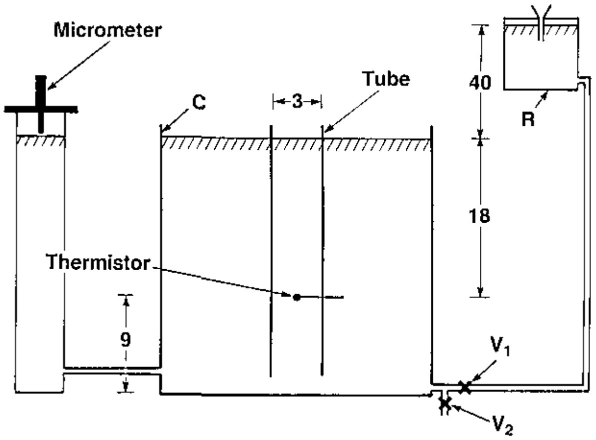

Figure 1. Experimental setup for simulating water convection to study the change in thermistor equilibrium temperature and the resulting effect on a measurement of absorbed dose or absorbed dose rate. The drawing is not to scale. The dimensions are in centimeters.

C was surrounded by thick insulation consisting of expanded polystyrene (for further details see figs. 3 and 5 in [3]). The desired uniform temperature in C was achieved with immersion heaters and circulating the water with air, which bubbled upward along the four vertical edges of C. Thermistor probes in C, R, and the room sensed temperatures, which were displayed with a resolution of 0.01 °C.

The large cross-sectional area of R (1,400 cm^2), helped to maintain a sufficiently constant flow of water. The instantaneous initial and final surface velocities S_v in C differed by 1 to 5%, as a result of changes in water level heights (about 3 to 13 mm in C).

Measurements were made of the average surface velocities $\bar{S}_v$, rise or fall. This was then used to determine the average axial water velocity $\bar{A}$, along the tube axis. (This is discussed below in section 6, $\bar{S}_v \neq \bar{A}_v$). $\bar{S}_v$ ranged from 1.3 to 10 mm/min. $\bar{S}_v$ (rise) was determined from the initial and final micrometer measurements and a measured time interval, from the time when the ball valve V_1 was suddenly opened to when it was closed. $\bar{S}_v$ (fall) was determined in a similar manner but by operating ball valve V_2; and, instead of the micrometer measurements, it was determined from the measured mass of water withdrawn and the cross-sectional areas of C (927 cm^2) and the water column (16 cm^2). The water lines contained other valves (not shown), which were pre-adjusted to give desired rates of water flow when V_1 or V_2 was opened.

4. Preparation

Initially the water was circulated with air and the immersion heaters were turned on until the water was heated to room temperature (regulated within about ±0.2 °C). This procedure minimized subsequent internal temperature drifts. The temperature of the stagnant water within the tube lagged behind that of the surrounding agitated water. To speed approach to uniformity of temperature of the entire water volume and of the two-piece tube, the upper part of the tube was detached (a few centimeters above the thermistor plane) and placed in a corner of C where water flowed vigorously within and without that part of the tube. At the same time, the motion of the water reduced the time to achieve uniformity of temperature in the lower part of the tube (still in position). About 30 minutes later the two parts were rejoined. Several minutes later the air supply was turned off and the water became stagnant. During the above procedure, the agitated water in R had been adjusted in temperature until it was observed to be the same as that in C.

5. Procedure

To assure repeatability of water velocities, the heights of the water levels in C and R were restored prior to a run. For example, to simulate upward convection, V_1 was opened, which caused water levels in C and R to rise and fall, respectively. After the run, the amount of water that had entered C was withdrawn through V_2 and replaced in R. To simulate downward convection, V_2 was opened, lowering the water level in C. The water withdrawn was then poured into R, and V_1 was opened until the water levels were restored.

A procedure was also followed to assure temperature stability as much as possible. If successive runs were made, following the above procedure alone, increased temperature instabilities would result because of small temperature differences of the water flowing into C. This would result in (1) temperature drifts caused by heat conducted toward or away from the tube axis, and (2) a temperature gradient along the tube axis, which is of more concern. Therefore, when the levels were restored after each run, the water in C was agitated for several minutes. This assured an essentially uniform temperature distribution along the outside of the tube and an eventually more uniform temperature along the tube axis. The motion of the water, however, did cause a significant disturbance in the thermistor equilibrium temperature, but after agitation equilibrium was restored within 10 minutes.

It is, however, still desirable to reduce the relatively uniform rate of heat conduction to or away from the entire tube axis. The direction of the observed drift (cooling or heating) indicated that R needed a small amount of warm or cool water, followed by agitation; or an eyedropper of hot or ice water was directly injected into C and agitated. The result was a sluggish and delayed reaction, but nevertheless this procedure did significantly help to provide thermal stability. The remaining small drift signals were quickly reduced by making an adjustment with a resistance-capacitance circuit across the Wheatstone bridge [10]. As with other calorimeters, this circuit proved effective in producing an essentially zero initial drift signal.

6. Axial Water Velocity

In figure 1, the water surfaces (inside and outside the tube) rise or fall at the same rate, S_v. Although S_v will slowly change (because of the changing heights with respect to V_1 and V_2), we consider the ideal situation where S_v is constant.

During the slow laminar flow of a fluid in a tube, the velocity at the wall remains zero. As time increases from $t=0$, the velocity increases toward and along the tube axis, where it is greatest. At positions along the axis (sufficiently far from "end effects" of the water surface and the bottom end of the tube), the instantaneous axial velocity A_v will increase from S_v to $2S_v$. The vertical velocities within the tube build up to a parabolic distribution, as a function of radius. A detailed theoretical analysis is given by Szymanski [11]. A figure and a detailed table are presented in reference [11] which give the buildup velocity profiles as a function of time and radius. The figure is also presented in a more recent reference [12], p. 129. Reference [13], among many others, gives additional detailed information on fluid flow. Laminar flow occurs when the Reynolds number

$$Re=\frac{DV}{\nu}<2000 \ . \tag{1}$$

In equation (1) D=inside diameter, V=average velocity within the tube (V=S_v), S_v=surface velocity, and ν=kinematic viscosity. For the present experiment, D=3 cm, S_v=1 cm/min (the maximum velocity used), and ν=0.59 cm^2/min (at 21 °C, the operating temperature of the calorimeter). Substituting these values in equation (1) gives $Re \simeq 5$, well within the range for laminar flow.

In general, the velocity on the axis for any size tube varies approximately linearly with time from the initial value S_v up to $1.5S_v$. For the 3-cm-diameter tube used in this experiment, the theoretical times required for the buildup to reach 50 and 95% of the maximum are 0.53 and 2.1 min, respectively. Therefore, if at $t=0$ the surface velocity is S_v (and remains constant), then at those respective times the velocities on the central axis are $1.50S_v$ and $1.95S_v$. In reality (as mentioned previously) $\bar{S}_v$ is measured. In the data analysis, $\bar{S}_v$ is treated as an assumed constant S_v. Therefore, only S_v will be mentioned in the remainder of this paper.

The equilibrium temperature of the thermistor was, therefore, disturbed by a steady increase in axial water velocity. One phase of the measurements required measuring the average rate of temperature change in the thermistor (which can be considered as the effect of an equivalent absorbed dose rate) during a measured time interval. This was related to $\bar{A}_v$ during that interval. $\bar{A}_v$ was computed by use of S_v and an empirical fit to the theoretical data mentioned in reference [11], integrated over the time interval.

7. The Thermistor

The thermistor indicated in figure 1 is a commercially available, electrically insulated thermistor (uninsulated thermistors were extremely noisy). The nominal size of the bead was 0.25 mm. It had two platinum leads (18 μm in diameter, 1 mm long) soldered to paired nickel alloy leads (76 μm in diameter). The bead and the 18-μm diameter wires had a thin coating of resin, of variable thickness <25 μm. An improvement was made by applying a thin coat of silicone rubber which significantly increased the electrical resistance between those components and the surrounding water. The resulting outside diameter of the silicone coating around the bead was nearly 0.35 mm. The diameter of the commercial insulating sleeve around the paired 76-μm wires was 0.23 mm.

The performance of the thermistor was good throughout the experiment. The recordings (shown in figure 2 and subsequent figures) indicate good signal-to-noise ratios. After each day of measurement, the water in container C was drained and the support tube and its thermistor were removed and dried in the air-conditioned room.

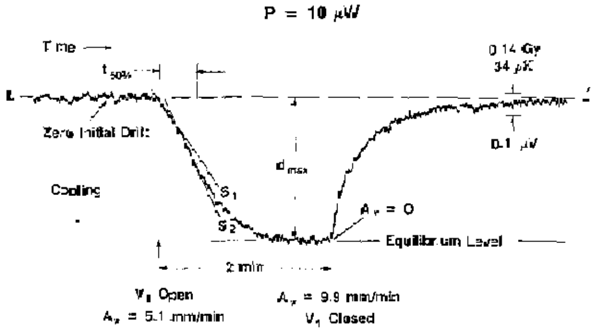

Figure 2. Typical response of a thermistor as a result of upward convection.

At a calorimeter operating temperature of 21 °C, the thermistor resistance was 2.6 kΩ and its measured resistance sensitivity was 3.7%/°C. From the measurements of its resistance as a function of temperature and power, the equilibrium temperature rise (ΔT) of the thermistor above that of the surrounding stagnant water was:

$$\Delta T=1.41\,P\ \mathrm{mK} \ , \tag{2}$$

where P=power in microwatts.

The value of ΔT could be significantly different for a different bead size and details of insulation. Measured results of convective effects are expected to vary directly with ΔT. Therefore, an experimenter should have a similar knowledge of a thermistor being used, in order to apply the results of this investigation. In general, it is good practice for experimenters to give an expression similar to eq (2) along with the thermistor powers which were used. Otherwise, the meaning of some reported results may be unconvincing to the readers.

The temperature calibration of the thermistor was also determined from the measurements of its resistance as a function of its temperature and power. This permitted calorimeter responses to be converted to temperature changes, described previously in detail [3].

8. Results

8.1 Upward Convection

Figure 2 shows a typical general response as a result of forced upward convection. In all cases, it was possible to preset the power to within an uncertainty of 0.1% and to produce an essentially zero initial drift. Valve V_1 was then suddenly opened, causing $S_v = A_v = 5.1$ mm/min. Convective cooling of the thermistor was instantaneous, because of its increased heat-transfer coefficient ([12], p. 409). Its cooling rate depended on A_v and power P, 10 μW for the run shown in figure 2. After 2 minutes, for this case, the thermistor response appears to be near equilibrium. At this time, the theoretical velocity buildup reached 94% of the maximum [11], giving a value of $A_v = 1.94 S_v = 9.9$ mm/min. Then V_1 was closed (rapidly causing A_v to drop to 0), which caused the thermistor to rise in temperature to its initial equilibrium value represented by the base line LL′. This is an indication that the background temperature of the water which left the vicinity of the thermistor was equal to that which entered that region. When this is not the case, the final trace will undershoot or overshoot LL′. Large effects like this were avoided by frequent agitation of the water and the preparation procedure (described in sections 1 and 4) to assure more uniformity in background temperature. Corrections were made for any of those small remaining effects caused by nonuniformity.

The scale on the right in figure 2 indicates the measurement sensitivity. The indicated absorbed dose or temperature change would have caused a 0.1-μV potential change in the output of the Wheatstone bridge, which was powered by a 1.35-volt mercury cell. The noise shown is approximately the greatest encountered for all values of power.

The thermistor response during water flow showed a wide range of characteristics, which varied with power and water velocity. Figure 2 shows an initial slope S_1 followed by a steeper slope S_2. Particularly at large signals caused by high powers (when the gain of the amplifier was reduced, resulting in little or no observable noise fluctuations), the transitional point from S_1 to S_2 in many cases appeared to be clear and abrupt; under some conditions there was more than one point of inflexion. Also, in many cases $S_1 > S_2$. The time to reach apparent equilibrium varied significantly.

The somewhat complicated response indicated by the recordings required some compromises in presenting the measured results. The recordings show two main characteristics: (1) a rate of change of response, and (2) a maximum deflection $d_{\max}$, represented by the indicated equilibrium level. At $d_{\max}$ the value of A_v assigned was $2S_v$. The quotient of $d_{\max}/2$ divided by the corresponding time interval is a measure of the rate of response up to 50% of $d_{\max}$. If $d_{\max}$ is expressed in terms of equivalent dose, then that quotient has the dimensions of a dose rate. While strictly speaking it is not an "average," it is in fact close to a true average, and it will be convenient here to refer to it as the average dose rate during the time interval $t_{50\%}$. That time interval appeared to be a reasonable choice, because beyond that point the signal began to decrease rapidly. The equivalent "negative" average absorbed dose rates $\dot{D}^-$ are plotted as a function of $\bar{A}_v$ during the time interval $t_{50\%}$.

A 1 mK rise in temperature is produced by an absorbed dose of 4.18 Gy, neglecting a heat defect. This conversion factor can be used to rescale the plotted results in terms of temperature.

Figure 3 shows a plot of individual points determined during a daily set of measurements, for $P = 25$ μW. The average $\dot{D}^-$, from 0 to 50% of equilibrium, is plotted as a function of the average axial water velocity. (The plots in the figures that follow do not show the individual points of measurements, for the sake of clarity.) Figure 4 shows plots of the approximate times for the thermistor to reach 50% of its temperature drop to equilibrium as a function of the equilibrium axial water velocity $2S_v$.

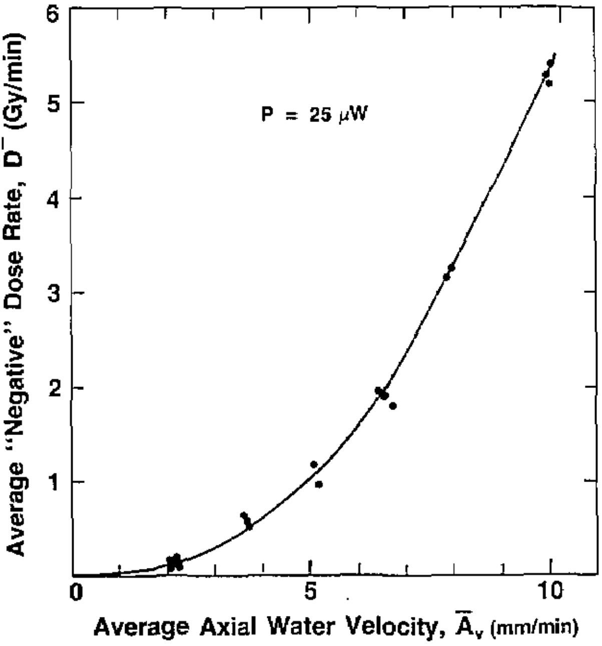

Figure 3. Plot of a daily set of measurements. The average "negative" absorbed dose rate $\dot{D}^-$, from 0 to 50% of equilibrium, is plotted as a function of the average axial water velocity $\bar{A}_v$ during the interval, $t_{50\%}$.

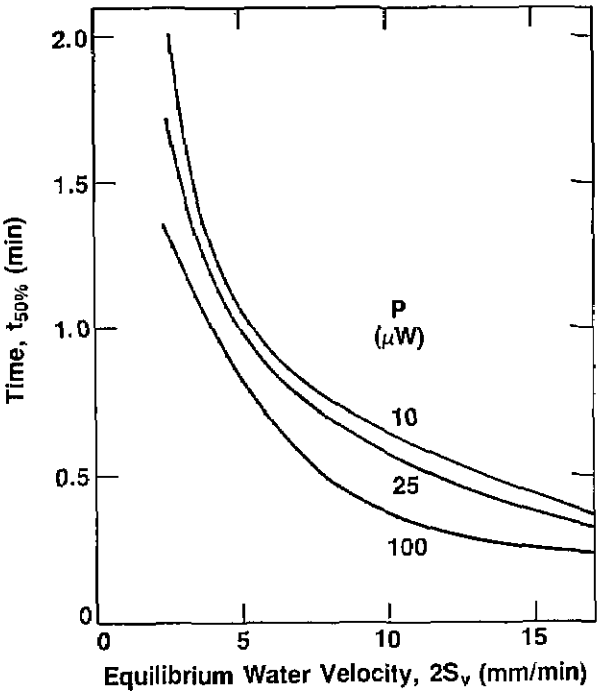

Figure 4. Plots of the time $t_{50\%}$ for the thermistor to reach 50% of its drop to equilibrium as a function of the equilibrium water velocity $2S_v$ along the tube axis.

Summaries of the measurements (for $P=5$ to 100 μW) are shown in figures 5, 6, and 7. An expanded scale of figure 5 (from $\bar{A}_v=0$ to 4 mm/min) is shown in figure 6. At low values of P and $\bar{A}_v$, $\dot{D}^-$ is very small. Therefore, the curves in those regions should serve only as a guide, because some subjectivity was used in extending the curves to zero $\bar{A}_v$ and $\dot{D}^-$. Figure 7 shows plots of the equivalent "negative" absorbed dose D^- at equilibrium as a function of the equilibrium water velocity $2S_v$ along the tube axis.

The smallest values of surface velocity and power were 1.3 mm/min and 5 μW, respectively. Six 2-minute runs were made in this condition. There appeared to be no detectable response to about 1.5 minutes. At the end of the run ($A_v=2.5$ mm/min), D^- was perhaps about 0.04 Gy. This was barely detectable, being just above the noise level. Figures 5 and 6 can be used in practice to estimate roughly the convective velocity produced by irradiation, by use of the initial and final drift rates of a recorded calorimeter run [9].

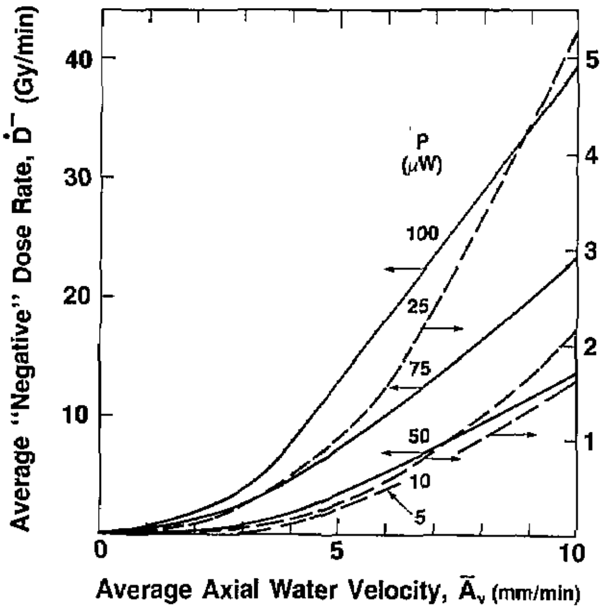

Figure 5. Summary of the measurements of the average "negative" absorbed dose rate $\dot{D}^-$ as a function of the average axial water velocity $\bar{A}$ during the time interval $t_{50\%}$.

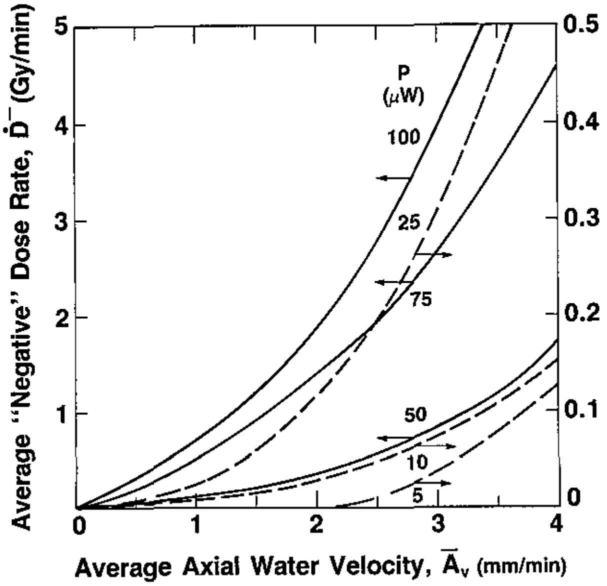

Figure 6. Expanded scale, from $\bar{A}_v=0$ to 4 mm/min, of the plot shown in figure 5.

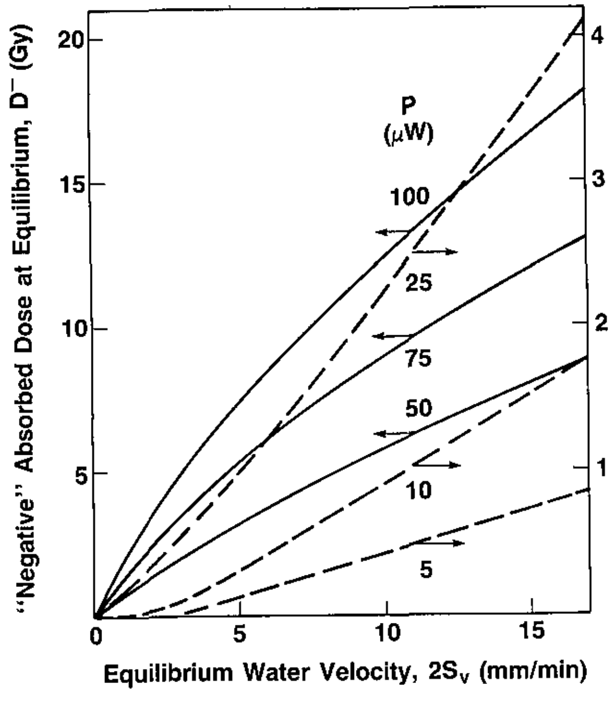

Figure 7. Summary of measurements of the equivalent "negative" absorbed dose D^- at equilibrium as a function of the equilibrium water velocity $2S_v$ along the tube axis.

8.2 Downward Convection

The investigation of downward convection started with initial values of $S_v=3.5$ mm/min and $P=30$ μW. The convective cooling of the thermistor had the same general shape as that shown for upward convection in figure 2. The same was noted when $P=40$ μW. Most of the time this appeared to be the case for $P=50$ μW, but occasionally (after V_2 was opened) there appeared to be a short and barely detectable heating response before convective cooling began. At $P=60$ μW the convective heating was clearly visible on nearly all occasions. It always appeared at higher values of power, and the response and duration increased with power. The power was varied up to 150 μW.

Figures 8, 9, and 10 show the development of the recordings when the initial velocity was varied, $P=80$ μW. Figure 10 may be compared with figure 11, where $P=100$ μW.

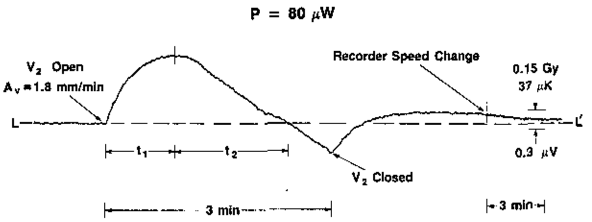

Figure 8. Thermistor response to downward convection, $P=80$ μW and $A_v=1.8$ mm/min at $t=0$.

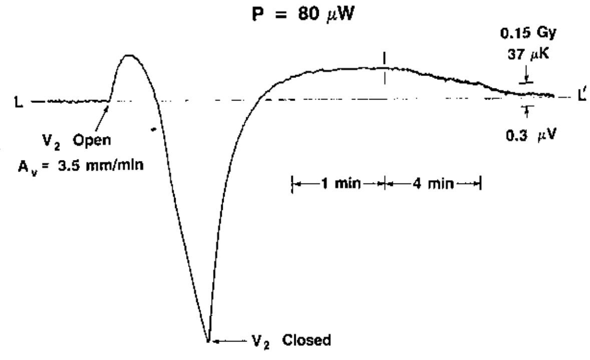

Figure 9. Thermistor response to downward convection, $P=80$ μW and $A_v=3.5$ mm/min at $t=0$.

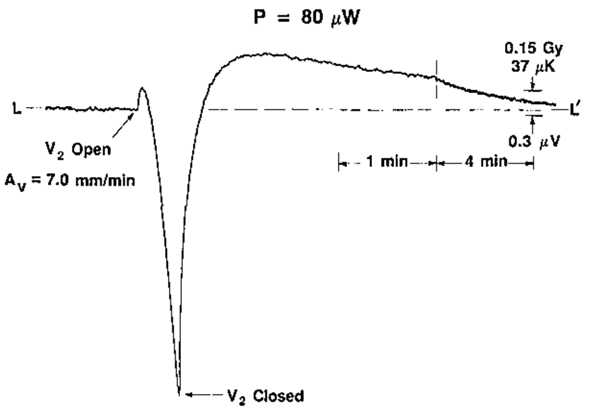

Figure 10. Thermistor response to downward convection, P=80 μW and A_v=7.0 mm/min at t=0.

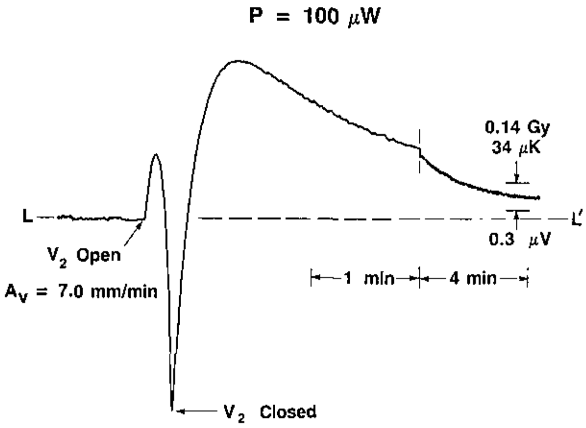

Figure 11. Thermistor response to downward convection, P=100 μW and A_v=7.0 mm/min at t=0.

Figures 12 and 13 show, respectively, summary measurements of the time interval t_1 and the equivalent absorbed dose D at the peak of response at the end of t_1, (see fig. 8) as a function of power. Figures 12 and 13 can be used for estimating the average equivalent absorbed dose rates $\dot{D}$ during t_1.

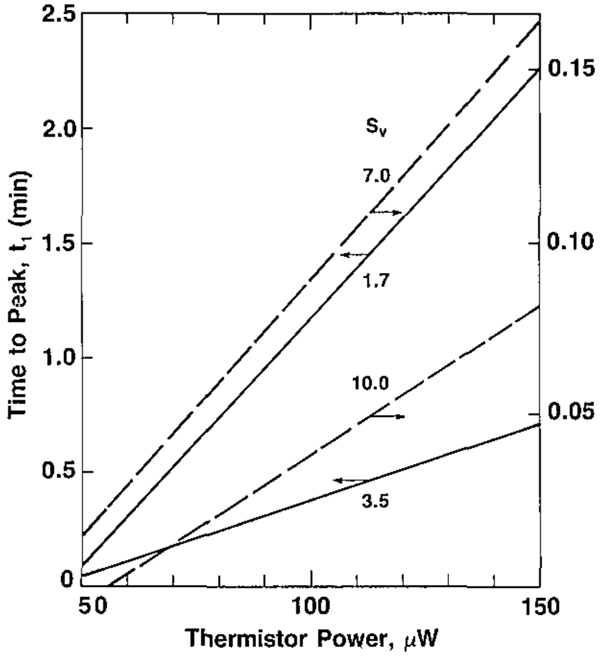

Figure 12. Summary of the measurements of the time t_1 to the peak of the temperature rise as a function of thermistor power. The surface velocity S_v is in mm/min.

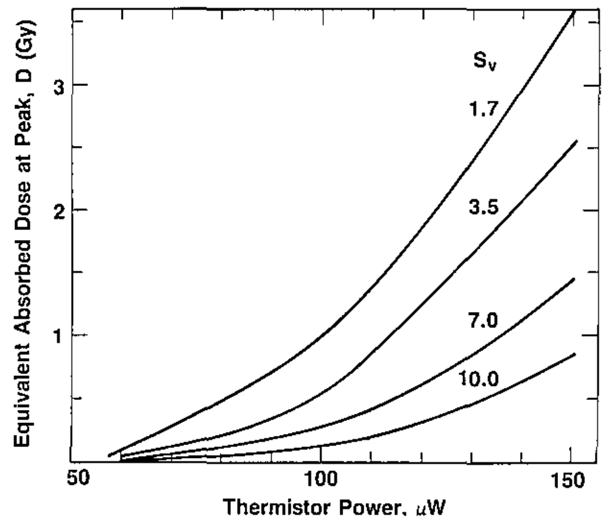

Figure 13. Summary of measurements of the equivalent absorbed dose D at the peak, at the end of time t_1, as a function of thermistor power. The surface velocity S_v is in mm/min.

A reason for the convective heating is postulated by use of the illustrations in figure 14. At low thermistor powers, figure 14(a), the temperature pattern around the thermistor is essentially symmetric, implying no or little convection. Movement of that pattern, either up or down, would increase the net temperature gradient in the immediate vicinity of the thermistor to cause it to cool. As the power is increased, *localized* convection will eventually occur, giving rise to a plume, figure 14(b). Forced upward convection would further increase the net temperature gradient, since the bottom of the plume would be forced nearer to the thermistor, and it would be expected that convective cooling of the thermistor would be observed. Downward convection will cause the plume to move down relative to the thermistor. This will initially result in a net decrease in temperature gradient, since the bottom end of the plume will be at a greater distance from the thermistor. This will decrease its heat transfer coefficient, causing the thermistor at least initially to rise higher in temperature. The magnitude of this effect will depend on the axial velocity. At a low velocity a longer time will be required for the plume to pass through the thermistor, causing a relatively long duration of convective heating.

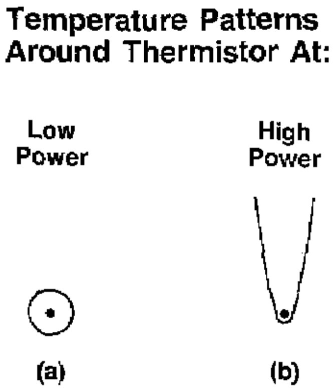

Figure 14. Illustrations of the equilibrium temperature patterns around a thermistor.

By the time the value V_2 was closed (figs. 8 to 11), the plume, figure 14(b), had descended downward, which caused heating of the water over an extended distance below the thermistor. This volume of water then ascended upward to cause a temperature overshoot before temperature equilibrium LL′ was attained.

Figure 15 shows plots of the apparent plume height as a function of power. This is the product of t_1+t_2 and $\bar{A}_v$ during that interval. For a given value of power, the results show a wide variation in the apparent plume heights. When $S_v=1.7$ mm/min, the runs from 100 to 150 μW showed that the signal was well above the base line LL′, when V_2 was closed. The results of those runs could not be shown, because they do not have the required time interval t_1+t_2. When $S_v=3.5$ mm/min, a large change in effect was seen. The change is still significant when $S_v=7.0$ mm/min. A still significant but smaller change was noted when $S_v=10.0$ mm/min.

It can be seen that the curves in figure 15 do not converge rapidly. Therefore, no definite conclusions can be drawn from this information, which is presented merely to show this type of behavior.

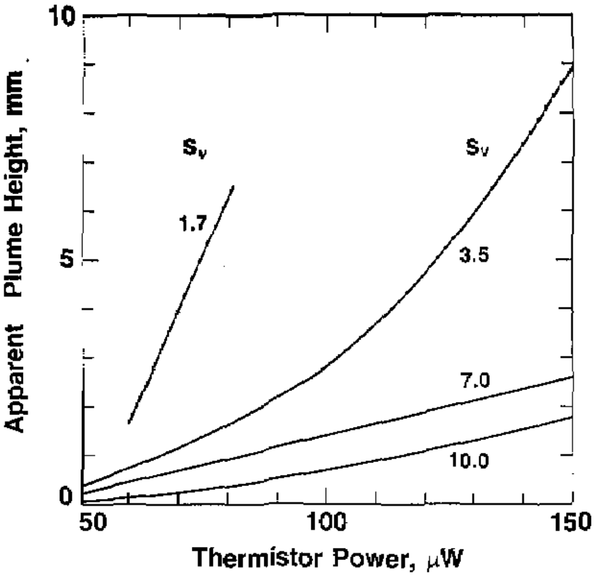

Figure 15. Summary of measurements of the "apparent" plume height as a function of thermistor power. The surface velocity S_v is in mm/min.

The above described test for convection around a thermistor as a function of power is much more sensitive than that previously described [3], where it was concluded that no convection of that type was observed.

8.2.1. Plume Theory The characteristics of a plume from a point heat source have been derived theoretically [14]. This is also discussed in [15], pp. 353–354 and [8], pp. 110–115. The basic theoretical equations apply to the condition where the rate of heat transfer from the source is sufficiently high to create a laminar convective plume. The present experiment indicates that this condition is satisfied when the power is at least 50 μW.

The theoretical calculations predict the following for a point source in water and $P=100$ μW. The velocity along the vertical axis is 7.2 mm/min, which remains constant with x, the distance above the source. The temperature rise at $x=1$ mm is 1.5 mK. Generally, the velocity and temperature rise vary as $P^{1/2}$ and Px^{-1}, respectively. The plume radius varies as $x^{1/2}$ $P^{-1/4}$. The rate of water flow through a horizontal plane at $x=1$ mm is 1.1 g/min; the mass flow rate varies as x, independent of P. This surprising result is due to the fact that mass flow is proportional to the product of velocity and the square of the radius, which is seen to be proportional to x [14].

9. Conclusion

The results of this investigation clearly reveal a potential source of inaccuracy in measurement of absorbed dose using large thermistor powers, in a water calorimeter in which uninhibited convection is allowed in the vicinity of the thermistor. Figures 5 and 6 can be used to estimate attenuation of this error by inhibiting the convective velocity with barriers and reducing the thermistor power, which should perhaps be as low as 2 μW. The output sensitivity of a Wheatstone bridge varies as the square root of the power, so the sensitivity does not decrease as rapidly as the power. Good signal-to-noise ratios can be attained at low power levels, particularly with the high dose rates available with therapy accelerators. To test the initial choice of thermistor power and convective barrier geometry, preliminary irradiation measurements should be made at several different power levels. No variation in measurements should be observed.

10. Summary

A calibrated thermistor was immersed in water. Electrical power dissipated in the thermistor caused it to rise to an equilibrium temperature above its initial temperature. The power was varied from 5 to 150 μW, and the equilibrium temperatures were disturbed by forced downward and upward simulated convection with water velocities from 1.3 to 17 mm/min. The velocities were related to the rate of temperature change, and also to the total temperature change from the original equilibrium value to a new equilibrium value. The rate of temperature change and temperature change were expressed as equivalent absorbed dose rate and absorbed dose, either positive or "negative."

11. Acknowledgment

The author is indebted to Ben Petree and Robert Loevinger for their critical reviews of the present and previous papers and for their many editorial improvements.

About the author: Steve R. Domen is a physicist in the Radiation Physics Division of NBS.

12. References

[1] ICRU Rep. No. 14, Appendix B. Bethesda, MD, ICRU Publications, 1969.

[2] Domen, S. R., Absorbed Dose Water Calorimeter, Med. Phys. 7, 157 (1980).

[3] Domen, S. R., An Absorbed Dose Water Calorimeter: Theory, Design, and Performance, J. Res. Natl. Bur. Stand. (U.S.) 87, 211 (1982).

[4] Schulz, R. J., and Weinhous, M. S., Convection Currents in a Water Calorimeter, Phys. Med. Biol. 30, 1093 (1985).

[5] Barnett, R. B., Water Calorimetry for Radiation Dosimetry, Ph.D. Thesis (1986), Univ. of Calgary, Calgary, Alberta Canada.

[6] Dring, R. P., and Gebhart, B., Hot-wire Anemometer Calibration for Measurements at Very Low Velocity, J. Heat Transfer 91, 241 (1969).

[7] Hollasch, K., and Gebhart, B., Calibration of Constant-Temperature Hot-Wire Anemometers at Low Velocities in Water with Variable Fluid Temperature, J. Heat Transfer 94, 17 (1972).

[8] Jaluria, Y., Natural Convection Heat Mass Transfer, Pergamon Press, Oxford (1980).

[9] Domen, S. R., Further Comments on Convection Currents in a Water Calorimeter. In press. Phys. Med. Biol.

[10] Domen, S. R., A Temperature-Drift Balancer for Calorimetry, Int. J. Radiat. Isot. 34, 927 (1983).

[11] Szymanski, P., Quelques Solutions Exactes des Équations de l'Hydrodynamique du Fluide Visqueux dans le Cas d'un Tube Cylindrique, J. Math. Pures Appl., Series 9 11, 67 (1932).

[12] Bird, R. B., Stewart, W. E., and Lightfoot, E. N., Transport Phenomena, John Wiley & Sons, New York (1960).

[13] Hall, N. A., Fluid Friction, Chapter 2 in Thermodynamics of Fluid Flow, Prentice-Hall, New York, NY (1951) pp. 18–36.

[14] Fujii, T., Theory of the Steady Laminar Natural Convection Above a Horizontal Line Heat Source and a Point Source, Int. J. Heat Mass Transfer 6, 597 (1963).

[15] Gebhart, B., Heat Transfer, McGraw-Hill, New York (1971).

Volume 93, Number 5, September-October 1988
Journal of Research of the National Bureau of Standards

Octacalcium Phosphate Solubility Product from 4 to 37 °C

Volume 93 Number 5 September-October 1988

M. S. Tung, N. Eidelman, B. Sieck, and W. E. Brown

American Dental Association
Health Foundation
National Bureau of Standards
Gaithersburg, MD 20899

Octacalcium phosphate (OCP) is proving to be an important intermediary in the formation of tooth and bone mineral and various pathological calcifications. Before this mineral can form, its solubility product must be exceeded. Thus, a knowledge of its precise values under various conditions is required for a basic understanding of calcification processes.

The methodology suitable for measuring the solubility of metastable phases was developed and used to determine the negative logarithms of the solubility products of OCP, pK_{sp}(OCP), at 4, 4.8, 6, 18, 23.5, and 37 °C. This methodology includes (1) the use of high solid-to-liquid ratio, 10 mg/mL, to minimize the effects of hydrolysis, (2) frequent sampling during equilibration to detect possible effects of hydrolysis, (3) equilibration from supersaturation and from undersaturation, and (4) equilibration in the absence and presence of a CO_2-containing atmosphere.

The resulting pK_{sp}(OCP) values are 48.3 ± 0.2, 48.3 ± 0.2, 48.2, 48.3, 48.4 ± 0.1 and 48.7 ± 0.2 at 4, 4.8, 6, 18, 23.5, and 37 °C. A 5.5% CO_2 atmosphere did not change the apparent pK_{sp}(OCP) value significantly. The value of pK_{sp}(OCP) obtained by approaching equilibrium from supersaturation was essentially the same as that from undersaturation.

The effects of (1) the use of different ionic models, (2) OCP hydrolysis, and (3) differences in equilibrium constants on the apparent pK_{sp}(OCP) values are described; the latter two contribute significantly to the differences in pK_{sp}(OCP).

Key words: equilibrium constants; hydrolysis; octacalcium phosphate; solubility; solubility product.

Accepted: April 14, 1988

Introduction

Octacalcium phosphate (OCP), $Ca_8H_2(PO_4)_6\cdot5H_2O$, is frequently encountered in calcium phosphate systems more basic than dicalcium phosphate dihydrate (DCPD), $CaHPO_4\cdot2H_2O$. It forms and hydrolyzes rapidly under physiological conditions [1]. There are many indications that it is the precursor in the formation of tooth and bone minerals and pathological calcium phosphates [2,3]. The structure of OCP has been determined [4] and its solubility reported [5–8]. The recently published values [5,6] for pK_{sp}(OCP) ($pK_{sp}(\text{OCP})=-\log K_{sp}(\text{OCP})$, where K_{sp}(OCP) is the solubility product of OCP) are in variance with older values [7,8] as shown in table 1. Thus, it is important to know the precise thermodynamic solubility of OCP in the form of the solubility product [pK_{sp}(OCP)] in order to assess the degree of saturation of biological fluids with respect to OCP. We report here values for pK_{sp}(OCP) at 4, 4.8, 6, 18, 23.5 and 37 °C. One of the main difficulties in obtaining the solubility of OCP is that OCP is not the most stable phase and will hydrolyze to other thermodynamically more

Table 1. Solubility products of OCP, as pK_{sp}(OCP), at various temperatures, this work and literature values. Values in parentheses were recalculated using our ionic equilibrium model

Temp. (°C)	This work	Nancollas et al. [5,6]	Madsen [7]	Moreno et al. [8]
4	48.3±0.2			
4.8	48.3±0.2			
6.0	48.2			
18	48.3			
23.5	48.4±0.1			
25		49.6±0.2[a] (49.0±0.2)[c]		46.97[b]
37	48.7±0.2	49.3±0.2[a] (49.1±0.3)[b]	48.46[a] (48.0)[b]	
45		49.8±0.3[a] (48.6±0.4)[b]		

[a] Calculated by Shyu et al. [5] and Heughebaert and Nancollas [6].

[b] Recalculated by using our ionic models and constants.

[c] Recalculated by using our ionic constants; when ionic activity coefficients were calculated from the extension of the Debye-Hückel limiting law, the $pK=48.97\pm0.25$; from the Davies equation $pK=49.03\pm0.23$.

stable calcium phosphates. Therefore, procedures suitable for measuring the solubility of metastable phases were developed and used. The methods minimize the effect of OCP hydrolysis and include (1) the use of high solid-to-liquid ratio, (2) frequent sampling during equilibration to detect possible effects of hydrolysis, (3) equilibration from supersaturation and from undersaturation, and (4) equilibration in the absence and presence of a CO_2-containing atmosphere, since carbonate slows down the hydrolysis. We have also studied the effect of OCP hydrolysis on the apparent solubility product and examined the possible causes for the differences in OCP solubility constants in the literature as compared to the values reported here.

Materials and Methods

Materials

OCP was prepared by two methods: (1) Hydrolysis of DCPD slurry in distilled water with addition of water dropwise over a period of about 3 months at room temperature [9]; this sample was designated as OCP-A and used for most of the study unless specified otherwise. The DCPD that was used for preparing the OCP was prepared by ammoniating an aqueous solution initially saturated with monocalcium phosphate monohydrate (MCPM), $Ca(H_2PO_4)_2 \cdot H_2O$, and DCPD, (i.e., at the singular point of MCPM and DCPD) according to the procedure described by Moreno et al. [10]. The OCP had a Ca/P ratio of 1.33±.02 and yielded a characteristic OCP x-ray diffraction pattern. (2) Growth of OCP by the constant composition method at pH=6[11]. This preparation was designated as OCP-B.

Analytical Methods

Two spectrophotometric methods were used to determine the concentration of calcium and phosphate: calcium as the Ca-Arzenazo III complex [12] and by atomic absorption [13], phosphate as vanado-molybdate [14] complex or the phosphomolybdate malachite green complex [12]. The estimated errors were ±1.5% of the amounts analyzed. The pH was measured with a combination glass-calomel reference electrode with estimated errors of ±0.008 pH units.

Equilibration Procedures

The saturated solutions of OCP were obtained by allowing OCP crystal dissolution or growth to proceed to equilibrium in solutions initially undersaturated or supersaturated with respect to OCP. Crystals of OCP were added to various concentrations of phosphoric acid (10 mg/mL), when equilibrium was approached from undersaturation, or to solutions containing potassium dihydrogen phosphate and calcium nitrate, when equilibrium was approached from supersaturation. The suspensions were stirred with a magnetic stirrer, and the experiments were carried out either in covered jacketed Pyrex cells through which thermostated water was circulated or in sealed plastic tubes which were mounted in a constant temperature bath at 4, 4.8, 6, 18, 23.5, or 37 °C. In some of the experiments the nitrogen or 5.5% CO_2/94.5% N_2 mixture presaturated with water was bubbled through the solutions. The equilibrations were allowed to proceed for different periods of time (15 min to 3.5 months). Samples were withdrawn periodically from the suspensions and either centrifuged at 15,000 rpm in an Eppendorf centrifuge (No. 5414) or filtered through a 0.22 μm filter (Millipore, Bedford, MA).[1]

The pH was measured just before taking the samples, after separation of the solids, and, in some cases, continuously at the initial stage. The calcium and phosphate concentrations of the supernatants or filtrates were determined as described above.

The ion activity products for OCP [*IP*(OCP)] were obtained from the calcium and phosphate concentrations, pH and ionic strengths using a computer program [15] which calculates the ion activity coefficients through the use of the extended Debye-Hückel equation [19] or Davies equation [20] and takes into account the ion pairs $CaOH^+$, $CaHPO_4$, $CaH_2PO_4^+$, $CaCO_3$ and $CaHCO_3^+$ [16], and dissociation of H_3PO_4 and H_2O, (Appendix) as follows:

$$IP(\mathrm{OCP})=(\mathrm{Ca}^{2+})^4(\mathrm{H}^+)(\mathrm{PO_4}^{3-})^3.$$

Here parentheses indicate ionic activities. The $K_{sp}(\mathrm{OCP})=IP(\mathrm{OCP})$ when the solution is in equilibrium with OCP. Unless specified otherwise, the extended Debye-Hückel equation was used.

Results

The compositions of solutions equilibrated with two different preparations of OCP and p*IP*(OCP) values as a function of time at 37 °C in a nitrogen atmosphere are presented in tables 2 and 3 (table 2 for solutions initially undersaturated, and table 3 for solutions initially supersaturated with respect to OCP). The results are similar for both preparations whether or not the initial solutions are under or super saturated with respect to OCP, except after 10 days. Equilibrium was obtained rapidly from both undersaturation and supersaturation (within 15 to 20 min) as indicated by constancy of the values of p*IP*(OCP) and pH of the solutions. In the equilibration of OCP-A from undersaturation, the p*IP*(OCP) was constant for about 10 days (depending on the initial phosphoric acid concentration) and then increased slowly after that. This increase is attributable to the hydrolysis of OCP to a more basic product which has lower solubility than that of OCP under the conditions studied. The pH of the solution increased rapidly in the first 15 minutes due to the dissolution of OCP, remained constant for 4.5 h, and then decreased slowly over the range of time studied, as indicated in table 2. The latter decrease can only be due to the hydrolysis of OCP to a non-stoichiometric "apatite." The hydrolysis produces phosphoric acid approximately as follows:

$$(10-x)\mathrm{Ca_8(PO_4)_6H_2\cdot 5H_2O}\rightarrow 8\mathrm{Ca}_{10-x}\mathrm{(PO_4)_6(OH)}_{2-2x}$$
$$+(12-6x)\mathrm{H_3PO_4}+(34+11x)\mathrm{H_2O}.$$

The Ca/(P − P_0) ratios in solutions should indicate the dissolution ratios. These ratios, although varying from the ratio for congruent dissolution (4/3), decreased with time, indicative of a hydrolysis process which increased the phosphate concentration in the solution. After equilibration of sample OCP-A for 3.5 months, only apatite lines could be detected in the x-ray powder diffraction patterns, and the p*IP*(OCP) was 50.1. When equilibrium was approached from supersaturation, the pH of the solution decreased rapidly from 5.7 to 5.47 in the first 20 minutes, as indicated in table 3, due to the precipitation of calcium and phosphate from solution and crystal growth of OCP. After that, the pH of the solution decreased slowly, and yet the p*IP*(OCP) remained constant. The slow decrease in the pH of the solution is again indicative of OCP hydrolysis to an apatite-like phase. Al-

---

[1] Certain commercial materials and equipment are identified in this paper to specify the experimental procedure. In no instance does such identification imply recommendation or endorsement by the National Bureau of Standards or the ADA Health Foundation or that the material or equipment identified is necessarily the best available for the purpose.

Table 2. Various times of equilibration of two batches of OCP with 0.457 mmol/L H_3PO_4 solutions from undersaturation at 37 °C and under N_2 atmosphere

		Composition of solution			
Time of equilib.	pH	[Ca] mmol/L	[P] mmol/L	$\frac{\mathrm{Ca}}{\mathrm{P}-\mathrm{P}_0}$	p*IP*
		OCP-A			
0	3.35	0.0	0.457		
15 min	6.35	0.614	0.994	1.14	48.86
31 min	6.32	0.616	0.993	1.15	48.98
62 min	6.30	0.630	1.032	1.10	48.98
2 h	6.36	0.644	1.052	1.09	48.68
4.5 h	6.35	0.670	1.092	1.06	48.68
23 h	6.16	0.806	1.367	0.89	48.88
10 d	5.43	2.91	5.37	0.59	48.78
2 months	4.75	7.29	13.91		49.69[a]
					av 48.83
		OCP-B			
0	3.33	0.0	0.457		
15 min	6.38	0.685	0.959	1.36	48.61
33 min	6.37	0.703	0.982	1.34	48.58
65 min	6.40	0.694	0.972	1.35	48.65
2 h	6.41	0.701	0.996	1.30	48.38
4.5 h	6.43	0.685	0.969	1.34	48.36
23 h	6.33	0.767	1.070	1.25	48.50
10 d	6.10	1.022	2.912	0.42	48.32
2 months	4.96	6.57	13.52	0.50	48.84[a]
					av 48.49

[a] Were not included in solubility calculation.

Table 3. p*IP* of OCP from supersaturation at 37 °C

		Composition of solution			
Time of equilib.	pH	[Ca] mmol/L	[P] mmol/L	$\frac{\mathrm{Ca}-\mathrm{Ca}_0}{\mathrm{P}-\mathrm{P}_0}$	p*IP*
0	5.70	4.43	3.33		47.59
20 min	5.47	4.41	3.38	−0.40	48.68
1 h	5.46	4.37	3.36	−2.00	48.75
2 h	5.45	4.35	3.39	−1.33	48.80
4 h	5.43	4.42	3.43	−0.10	48.86
22 h	5.41	4.60	3.73	0.43	48.79
					av 48.78
0	5.70	4.80	3.28		47.50
42 min	5.35	5.53	4.00	1.01	48.71
2 d	5.30	5.61	3.98	1.16	48.94
3 d	5.27	6.02	4.44	1.05	48.87
5 d	5.22	6.67	4.95	1.12	48.83
12 d	5.07	8.42	6.77	1.04	48.86
					av 48.84

though the hydrolysis of OCP-A seemed to occur early, as indicated by the decrease in pH and $\Delta Ca/\Delta P$ in 23 h, the effects of hydrolysis on the value of p*IP*(OCP) was observed only after 10 days in the equilibration from undersaturation (table 2). The hydrolysis of OCP-B was slow compared to that of OCP-A, as indicated by the change in pH of the solution (table 2); therefore, the variation of p*IP*(OCP) with time was not as great as in the case of OCP-A.

The results of pK_{sp}(OCP) under a 5.5% CO_2 atmosphere or under air (tables 4 and 5) fall in the same ranges as those under N_2 (tables 2 and 3). The hydrolysis rate, as indicated by decreases in pH and $\Delta Ca/\Delta P$ in tables 2, 4, and 5, depends on the CO_2 content in the atmosphere and decreases in the or-

Table 4. pK_{sp} of OCP under 5.5 volume % of CO_2/94.5 % N_2 atmosphere from undersaturation and at 37 °C

		Composition of solution			
Time of equilib.	pH	[Ca] mmol/L	[P] mmol/L	$\frac{Ca}{P-P_0}$	pK_{sp}
0	3.196	0	0.509		
1.5 h	5.996	1.27	1.53	1.24	48.80
2.0 h	5.937	1.31	1.57	1.23	49.00
28.0 h	5.928	1.30	1.69	1.10	48.97
2 d	5.949	1.30	1.73	1.06	48.84
5 d	5.914	1.50	1.99	1.01	48.61
7 d	5.930	1.49	2.04	0.97	48.52
9 d	5.812	1.63	2.15	0.99	48.87
12 d	5.764	1.80	2.65	0.84	48.70
16 d	5.675	1.95	2.99	0.79	48.86
					av 48.80
0	2.962	0	0.935		
1.5 h	5.808	1.42	2.07	1.25	49.14[a]
2.0 h	5.808	1.52	2.16	1.24	48.99
28.0 h	5.814	1.46	2.16	1.19	49.03
2 d	5.841	1.49	2.22	1.16	48.83
5 d	5.817	1.64	2.36	1.15	48.72
7 d	5.853	1.59	2.32	1.15	48.63
9 d	5.773	1.66	2.35	1.17	48.92
12 d	5.742	1.86	2.84	0.98	48.68
16 d	5.695	1.99	3.03	0.95	48.72
					av 48.82

[a] Was not included in solubility calculation.

Table 5. pK_{sp} of OCP under air atmosphere at 37 °C

		Composition of solution			
Time of equilib.	pH	[Ca] mmol/L	[P] mmol/L	$\frac{Ca}{P-P_0}$	pK_{sp}
0		0	0.463		
0.5 h	6.35	0.606	1.073	0.99	48.80
1 h	6.33	0.621	1.083	1.00	48.84
2 h	6.32	0.650	1.083	1.05	48.81
28 h	6.10	1.056	1.756	0.82	48.44
					av 48.72
0			0.463		
2 h	6.33	0.630	1.139	0.93	48.74
2 d	5.83	1.384	2.500	0.68	48.86
3 d	5.68	1.74	3.424	0.59	48.86
					av 48.82

der N_2>air>5.5% CO_2 due to the inhibitory effect of carbonate on hydrolysis. On the other hand there is no observable effect of carbonate on the pK_{sp}(OCP) presumably because carbonate cannot be incorporated into the OCP crystals.

The solubility products under different initial solution compositions at 4, 6, 4.8, 23.5, and 37 °C are shown in tables 6–11 together with the equilibrium times, composition of solutions and $\Delta Ca/\Delta P$. The results indicate that hydrolysis is slower when the initial solution has lower pH (i.e., higher phosphoric acid concentration), lower temperature, or the initial solution is supersaturated. There are indications of lack of attainment of saturation in the early stages of the equilibration in the presence of CO_2 (table 4) and in the solutions with low initial pH (table 11); the relatively high values of pIP(OCP) in the longest equilibrations indicate that the rate of hydrolysis approximated that of dissolution. The pIP(OCP) values obtained from the solutions which had not reached saturation in the early stages of the equilibration and from the solutions in which hydrolyzed OCP had increased the value of pIP(OCP) were not included in the results shown in table 1. The solutions were not considered to be in equilibrium with OCP when the pIP(OCP) values of the initial solutions or the final solutions were 0.2 units higher than the average pK_{sp}(OCP) value.

Table 6. Solubility of OCP at 4 °C

		Composition of solution			
Time of equilib. (days)	pH	[Ca] mmol/L	[P] mmol/L	$\frac{Ca}{P-P_0}$	pK_{sp}
0		0	0.236		
1	7.11	0.459	0.613	1.22	48.37
4	7.11	0.478	0.618	1.25	48.46
5	7.10	0.471	0.64	1.17	48.48
0		0	0.543		
5	6.77	0.781	1.22	1.12	48.18
0		0	0.825		
11	6.63	0.980	1.657	1.18	48.03
0		0	0.894		
1	6.52	1.05	1.401	2.07	48.57
2	6.54	1.05	1.667	1.36	48.29
4	6.55	0.989	1.664	1.28	48.34
				av	48.26±0.19

Table 7. Solubility of OCP at 4.8 °C

Initial conditions					Composition of solution			
pH	H_3PO_4 mmol/L	$Ca(OH)_2$ mmol/L	Time of equilib. (days)	pH	[Ca] mmol/L	[P] mmol/L	$\frac{Ca-Ca_0}{P-P_0}$	pK_{sp}
	0.248	0	11	6.93	0.577	0.791	1.06	48.47
	0.543	0	1	6.77	0.765	1.23	1.11	48.16
	0.849	0	17	6.38	1.17	2.05	0.97	48.52
	1.7	0	17	6.14	1.75	3.21	1.16	48.46
6.08	1.48	0.79	12	6.44	1.06	2.50	0.26	48.20
5.62	3.0	1.61	12	6.15	1.95	3.31	1.10	48.21
							av	48.34±0.16

Table 8. Solubility of OCP at 6.0 °C

Time of equilib.	pH	Composition of solution [Ca] mmol/L	 [P] mmol/L	pK_{sp} Ext. DH	 Davies
0	5.92	4	3		
5 min	5.95				
2 h	5.95	4.19	3.15	48.15	48.19
1 d	5.97	4.01	3.14	48.13	
4 d	5.95	3.93	3.11	48.26	
7 d	5.97	3.836	3.05	48.30	48.34
				av 48.21±0.08	

Table 9. Solubility of OCP at 18 °C

Time of equilib. (days)	pH	Composition of solution [Ca] mmol/L	 [P] mmol/L	pK_{sp}
9	6.76	0.586	0.897	48.24
22	6.47	0.840	1.486	48.27

Table 10. Solubility of OCP at 23.5 °C

Initial conditions pH	 H_3PO_4 mmol/L	 $Ca(OH)_2$ mmol/L	Time of equilib. (days)	pH	Composition of solution [Ca] mmol/L	 [P] mmol/L	$\frac{Ca-Ca_0}{P-P_0}$	pK_{sp}
	0.849		17	6.09	1.62	2.04	1.36	48.31
	1.7		17	5.94	1.74	3.20	1.16	48.37
	3.39		12	5.57	2.94	5.87	1.19	48.67
6.08	1.48	0.79	12	6.26	0.99	1.92	0.45	48.40
5.62	3.0	1.16	12	5.92	1.69	3.60	0.13	48.40
								av 48.43±0.14

Our values of pK_{sp}(OCP) (second column of table 1) increased only slightly in the temperature range 4 to 37 °C. Those reported by Shyu et al. [5] and Heughebaert and Nancollas [6] also varied only slightly in the range from 25 to 45 °C. Considering the experimental errors and the uncertainty of equilibrium constants used, these two studies indicate that the solubility product of OCP is not affected significantly by temperature. The two sets of data in the temperature range where they overlap are similar after correction for differences in ionic models and equilibrium constants, although our values for pK_{sp}(OCP) are smaller than theirs. An attempt is made in the discussion to compare the effect of OCP hydrolysis and the different ionic models and equilibrium constants on the pK_{sp}(OCP) values.

Discussion

The OCP is not the most stable phase under the conditions studied here or reported in the literature. Thermodynamically it will hydrolyze to other calcium phosphates; the kinetic rates depend on temperature, pH, solid-to-liquid ratio, and calcium-to-phosphate ratio in solution. Similar problems of instability have also been encountered in the solubility studies of carbonate- and fluoride-containing apatites [17] and tetracalcium phosphate. The

Table 11. pK_{sp} of OCP under N_2 atmosphere at 37 °C

		Composition of solution			
Time of equilib.	pH	[Ca] mmol/L	[P] mmol/L	$\frac{Ca}{P-P_0}$	pK_{sp}
0		0	0.242		
2 h	6.75	0.331	0.524	1.174	48.93
2 d	6.45	0.549	0.941	0.785	48.66
6 d	6.10	0.876	1.64	0.626	48.82
					av 48.80
0		0	0.463		
2 h	6.33	0.633	1.07	1.048	48.80
6 h	6.28	0.644	1.15	0.967	48.86
11 h	6.14	0.792	1.41	0.840	48.97
1 d	6.03	0.989	1.77	0.758	48.86
2 d	5.64	1.93	3.71	0.594	48.80
					av 48.86
0	2.96	0	0.935		
2 h	5.81	1.52	2.16	1.241	48.99
1 d	5.81	1.46	2.16	1.192	49.03
2 d	5.84	1.49	2.22	1.160	48.83
5 d	5.82	1.64	2.36	1.151	48.72
7 d	5.85	1.59	2.32	1.148	48.63
					av 48.84
0	6.08	0.79	1.48		
12 d	6.26	0.99	1.920	0.45	48.45
0	5.62	1.61	3.00		
12 d	5.70	1.95	4.28	0.27	48.44
0		0	3.39		
12 d	5.52	2.76	6.02	1.05	48.40
0		0	3.50		
2 h	5.37	2.86	5.67	1.32	49.02[a]
1 d	5.42	2.95	5.72	1.33	48.72
2 d	5.33	3.33	6.47	1.12	48.83
3 d	5.31	3.41	6.68	1.07	48.86
7 d	5.24	4.32	8.47	0.87	48.59
					av 48.75

[a] Was not included in solubility calculation.

longitudinal data given in tables 2–5 and 11 clearly reveal that hydrolysis was taking place in these studies: (1) The pH values of the solutions decreased monotonically with time. This is the result of OCP hydrolyzing into a more basic salt. In several instances, the pH changed more than a unit in its value without a large change in the p*IP*(OCP). The lack of change in the value of pK_{sp}(OCP) is apparently related to the hydrolysis process being slow compared to the rate of dissolution of OCP when relatively high solid-to-solution ratios are used. (2) The calcium and phosphate concentrations increased with time after equilibrium had been reached. This is in accord with the phase diagram for OCP. Despite the relatively large changes in pH and calcium and phosphate concentrations, the p*IP*(OCP) remained quite constant in most instances. This is in accord with a process in which the composition shifts along the OCP isotherm toward higher concentrations and lower pH values [18] so that the solution remains essentially saturated. One reason for this behavior is our use of a relatively high solid-to-solution ratio in the equilibrations; this favors a high dissolution rate compared to the hydrolysis rate.

Heughebaert and Nancollas [6] state: "The mean molar calcium/phosphate ratios of the solid phases after equilibrium in these experiments were 1.30±0.05 at 25 °C and 1.33±0.02 at 45 °C confirming the good stability of OCP in the aqueous media under these conditions of temperature and pH. In particular, hydrolysis of OCP into an HAp-like phase at 45 °C in the pH range 5.5–6.8 was never detected under the experimental conditions used." The changes in the solution composition at 25 °C [6], which is much more sensitive to the hydrolysis as compared to the changes in Ca/P ratios of the solid, indicate some hydrolysis of OCP. The ΔCa/ΔP values calculated from the Heughebaert and Nancollas 25 °C data (table II, ref. [6]) reveal that the ΔCa/ΔP ratios were larger than 1.33 (table 12) when equilibrium was approached from supersaturation (av ΔCa/ΔP = 1.53 when the unreliable value from expt. 52G is omitted) and all the ΔCa/ΔP ratios were smaller than 1.33 when equilibrium was approached from undersaturation. There is no overlapping in the two sets of data. The above results are in accord with hydrolysis processes in which a product more basic than OCP is being formed. For example, consider a process in which precipitation of OCP alone is occurring. The calcium lost from solution divided by phosphate that is lost in the same time interval, ΔCa/ΔP, would be 1.33. Now if, say, OHAp precipitated along with the OCP (or was formed by hydrolysis of OCP in situ), the quantity ΔCa/ΔP would be larger than 1.33. This is the situation with most of the 25 °C data from supersaturation (table 12). The reverse would be the case when approaching equilibrium from undersaturation. If only OCP were dissolving, ΔCa/ΔP would be 1.33. But if some OHAp were forming, Ca and P would be removed in a ratio greater than 1.33, leaving a net dissolved ΔCa/ΔP less than 1.33. Thus, the ΔCa/ΔP data at 25 °C (table 12) indicate that hydrolysis of OCP had occurred. The ΔCa/ΔP ratios calculated from the data at 37 °C by Shyu et al. [5] also indicate the occurrence of OCP hydrolysis. On the other hand, the solution compositions of the 45 °C equilibrations [6] do not indicate that hydrolysis of OCP had occurred, and the pK_{sp}(OCP), calculated from these data using our ionic model, is 48.6±0.4, the same as our value at 37 °C.

Table 12. Calculated ΔCa, ΔP, and ΔCa/ΔP values from the 25 °C data of Heughebaert and Nancollas [6]. The equilibrations 44G through 52G are equilibrations approached from supersaturation; those labeled 44D to 52D are from undersaturation

#	ΔCa	ΔP	ΔCa/ΔP
52G	0.014	0.005	2.8
50G	0.20	0.016	1.25
48G	0.37	0.22	1.68
47G	0.26	0.20	1.30
46G	0.27	0.15	1.80
44G	0.18	0.11	1.64
52D	0.092	0.096	0.96
50D	0.157	0.185	0.85
48D	0.151	0.187	0.81
47D	0.197	0.206	0.96
46D	0.215	0.227	0.95
44D	0.266	0.236	1.13

The pK_{sp}(OCP) values for four groups of investigators using different ionic models and equilibrium constants are compared in table 1. It is apparent that the pK_{sp}(OCP) values reported by Heughebaert and Nancollas [6] and by Shyu et al. [5] at 25 and 37 °C are about an order of magnitude higher than those reported here. Our 37 °C value is higher than the values attributed to Madsen [7]. Madsen's two values for pK_{sp}(OCP) are recalculations from his calculated solubility data that were based on an equilibrium model which did not include the ion pairs $CaH_2PO_4^+$, $CaHPO_4^0$, and $CaOH^-$. The Moreno et al. [8] value at 25 °C is based on a single composition (the singular point for brushite and OCP). Thus, even though it has been recalculated to take into account calcium and phosphate ion pairs, relatively little reliance can be placed on this value [8]. We discuss the causes for the discrepancies between our pK_{sp}(OCP) values and those of Shyu et al. [5] and of Heughebaert and Nancollas [6] in the following sections.

Thermodynamic Systems and Ionic Model

Heughebaert and Nancollas [6] and Shyu et al. [5] used a five component system, $Ca(OH)_2-H_3PO_4-KNO_3-H_2O-KOH$. The component KNO_3 was included in the Heughebaert and Nancollas [6] and Shyu et al. [5] systems so that extrapolations could be made to zero ionic strength in evaluating pK_{sp}(OCP). The component KOH was used to adjust the pH. We used mostly the ternary system, $Ca(OH)_2-H_3PO_4-H_2O$, except for the studies with initially supersaturated solutions. Our use of a ternary system was motivated by the desire to keep the system as simple as possible so as to avoid unanticipated ionic interactions. In the ternary system, the ionic strengths were generally so low that the ion activities could be calculated directly using the extended Debye-Hückel [10] or Davies equation [20]. However, both methods should yield satisfactory results provided they are based on a valid ionic model of the system. It is interesting that the pK_{sp}(OCP) values are not significantly different when either the extended Debye-Hückel equation or Davies equation is used as shown in tables 1 and 8.

Equilibration Conditions

Heughebaert and Nancollas [6] equilibrated their samples for 25 days at 25 °C and 12 days at 45 °C, apparently without sampling at shorter time periods; Shyu et al. [5] sampled at termination of each experiment after periods of 4, 10, 30 or 40 days. As indicated in the Methods section, we used higher solid-to-solution ratios (10 mg/mL) as compared to Shyu et al. [5] and Heughebaert and Nancollas (3 mg/mL), and sampled frequently at much shorter time periods. In doing so, a constant value of pK_{sp}(OCP) was obtained in a relatively short time. In the experiments with prolonged equilibration times, a subsequent increase in the value of the apparent pK_{sp}(OCP) was observed which we attribute to hydrolysis of the OCP to a more basic and less soluble form of calcium phosphate. Table 2 clearly shows increases in the apparent pK_{sp}(OCP) after the longer equilibration times.

Heughebaert and Nancollas [6] and Shyu et al. [5] approached equilibrium from both undersaturation and supersaturation. Most of our equilibrations were from undersaturation, but good agreement exists between our data from supersaturation and undersaturation.

The value of a pK_{sp}(OCP) calculated from a set of experimental data is particularly sensitive to small errors in the measurement of pH. Glass electrodes were used by both groups of investigators. Heughebaert and Nancollas [6] and Shyu et al. [5] used a silver/silver chloride reference electrode which incorporated an intermediate liquid junction containing potassium chloride solution at the same ionic strength as the solution being studied and, therfore, avoiding the diffusion of the potassium chloride into solution. We used a standard calomel reference electrode and minimized the diffusion of the potassium chloride by avoiding prolonged contact between the electrode and the solution.

Equilibrium Constants

The pK_{sp}(OCP) is calculated from the pH, [Ca], and [PO$_4$] data through the use of an ionic equilibrium model [15]. This model uses dissociation constants of H_3PO_4 and H_2O and the association constants of the ion pairs $CaHPO_4$, $CaH_2PO_4^+$, and $Ca(OH)^+$ and, in this study, $CaCO_3$ and $CaHCO_3$. A comparison of the constants used by Heughebaert and Nancollas [6] with those used by us (shown in table 13) reveals substantial differences in the formation constants for the ion pairs at some of the temperatures. In table 1 are given the 25, 37 and 45 °C values of pK_{sp}(OCP) reported by Shyu et al. and Heughebaert and Nancollas [5,6]. Below each of these values is given in parentheses the value we calculated using their data for pH, [Ca], [PO$_4$], and neutral ions with our model and equilibrium constants. The pK_{sp}(OCP) values calculated by Heughebaert and Nancollas [6] are significantly higher than our values calculated from the same experimental data; these differences are probably due to the different equilibrium constants used, since both the extended Debye-Hückel equation and the Davies equation gave the same results. Clearly, there is a need to reassess the values of the ion pair formation constants since they contribute significantly to the differences in the pK_{sp}(OCP) values as shown in table 1.

The pK_{sp}(OCP) values in our study are similar to those calculated from their data [5,6] with our model and equilibrium constants (table 1); our values are slightly lower than theirs at 23.5 to 37 °C probably due to the hydrolysis of OCP in their study.

Table 13. Equilibrium constants [5,6,15]

	25 °C		37 °C		45 °C	
	This study	Heughebaert et al. [6]	This study	Shyu et al. [5]	This study	Heughebaert et al. [6]
$H_3PO_4 \rightleftharpoons H^+ + H_2PO_4^-$	7.11×10^{-3}	7.11×10^{-3}	6.22×10^{-3}	6.22×10^{-3}	5.63×10^{-3}	5.63×10^{-3}
$H_2PO_4 \rightleftharpoons H^+ + HPO_4^{2-}$	6.31×10^{-8}	6.30×10^{-8}	6.58×10^{-8}	6.58×10^{-8}	6.60×10^{-8}	6.61×15^{-8}
$HPO_4^{2-} \rightleftharpoons H^+ + PO_4^{3-}$	4.52×10^{-13}	4.73×10^{-13}	6.84×10^{-13}	6.61×10^{-13}	9.02×10^{-13}	6.61×10^{-13}
$Ca^{2+} + H_2PO_4^- \rightleftharpoons CaH_2PO_4^+$	8.48	25.6	7.01	31.9	5.57	36.5
$Ca^{2+} + HPO_4^{2-} \rightleftharpoons CaHPO_4$	264	548	355	681	503	787
$Ca^{2+} + PO_4^{3-} \rightleftharpoons CaPO_4^-$	2.9×10^{6}	2.9×10^{6}	2.9×10^{6}	3.46×10^{6}	2.9×10^{6}	3.86×10^{6}
$Cu^{2+} + OH \rightleftharpoons CuOH^+$	20.0	13.8	20.0	21.3	20.0	28.4
$H^+ + OH^- \rightleftharpoons H_2O$	1.013×10^{-14}	1.004×10^{-14}	2.41×10^{-14}	2.42×10^{-14}	4.04×10^{-14}	4.09×10^{-14}

Acknowledgment

This investigation was supported, in part, by USPHS Research Grants DE05354 and HL30035 to the American Dental Association Health Foundation from the National Institutes of Health and is part of the dental and medical research program conducted by the National Bureau of Standards in cooperation with the American Dental Association Health Foundation. We thank T. M. Gregory and C. M. Carey for assistance in calculations.

About the authors: The authors are with the Paffenbarger Research Center, American Dental Association Health Foundation at NBS. M. S. Tung is a project leader, N. Eidelman is a research chemist, B. Sieck is a research assistant, and W. E. Brown is the Director Emeritus.

References

[1] Tomson, M. B., and Nancollas, G. H., Mineralization Kinetics: A Constant Composition Approach, Science **200**, 1059 (1978).

[2] Brown, W. E., Chow, L. C., Siew, C., and Gruninger, S., Acidic Calcium Phosphate Precursors in Formation of Enamel Mineral, in Tooth Enamel IV, R. W. Fearnhead, and S. Suga, Eds., Elsevier Science Publishers, Amsterdam, 1984.

[3] Tomazic, B. B., Etz, E. S., and Brown, W. E., Nature and Properties of Cardiovascular Deposits, Scanning Microsc. **1**, 95 (1987).

[4] Brown, W. E., Crystal Structure of Octacalcium Phosphate, Nature **196**, 1048 (1962).

[5] Shyu, L. J., Perrez, L., Zawacky, S. J., Heughebaert, J. C., and Nancollas, G. H., The Solubility of Octacalcium Phosphate at 37 °C in the System $Ca(OH)_2-H_3PO_4-KNO_3-H_2O$, J. Dent. Res. **62**, 398 (1983).

[6] Heughebaert, J. C., and Nancollas, G. H., Solubility of Octacalcium Phosphate at 25 and 45 °C in the System $Ca(OH)_2-H_3PO_4-KNO_3-H_2O$, J. Chem. Eng. Data **30**, 279 (1985).

[7] Madsen, H. E. L., Ionic Concentration in Calcium Phosphate Solutions, I. Solutions Saturated with Respect to Brushite or Tetracalcium Monohydrogen Phosphate at 37 °C, Acta Chem. Scand. **24**, 1671 (1970).

[8] Moreno, E. C., Brown, W. E., and Osborn, G., Stability of Dicalcium Phosphate Dihydrate in Aqueous Solutions and Solubility of Octacalcium Phosphate, Soil Sci. Soc. Amer. Proc. **21**, 99 (1960).

[9] Chickerur, N. S., Tung, M. S., and Brown, W. E., A Mechanism for Incorporation of Carbonate into Apatite, Calcif. Tissue Int. **32**, 55 (1980).

[10] Moreno, E. C., Brown, W. E., and Osborn, G., Solubility of Dicalcium Phosphate Dihydrate in Aqueous Systems, Soil Sci. Soc. Amer. Proc. **24**, 94 (1960).

[11] Heughebaert, J. C., and Nancollas, G. H., Kinetics of Crystallization of Octacalcium Phosphate, J. Phys. Chem. **88**, 2478 (1984).

[12] Vogel, G. L., Chow, L. C., and Brown, W. E., A Microanalytical Procedure for the Determination of Calcium Phosphate and Fluoride in Enamel Biopsy Samples, Caries Res. **17**, 23 (1983).

[13] Willis, J. B., The Determination of Metals in Blood Serum by Atomic Absorption Spectroscopy. I. Calcium, Spectrochim. Acta **16**, 259 (1960).

[14] Brabson, J. S., Dunn, R. L., Epps, E. Z., Jr., Hoffman, W. M., and Jacob, K. D., Report on Phosphorus in Fertilizers: Photometric Determination of Total Phosphorus, J. Assoc. Off. Anal. Chem. **41**, 517 (1958).

[15] McDowell, H., Gregory, T. M., and Brown, W. E., Solubility of $Ca_5(PO_4)_3OH$ in the System $Ca(OH)-H_3PO_4-H_2O$ at 5, 15, 25 and 37 °C, J. Res. Natl. Bur. Stand. (U.S.) **81A**, 273 (1977).

[16] Plummer, L. N., and Bussenberg, E., The Solubilities of Calcite, Aragonite and Vaterite in CO_2-H_2O Solutions Between 0 and 90 °C, and an Evaluation of the Aqueous Model for the System $CaCO_3-CoO_2-H_2O$, Geochim. Cosmochim. Acta **46**, 1011 (1982).

[17] LeGeros, R. Z., and Tung, M. S., Chemical Stability of Carbonate and Fluoride-Containing Apatites, Caries Res. **17**, 419 (1983).

[18] Brown, W. E., The Solubilities of Phosphates and Other Sparingly Soluble Compounds, in Environmental Phosphorus Handbook, J. Griffith, A. Beeton, and J. M. Spencer, Eds., John Wiley, New York, 1973, p. 203.

[19] Bates, R. G., Determination of pH: Theory and Practice, John Wiley & Sons, New York, 1973, p. 48.

[20] Davies, C. W., Ion Association, Butterworth & Co., London, 1960, p. 41.

[21] Kielland, J., Individual Activity Coefficients of Ions in Aqueous Solutions, J. Amer. Chem. Soc. **59**, 1675 (1937).

[22] Goldberg, R. N., An Equilibrium Model for the Calculation of Activity and Osmotic Coefficients in Aqueous Solutions, J. Res. Natl. Bur. Stand. (U.S.) **89**, 251 (1984).

[23] Sillen, L. G., Stability Constants of Metal-ion Complexes, The Chemical Society, Burlington, London, 1964.

Appendix

The ionic activity coefficients were calculated from the extension of the Debye-Hückel limiting law [19] or Davies equation [20]. The expanded Debye-Hückel equation is

$$\log f_i = -Az^2\sqrt{I}/(1+Ba_i\sqrt{I})$$

and the Davies equation is

$$\log f_i = -Az^2[\sqrt{I}/(1+\sqrt{I})-0.3I],$$

where f_i and I are the activity coefficients of species i and the ionic strength, respectively. A and B are functions of the temperature and the dielectric constant of the solvent (Appendix table 4, ref. [19]).

For the parameters a_i we used for Ca^{++}: 6×10^{-8} cm; for $H_2PO_4^-$: 4.5×10^{-8} cm; for $HPO_4^=$ and $PO_4^{\equiv}$: 4×10^{-8} cm; for H^+: 9×10^{-8} cm; and for OH^-: 3.5×10^{-8} cm [21]. The use of different values of a_i thermodynamically violates the Gibbs-Duhem equation [22]. The equilibrium constants for ion pairs, phosphoric acid and water are shown in table A1 [15,16,22]: $\log_{10}k=A_1/T^2+A_2/T+A_3+A_4T+A_5\log_{10}T$, where T=kelvins. The temperature dependence of the k_3 value for H_3PO_4 is given by: $-\log_{10}k=12.45-0.015(°C-18.0)$, where °C is the temperature.

Table A1. Parameters for equilibrium constants

Ion pair	A_1	A_2	A_3	A_4	A_5
H_3PO_4 k_1	0.	−799.31	4.5535	−0.01349	0.
H_3PO_4 k_2	0.	−1989.32	5.4374	−0.02001	0.
k_w	0.	−4470.99	6.0875	−0.01706	0.
H_2CO_3 k_1	−1684915.	21834.37	−356.3094	−0.06092	126.8339
H_2CO_3 k_2	−563714.	5151.79	−107.8871	−0.03253	38.9256
H_2CO_3 k_H (gas partition)	669365.	−6919.53	108.3865	0.01985	−40.4515
CaH_2PO_4	0.	−8232.51	57.1388	−0.09592	0.
$CaHPO_4$	0.	12213.79	−81.1027	0.14275	0.
$CaPO_4$	0.	0.	6.4624	0.	0.
CaOH	0.	0.	1.3010	0.	0.
$CaHCO_3$	0.	−34765.05	1209.1200	0.31294	478.782
$CaCO_3$	0.	35512.75	−1228.7320	−0.29944	−485.818

Volume 93, Number 5, September-October 1988
Journal of Research of the National Bureau of Standards

Conferences/Events

SURFACE METROLOGY A Report on the Fourth International Conference on the Metrology and Properties of Engineering Surfaces, National Bureau of Standards, Gaithersburg, MD, April 13-15, 1988

Surface metrology finds application to many branches of engineering ranging from optical surfaces to roadways. This triennial conference, held for the first time outside of England, traditionally attracts delegates with diverse interests from many countries. This year, in addition to the delegates from the United States, there were 20 delegates from England, five from France and others from Canada, West Germany, Austria, Japan, Sweden, and Ireland.

Delegates heard and debated 38 presentations on a wide variety of topics that, in retrospect, one could reorganize into the following general areas: measurement techniques, surface specimens, statistical characterization, production methods, and engineering function. A few of the interesting applications are described below.

One notable application to engineering function was Tabenkin and Parsons' (paper 38) use of the stylus technique to characterize the dispersion of carbon black agglomerates in rubber, a family of materials that might normally be thought of as too soft for reliable characterization by stylus. Inadequate dispersion leads to reduced product life and other detrimental effects in rubber products. Figure 1 shows the stylus in contact with such a rubber surface. The presence of the agglomerates is evidenced either by discrete peaks in the stylus profiles or by valleys left when the material is separated during the cutting process.

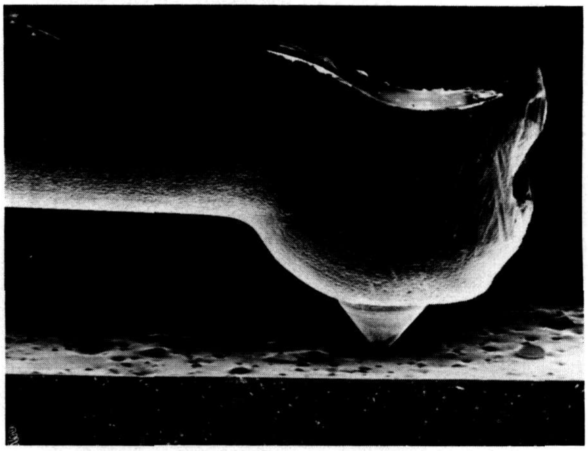

Figure 1. The presence of an agglomerate in a rubber sample is indicated by a peak or valley recorded on a chart as the stylus travels over the sample's surface. SEM micrograph from Tabenkin and Parsons (paper 38).

Rao et al. (paper 37) discussed their initial work to construct an expert system for selection of surface texture parameters. It was based on a table of results (table 1) gathered by Bielle and others (private communication) for the French automobile industry. The table relates a set of engineering functions such as static sealing with surface texture parameters that should be specified to optimize the function. However, the set of surface parameters shown in table 1, known as the R&W system, are defined using pattern recognition ideas rather than the conventional time series analysis. This approach to correlating surface function with surface finish is an interesting and controversial one.

The conference also recounted many significant advances in the area of measurement techniques.

The traditional technique for measuring surface texture is the stylus. However, nonstylus techniques are being increasingly studied and used. At this conference, research was presented on the measurement of surface texture by optical focusing, optical interferometry, optical scattering, infrared thermography, ultrasonics, two kinds of capacitance techniques, ellipsometry, and scanning tunneling microscopy.

Some of the most dramatic advances are in the field of interferometry (papers 2, 4, and 10) where height resolution at the Angstrom level can be achieved routinely nowadays.

At the large end of the scale, Pryor (paper 14) introduced a new optical imaging technique, known as D-sight, that can detect flaws and small form deviations with great sensitivity on large objects such as automobile and aircraft production components. Figure 2 shows an example of the sensitivity of the technique for inspection of a car body.

Table 1. Classification of engineering surface functions, important surface parameters, and notations on documents. Taken from J. Bielle (private communication) and presented by Rao et al. (paper 37)

SURFACE FUNCTIONS					PARAMETERS								
					ROUGHNESS			WAVINESS				TOTAL PROFILE	
DESIGNATIONS				SYMBOL	R	R_{MAX}	AR	W	W_{MAX}	W_t	AW	P_t	T_p (c)
TWO PARTS IN CONTACT	WITH RELATIVE DISPLACEMENT	SLIDING (LUB.)		FG	●			<.8R			○		●
		SLIDING (DRY)		FS	●		○		●		○		
		ROLLING		FR	●			<.3R	●		○		○
		RESISTANCE TO HAMMERING		RM	○		○	○			○		●
		FLUID FRICTION		FF	●		○				○		
		DYNAMIC SEALING	WITH SEAL	ED	●	○	○	<.6R	●		○		
			WITHOUT SEAL		○	●		<.6R					●
	WITHOUT DISPLACEMENT	STATIC SEALING	WITH GASKET	ES	○	●		< R		○	○		
			WITHOUT GASKET		○	●		< R		●			
		PRESS FIT		AC	○								●
		ADHERENCE (BONDING)		AD	●							○	
INDEPENDENT SURFACE	WITH STRESS	TOOLS (CUTTING SURFACE)		OC	○		○	●			●		
		FATIGUE STRENGTHS		EA	○	●	○						○
	WITHOUT STRESS	CORROSION RESISTANCE		RC	●	●							
		PAINT COATING		RE			○				○		
		ELECTROLYTIC COATING		DE	●	<2R	●						
		MEASURES		ME	●			< R					
		APPERANCE (ASPECT)		AS	●		○	○			○		

● : MOST IMPORTANT PARAMETERS TO BE SPECIFIED

○ : SECONDARY PARAMETERS TO BE SPECIFIED DEPENDING ON FUNCTIONS

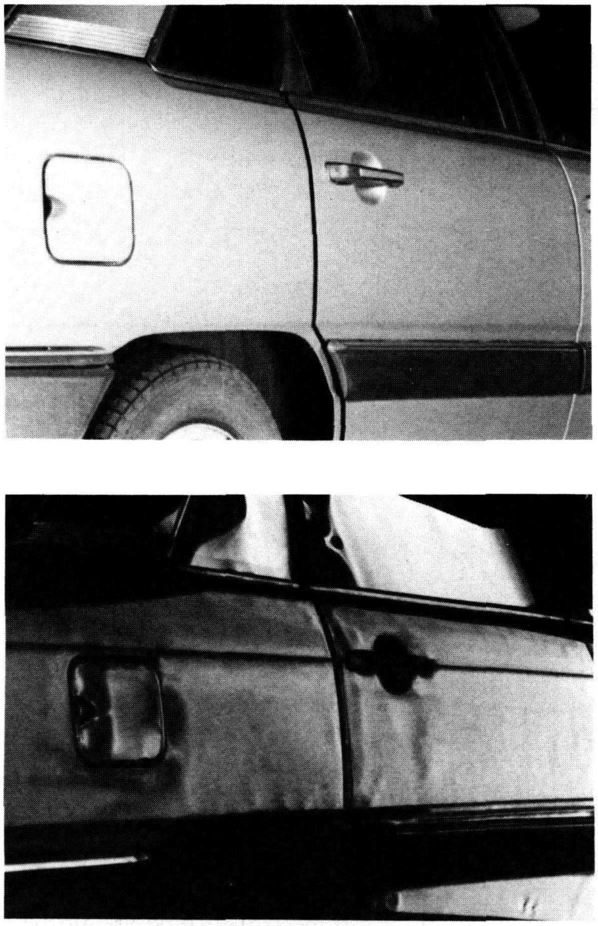

Figure 2. Comparison of a new car body viewed without D-sight (above) and with D-sight. The shadows in the images are caused by minute form deviations of the part. Taken from the work of Pryor et al. (paper 14).

Two kinds of capacitance methods were discussed. The area-averaging approach (fig. 3) was analyzed by Lieberman et al. (paper 11) with a realistic model that took into account both the electrical effects due to each tiny element of the surface and the mechanical flexibility of the sensor itself.

By contrast, Garbini et al. (paper 7) described their fringing field capacitive device for profiling (fig. 4). They showed good agreement of roughness average results measured by their approach with those obtained by the stylus technique.

In the area of statistical characterization, Whitehouse (paper 29) developed an interesting unification of friction measurements and stylus-type surface texture measurements and developed a single formulation of the dynamics of both types of systems. His paper highlighted the difficulties both of measuring surface texture in the presence of friction at the point of contact and of measuring friction of components having surface texture.

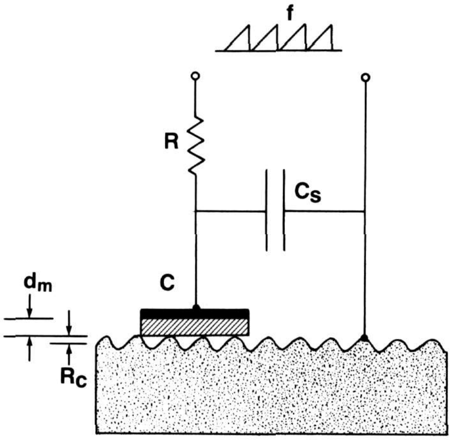

Figure 3. Schematic diagram of a capacitance instrument probing the topography of a rough surface. Capacitor C consists of the metallization (blackened) and the dielectric film (shaded) resting on the rough metal surface (speckled) beneath it. Taken from Lieberman et al. (paper 11).

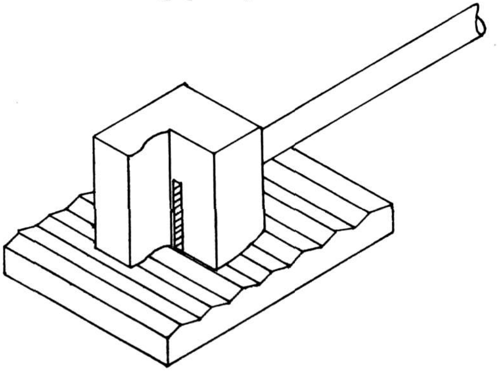

Figure 4. Cut-away view of the fringe field sensor. Taken from Garbini et al. (paper 7).

Lastly, two new types of surface texture specimens were presented. The specimens discussed by Song (paper 21) (fig. 5) had smooth random surfaces machined in steel with roughness average values ranging from 0.012-0.1 μm. They also had high uniformity from one place to the next in spite of the random surfacing process that had produced them. Berger (paper 20) discussed specimens fabricated by silicon technology. Each wafer surface contained a thermally grown SiO_2 layer with a single well-controlled thickness but with several feature spacings. The result was a surface consisting of "square waves" (fig. 6) suitable as a step height or pitch standard. Since it had four line spacings, one of them being as small as 6 μm, the sample could also be used to test the quality of stylus tip widths ranging from 1 to 12 μm.

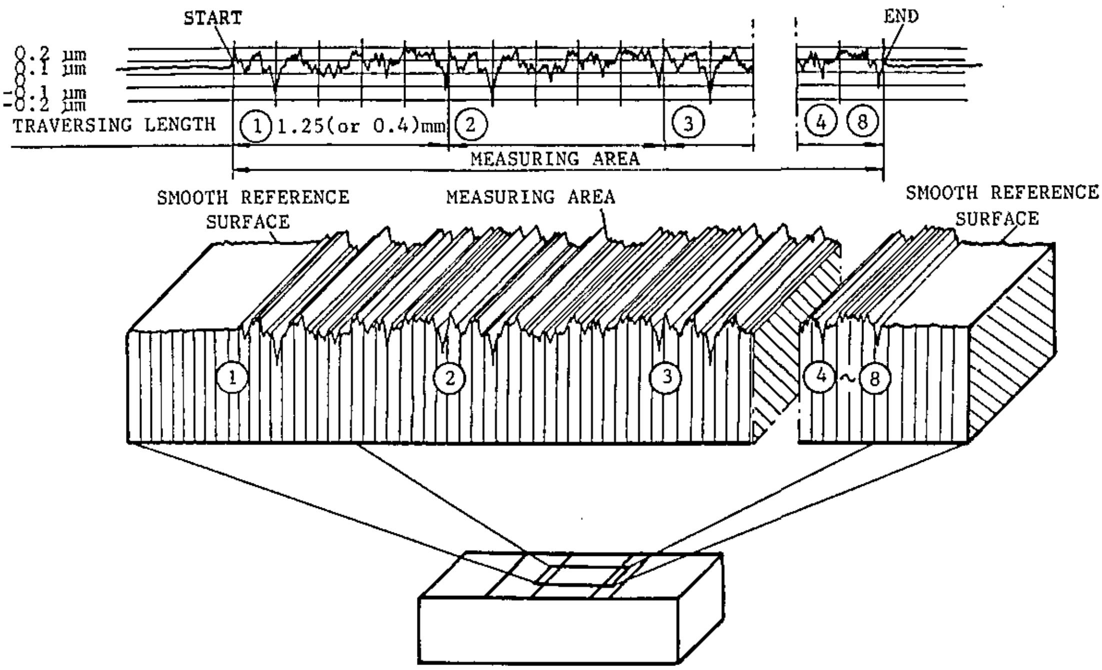

Figure 5. Detail of a roughness calibration specimen developed by Song (paper 21). It shows how the random roughness profile is repeated over the surface, thus achieving high uniformity.

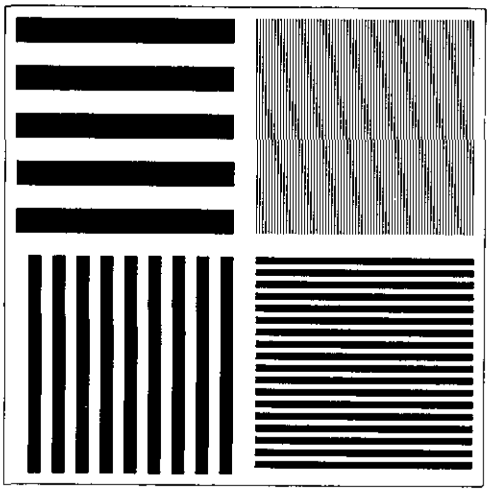

Figure 6. Layout of the "square wave" roughness specimen fabricated in silicon by Berger (paper 20). The specimen contains four patches having well-controlled pitches between the lines.

The conference co-chairmen were T. V. Vorburger from NBS and T. R. Thomas from Teesside Polytechnic, Middlesbrough, England. The success of the conference was due in great part to the energy of the organizing secretary, K. J. Stout, from the University of Birmingham, England.

List of Papers Presented at Conference

The proceedings, to be published as several successive issues in the journal, Surface Topography, and as *Proceedings of the Fourth International Conference on the Metrology and Properties of Engineering Surfaces* (Kogan Page, London, 1988), will include most of the presentations referenced below.

Measurement Techniques

1. Baker, L. R., Areal Measurement of Topography. (SIRA, UK)
2. Biegen, J., and Smythe, R., High Resolution Phase Measuring Laser Interferometric Microscopy for Engine Surface Metrology. (ZYGO, USA)
3. Blessing, G., and Eitzen, D.G., Surface Roughness Sensed by Ultrasound. (NBS, USA)
4. Bristow, T. C., Surface Roughness Measurements over Long Scan Lengths. (Photographic Sciences, USA)
5. Church, E. L., Dainty, J. C., Gale, D. M., and Takacs, P. Z., Measurement of Surface Topography by Interference Microscopy. (U.S. Army, USA/Imperial College, UK)
6. Evans, C. J., and Polvani, R. S., Some Observations of Subsurface Damage in Precision Machined Components. (NBS, USA)
7. Garbini, J. L., Jorgensen, J. E., Downs, R. A., and Kow, S. P., Fringe-Field Capacitative Profilometry. (University of Washington, USA)
8. Gee, A. E., Green, D., and Pain, D., An In-Process Tool Proximity Center for Ultra-fine Machining. (Cranfield, UK)

9. Jordan, D. L., Hollins, R. C., Jakeman, E., and Prewett, A., Visible and Infra-Red Scattering from Well Characterised Surfaces. (RSRE/University College, UK)
10. Lange, S. R., and Bhushan, B., Use of Two- and Three-Dimensional, Noncontact Surface Profiler for Tribology Applications. (WYKO/IBM, USA)
11. Lieberman, A. G., Vorburger, T. V., Giauque, C. H. W., Risko, D. G., and Rathbun, K. R., Comparison of Capacitance and Stylus Measurements of Surface Roughness. (NBS/Extrude Hone, USA)
12. Martin, J., Surface Roughness Measurement by Infrared Thermography. (NBS, USA)
13. Osanna, P. H., and Durakbasa, N. M., Comprehensive Analysis of Workpiece Geometry by Means of the Coordinate Measurement Technique. (Wien, AUSTRIA)
14. Pryor, T. R., Reynolds, R., and Pastorius, W., D-Sight: A Whole-Field Optical Technique for Determination of Surface Form Deviation. (Diffracto, CANADA)
15. Scott, P. J., Developments in Surface Texture Measurement. (Rank Taylor Hobson, UK)
16. Sullivan, P. J., Davis, E.J., and Stout, K. J., The Topographical Characteristics of Micro-Indentations and Their Relevance to Microhardness Testing. (Birmingham, UK)
17. Teague, E. C., Surface Metrology, Emphasize METROLOGY. (NBS, USA)
18. Wayte, R. C., Sayles, R., Tweedale, P. J., and Briscoe, B. J., The Design and Construction of an Inexpensive Laser Optical Profilometer. (Imperial College, UK)
19. Williams, M. W., Ludema, K. C., and Hildreth, D. M., Mueller Matrix Ellipsometry of Practical Surfaces. (University of Michigan, USA)

Surface Specimens

20. Berger, J., A New Surface Roughness Standard Fabricated Using Silicon Technology. (VLSI, USA)
21. Song, J. F., Random Profile Precision Roughness Calibration Specimens. (CIMM, CHINA)

Statistical Characterization

22. Kagami, J., Hatazawa, T., Yamada, K., and Kawaguchi, T., Three-Dimensional Observation and Measurement of Worn Surfaces. (Utsunomiya, JAPAN)
23. Radcliffe, S. J., and George, A. F., The Analysis and Presentation of Multi-trace Data and Some Applications in Industrial Research. (CEGB, UK)
24. Roques-Carmes, C., Wehbi, D., Quiniou, J. F., and Tricot, C., Modelizing Engineering Surfaces and Evaluating Their Non-Integer Dimension for Application in Material Science. (LMS-ENSMM, FRANCE)
25. Schneider, U., Steckroth, A., Rau, N., and Hubner, G., An Approach to the Evaluation of Surface Profiles by Separating Them into Functionally Different Parts. (Daimler-Benz, WEST GERMANY)
26. Sherrington, I., and Smith, E. H., Fourier Models of the Surface Topography of Engineering Components. (Preston, UK)
27. Thomas, T. R., and Thomas, A. P., Fractals and Engineering Surface Roughness. (Teesside, UK)
28. Watson, W., and Woods, A., The Three Dimensional Representation of Engineering Surfaces. (Leicester, UK)
29. Whitehouse, D. J., Friction and Surface Measurement. (Warwick, UK)

Production Methods

30. Gill, R., Surface Finish and Roundness Error in Centreless Grinding. (Middlesex Polytechnic, UK)
31. Strode, I., and Goodfellow, S., The Effect of Electrodischarge Machining on the Surface Integrity and Mechanical Properties of an Alloy Steel. (Polytechnic of Wales, UK)
32. Weck, M., and Modemann, K., Surface Quality as a Function of the Static and Dynamic Machine Tool Behaviour in Process. (Aachen, WEST GERMANY)

Engineering Function

33. Davis, E. J., Sullivan, P. J., and Stout, K. J., The Application of 3D Topography to Engine Bore Surfaces. (Birmingham, UK)
34. Dickson, G. R., McIlhagger, R., and Miller, P. P., The Effects of Mould Surface Finish and Processing Conditions on the Surface Characteristics of Polymeric Injection Mouldings. (Ulster University, UK)
35. Griffiths, B. J., Manufacturing Surface Design and Monitoring for Performance. (Brunel University, UK)
36. McCool, J. I., Predicting Flash Temperature at Microcontacts. (SKF, USA)
37. Rao, N. A. B., and Raja, J., A Knowledge Based System for Selection of Surface Texture Parameters—A Preliminary Investigation. (Michigan Technological University, USA)
38. Tabenkin, A. N., and Parsons, F. G., Surface Analysis for Measurement of Pigment Agglomeration in Rubber. (Federal Products, USA)

T. V. Vorburger
Precision Engineering Division
Center for Manufacturing Engineering
National Bureau of Standards
Gaithersburg, MD 20899

Calendar

October 3–6, 1988

MFPG 43rd MEETING: ADVANCED TECHNOLOGY IN FAILURE PREVENTION

Location: Kona Kai Hotel
San Diego, CA

The theme of the 43rd MFPG Meeting is improvement in mechanical systems and structure readiness, reliability, and maintainability through the application of advanced technology. Emphasis will be on developments in detection, diagnosis and prognosis (DD&P) instrumentation and techniques and on mechanisms of failure in both aircraft and industrial applications. The conference will highlight concurrent sessions in DD&P and mechanisms of failure and will also include the opportunity of visiting a San Diego area company for a technical presentation and demonstration. Sponsored by the National Bureau of Standards and Office of Naval Research in cooperation with American Helicopter Society.

Contact: T. Robert Shives, B106 Materials Building, National Bureau of Standards, Gaithersburg, MD 20899, 301/975-5711.

October 6–8, 1988

CONFERENCE ON MODERN INSTRUMENTATION AND ANALYSIS TECHNIQUES

Location: National Bureau of Standards
Gaithersburg, MD

The purpose of this conference is to provide a useful overview to dental materials researchers on application and use of modern measurement and analysis techniques. Some topics to be discussed include: Chromatography, HPLC, GPC, LC; Infrared Spectroscopy, IR, FTIR; Nuclear Magnetic Resonance Spectroscopy; X-Ray Scattering and Synchrotron Radiation; Neutron Scattering; Profilometry; Secondary Ion Mass Spectroscopy, and Scanning Transmission Electron Microscopy (STEM) and Transmission Electron Microscopy (TEM). Sponsored by the National Bureau of Standards and the Academy of Dental Materials.

Contact: Dr. John Tesk, A143 Polymer Building, National Bureau of Standards, Gaithersburg, MD, 20899, 301/975-6801.

October 13–14, 1988

IMPLEMENTATION OF PUBLIC LAW 100–235 (COMPUTER SECURITY): A FORUM FOR FEDERAL AGENCIES

Location: National Bureau of Standards
Gaithersburg, MD

This seminar will be the second in a series of workshops to assist Federal agencies in meeting their requirements for implementing the legislation. Participants will exchange ideas, methodologies, and materials developed by Federal agencies to protect information and information processing resources. The objectives, development, submission and review of system security plans will be addressed by representatives from Federal agencies, including NBS, OPM, OMB, NSA, NASA, and Treasury.

Contact: Anne Todd, B368 Technology Building, National Bureau of Standards, Gaithersburg, MD 20899, 301/975-3366.

April 3–7, 1989

6th INTERNATIONAL CONFERENCE ON HIGH TEMPERATURES: CHEMISTRY OF INORGANIC MATERIALS

Location: National Bureau of Standards
Gaithersburg, MD

This meeting brings together experts in the field of high temperature materials to discuss the latest scientific and technical developments. Both plenary and selected contributed papers are presented and published subsequent to the meeting. Academic, industrial and government researchers world wide with an interest in high temperature processing, performance and properties of inorganic materials will participate in the meeting. Organized under the joint sponsorship of the International Union of Pure and Applied Chemistry and the National Bureau of Standards.

Contact: John W. Hastie, B106 Materials Building, National Bureau of Standards, Gaithersburg, MD 20899, 301/975-5754.

April 17–21, 1989

NUCLEAR ANALYTICAL METHODS IN THE LIFE SCIENCES

Location: National Bureau of Standards
Gaithersburg, MD

Nuclear analytical methods, in particular nuclear activation techniques, constitute an important group of methods of chemical and physical-chemical analysis. This is the fourth symposium in a series on the subject of nuclear analytical methods in the life sciences. This meeting will review some of the more recent developments in the field and provide a viewpoint on the current status of nuclear techniques. Papers will be presented in oral and poster sessions on the following topics: (1) New and Emerging Methodology, (2) Activation Techniques, (3) Quality Assurance, (4) Comparison of Activation Analysis with Other Methods and (5) Applications of Nuclear Techniques in Biology, Medicine, Biotechnology, Agriculture, and Nutrition as well as in Public and Environmental Health.

This international conference is co-sponsored by the American Nuclear Society.

Contact: Rolf Zeisler, B108 Reactor Building, National Bureau of Standards, Gaithersburg, MD 20899, 301/975-6290.

April 26–28, 1989

FIFTY YEARS WITH NUCLEAR FISSION

Location: National Bureau of Standards
Gaithersburg, MD

Fifty Years with Nuclear Fission will be celebrated with a conference at the National Bureau of Standards and the National Academy of Sciences. Chaired by Dr. G. T. Seaborg, and Dr. E. Segrè, the first general session, held at the NAS, will feature invited talks devoted to an historical account of progress in the field given by leading contributors from the U.S. and abroad. The second and third days of the conference, to be held at NBS, will feature invited and contributed papers covering the following topics: Fission Theory, Experiments in Support of Theory, Instrumentation, Fission Applied Data, Astrophysical and Space Applications, Fission By-Products in Biology and Medicine, Industrial Fission By-Product Applications, Reactor Design and Development, Safeguards, Peaceful Uses of Fission Technology, and Applications in General Research.

Sponsored by the National Bureau of Standards and the American Nuclear Society, and co-sponsored by the American Physical Society Division of Nuclear Physics and by the American Chemical Society Division of Nuclear Chemistry and Technology.

For further information, contact Oren A. Wasson, B109 Radiation Physics Building, National Bureau of Standards, Gaithersburg, MD 20899, 301/975-5567, (FTS 879-5567).

May 4–5, 1989

9th CONFERENCE ON ROOFING TECHNOLOGY

Location: National Bureau of Standards
Gaithersburg, MD

The National Bureau of Standards and the National Roofing Contractors Association have joined in sponsoring conferences on roofing technology on a bi-annual basis since 1969. This conference is the 9th Conference on Roofing Technology. The theme of the conference is *Putting Roofing Technology to Work*. Topics to be discussed include thermal analysis for membrane characterization, field testing and the effect of surface contamination on adhesive-bonded seams, compatibility of insulations and membranes, vapor retarders, thermal bridging, planned maintenance, and new developments in coatings.

Sponsored by the National Roofing Contractors Association and the National Bureau of Standards.

Contact: Walt Rossiter, B348 Building Research Building, National Bureau of Standards, Gaithersburg, MD 20899, 301/975-6719.

June 7–9, 1989

SECOND INTERNATIONAL CONFERENCE ON HOT ISOSTATIC PRESSING (HIP)—THEORY AND APPLICATIONS

Location: National Bureau of Standards
Gaithersburg, MD

During the last 15 years Hot Isostatic Pressing (HIP) has proved to be a versatile technique for the manufacture of advanced products, such as fully dense powder parts, and to increase the performance of components, e.g., defect healing of castings. The technique is evolving steadily. Significant advances are occurring in the modeling of the densification process, in the development of more versatile HIP units, and in the application of HIP technology to new types of materials. The goal of this conference is to promote a wider awareness of advances which have occurred since the previous conference in Lulea, Sweden in the theories and application of HIP, and to stimulate discussions of these advances and of the future directions for HIP technology.

Sponsored by the National Bureau of Standards.

Contact: Dr. Robert Schaefer, A153 Materials Building, National Bureau of Standards, Gaithersburg, MD 20899, 301/975-6176.

July 23–27, 1989

SECOND INTERNATIONAL CONFERENCE ON CHEMICAL KINETICS

Location: National Bureau of Standards
Gaithersburg, MD

The purpose of this conference is to bring together leading individuals from universities, research laboratories, and industrial organizations to review the progress and problems of current interest in the measurement, evaluation, and application of fundamental chemical kinetic data to the analysis of complex chemical processes. The conference will focus on those areas of science and technology in which modeling is being successfully used to explain and predict complex phenomena. Subject areas of interest include: atmospheric chemistry, acid deposition, combustion chemistry, chemistry of energetic materials, plasma processing, analytical chemistry, modeling studies of complex systems, experimental and theoretical approaches to providing fundamental chemical data, and the assembly and evaluation of data bases for large scale simulation of complex systems. The conference will be concerned with both gas and condensed phase chemistry.

Sponsored by the National Bureau of Standards.

Contact: Dr. John Herron, A147 Chemistry Building, National Bureau of Standards, Gaithersburg, MD 20899, 301/975-2569.